Measurement of $\Lambda(1405)$ and $\Sigma^0(1385)$ photoproduction on the proton at Eγ = 1.5-3.0 GeV

Yohei Nakatsugawa

July 3, 2013

Abstract

The $\Lambda(1405)$ is assigned as a p-wave q^3 baryon in a quark model. However, it is also suggested that $\Lambda(1405)$ has a non-q^3 structure such as a meson-baryon molecular state. Some theoretical works using chiral Lagrangian and coupled unitary model predict the line shape of $\Lambda(1405)$ as $\pi\Sigma^0$ and $\overline{K}N$. Its 2-pole structure is also suggested. On the other hand, $\Sigma^0(1385)$ is firmly established as a q^3 state baryon. The difference of the internal structure of $\Lambda(1405)$ and $\Sigma^0(1385)$ may appear in the photoproduction cross sections and/or photon beam asymmetries of these two hyperons. Recently, differential cross sections for $\gamma p \to K^+\Lambda(1405)$ and $\gamma p \to K^+\Sigma^0(1385)$ reactions were measured by LEPS collaboration. However, the statistics were limited. A new experiment was carried out at SPring-8/LEPS with liquid hydrogen target and linearly polarized photon beam. In order to detect decay products of hadrons, a time projection chamber(TPC) surrounding the target was used together with the LEPS spectrometer.

The spectrum of hyperons are obtained from a missing mass of $\gamma p \to K^+\mathrm{X}$, but $\Lambda(1405)$ and $\Sigma^0(1385)$ can not be separeted due to their intrinsic widths. In order to obtain the yeilds of $\Lambda(1405)$ and $\Sigma^0(1385)$ separately, we selected following two reactions and required some cut conditions: (1) $\gamma p \to K^+\Sigma^0(1385) \to K^+\Lambda\pi^0 \to K^+ p\pi^-\ \pi^0$, (2) $\gamma p \to K^+\Lambda(1405) \to K^+\ \Sigma^\pm\pi^\mp \to K^+ n\pi^+\pi^-$. The spectrum of $\Sigma^0(1385)$ was extracted from reaction (1) using following cut conditions: (i) K^+ was detected in the forward spectrometer, (ii) a proton and a π^- were detected in the TPC, (iii) a $\Lambda(1116)$ was identified using the invariant mass of $p\pi^-$. Because $\Lambda(1405)$ is prohibited from decaying into $\Lambda\pi^0$ by isospin conservation, the yield of $\Sigma^0(1385)$ can be estimated by its decay branching ratios. The spectrum of $\Lambda(1405)$ was obtained from reaction (2) requiring following cut conditions: (iv) K^+ in the forward spectrometer, (v) a π^+ and a π^- were detected in the TPC, (vi) a neutron was identified using the missing mass of $\gamma p \to K^+\pi^+\pi^-\mathrm{X}$. It is pointed out that because of a strong interference of the isospin 0 and 1 terms of the $\Sigma\pi$ scattering amplitudes, the line shape of $\Lambda(1405)$ could be different in $\Sigma^-\pi^+$ and $\Sigma^+\pi^-$ decay modes. In order to separate both decay modes, a kinematic fit with two constraints, $\mathrm{MM}(K^+\pi^+\pi^-) = \mathrm{M}(n)$ and $\mathrm{MM}(K^+\pi^\pm) = \mathrm{M}(\Sigma^\mp)$, was applied. The isospin interference term is canceled by summing the spectra of the $\Sigma^-\pi^+$ and $\Sigma^+\pi^-$ modes. The summed spectrum was obtained after correcting for the decay branch of $\Sigma^+ \to p\pi^0$.

The differential cross sections of $\Lambda(1405)$ and $\Sigma^0(1385)$ were measured at three photon energy regions at $0.8 < \cos\Theta_{K^+CM} < 1.0$, where Θ_{K^+CM} is the polar angle of K^+ in the center of mass system. In the reference [24], the production ratio of $\Lambda(1405)$ to $\Sigma^0(1385)$ decreases with increasing photon energy and that may suggest the difference of the production mechanism of $\Lambda(1405)$ to $\Sigma^0(1385)$. The maximum photon energy of this data set is higher than that of thre previous experiment at LEPS. The differential cross sections of $\Lambda(1405)$ production were measured at three photon energy regions to be $0.236 \pm 0.017(\mathit{stat.}) \pm 0.011(\mathit{syst.})$ μb for $1.5 < E_\gamma < 2.0$ GeV, $0.153 \pm 0.015(\mathit{stat.}) \pm 0.016(\mathit{syst.})$ μb for $2.0 < E_\gamma < 2.4$ GeV and $0.642 \pm 0.035(\mathit{stat.}) \pm 0.017(\mathit{syst.})$ μb for $2.4 < E_\gamma < 3.0$ GeV.

The differential cross section at the highest photon energy region was found to be larger than at lower energy region.

This indicates t-channel contribution which can not be explained by tree-level K^- exchange, such as Regge trajectory of Vector Meson Dominance. In order to investigate exchanged

particle in t-channel, the photon beam asymmetry of $\Lambda(1405)$ photoproduction should be measured at forward angle of K^+.

Contents

1 Introduction **5**
- 1.1 Internal structure of the $\Lambda(1405)$ . . . 5
- 1.2 Photoproduction of hyperon resonances . . . 7
- 1.3 Previous experiment at LEPS using a Time Projection Chamber . . . 10
- 1.4 Physics motivation . . . 12

2 Experiment **15**
- 2.1 SPring-8 facility . . . 15
- 2.2 LEPS facility . . . 16
  - 2.2.1 Backward Compton scattering . . . 18
  - 2.2.2 Laser operating system . . . 21
- 2.3 Tagging system . . . 25
  - 2.3.1 Beam line setup . . . 25
- 2.4 LEPS spectrometer . . . 29
  - 2.4.1 Trigger counters . . . 29
  - 2.4.2 e^+e^- Blocker . . . 33
  - 2.4.3 Drift chambers . . . 34
  - 2.4.4 TOF wall . . . 36
  - 2.4.5 Dipole magnet . . . 37
  - 2.4.6 Solenoid magnet . . . 38
  - 2.4.7 RF signal . . . 39
- 2.5 The liquid hydrogen target . . . 40
- 2.6 Time Projection Chamber . . . 43
  - 2.6.1 High voltage membrane and field cages . . . 43
  - 2.6.2 Gas amplification part . . . 44
- 2.7 Electronics and Triggers . . . 49
- 2.8 Data summary . . . 51

3 Data analysis **56**
- 3.1 Event selection by the LEPS spectrometer . . . 56
  - 3.1.1 Particle identification by the LEPS spectrometer . . . 56
  - 3.1.2 Rejection of decay-in-flight of K^+ . . . 57
  - 3.1.3 Reaction vertex cut . . . 57
  - 3.1.4 The missing mass spectrum of $\gamma p \rightarrow K^+X$ reaction . . . 58
- 3.2 Track reconstrunction in the TPC . . . 58

3.2.1 Particle identification by the TPC 60
3.3 Analysis for $\Sigma^0(1385)$ photoproduction 64
3.3.1 Identification of $\Lambda(1116)$ by TPC 65
3.3.2 $MM(K^+)$ distribution for Λ tagged events 66
3.3.3 Background of $\gamma p \to K^+\Lambda(1405) \to K^+\Sigma^0\pi^0$ 66
3.3.4 Background of $\Lambda(1405)/\Sigma^0(1385) \to \Sigma^+\pi^-$ mode 69
3.3.5 Yield estimation of $\Sigma^0(1385)$ 70
3.4 Analysis for $\Lambda(1405)$ photoproduction 74
3.5 Neutron identification 74
3.6 Event selection by the kinematical fit 75
3.7 Selection of Σ^+ or Σ^- 76
3.8 $MM(K^+)$ spectra for charged decay modes 77
3.9 Yield of $\Lambda(1405)$ 78

4 Results **83**
4.1 Differential cross section 83
4.2 Photon energy dependence of the differential cross section 84
4.3 Comparison with two experiments at LEPS 84
4.4 Comparison with CLAS 84

5 Discussion **91**

6 Summary **93**

Chapter 1

Introduction

1.1 Internal structure of the $\Lambda(1405)$

In the quark model, the $\Lambda(1405)$ is an excited state of Λ hyperon and consists of three quarks (uds). It has the spin-parity of $J^P = \frac{1}{2}^-$. The isospin is 0 and the strangeness is -1. The mass and full width is 1405.1 MeV/c^2 and 50 MeV/c^2, respectively [1].

The $\Sigma^0(1385)$ has the same constituent quarks as the $\Lambda(1405)$ and its mass is close to that of the $\Lambda(1405)$. The $\Sigma^0(1385)$ has the spin-parity of $J^P = \frac{3}{2}^+$. The isospin is 1 and the strangeness is -1. The mass and full width is 1383.7 MeV/c^2 and 36 MeV/c^2, respectively [1]. While the $\Sigma^0(1385)$ is firmly established as a three quark(qqq) baryon resonance [2], the $\Lambda(1405)$ has some puzzling nature and its internal structure has been a controversial topic for a long time.

The $\Lambda(1520)$ has the spin-parity of $J^P = \frac{3}{2}^-$, and its mass is 1519.5 MeV/c^2 [1]. The $\Lambda(1405)$ and the $\Lambda(1520)$ are the spin-multiplet partners each other in the quark model. However, the mass of the $\Lambda(1405)$ experimentally observed is much smaller than that of the $\Lambda(1520)$ and this large difference between the mass of these two hyperons can not be explained by the spin-orbit interaction between quarks. In addition, the mass of $\Lambda(1405)$ is also much smaller than the theoretical calculation. For example, the calculation besed on a nonrelativistic quark model by Isgur and Karl predicted the mass of the $\Lambda(1405)$ to be 1.49GeV/c^2 [2]. Because the observed mass of the $\Lambda(1405)$ is close to the $\overline{K}N$ threshold, it has been suggested that the $\Lambda(1405)$ is the $\overline{K}N$ quasi-bound state [3, 4]. If the $\Lambda(1405)$ is such a meson-baryon molecule, the qqq baryon which is the spin-multiplet partner of the $\Lambda(1520)$ is missing. There has been a long discussion whether the $\Lambda(1405)$ is a qqq baryon or a meson-baryon molecule. The discussion is well summarized in the reference [5].

There have been various theoretical studies of the $\Lambda(1405)$. Some lattice QCD calculations predicted the mass of the $\Lambda(1405)$ based on the various quark configurations(qqq, $qqqq\overline{q}$), and the prediceted mass is much heavier than the observed mass of the $\Lambda(1405)$[6, 7, 8]. Nacher *et al.* dynamycally generated the lineshape of the $\Lambda(1405)$ as a $\pi\Sigma$ and $\overline{K}N$ bound state using a chiral Lagrangian and coupled unitary model [9]. This model also prediceted a second pole of the $\Lambda(1405)$ at 1.42GeV/c^2 which strongly couples to the $\overline{K}N$ channel [10]. According to their prediction, the second pole become visible for the reaction in which a virtual $\overline{K}$ interacts with a nucleon.

Until recently, there were only a few experimemtal studies on the $\Lambda(1405)$. It is difficult to distinguish the $\Lambda(1405)$ and the $\Sigma^0(1385)$ because the intrinsic widths of these two resonances are larger than the difference between their masses (Γ= 36 MeV/c^2 for $\Sigma^0(1385)$ and Γ= 50 MeV/c^2 for $\Lambda(1405)$). In the year 1973, Thomas *et al.* measured the lineshape of the $\Lambda(1405)$ in BNL via the $\pi^- p \to K_s^0 \Lambda(1405) \to K_s^0\ \pi^{\pm}\Sigma^{\mp}$ reaction [11]. Next, Hemingway measured the lineshape of the $\Lambda(1405)$ in CERN in the year 1984 via the $K^- p \to \pi^-\Sigma^+(1660)$ $\to \pi^-\pi^+\Lambda(1405) \to \pi^-\pi^+\pi^-\Sigma^+$ reaction [12]. Figure 1.1 shows the invariant mass spectrum of the $\Lambda(1405)$ measured by Hemingway. The solid histogram shows the measured spectrum. The solid, dotted and dashed line show the fitting results by the Breit-Wigner function, K-matrix fit and a extended cloudy bag model, respectively. The lineshape of the $\Lambda(1405)$ is asymmetric because it couples to the KN channel which opens from 1.43 GeV/c^2, and therefore, it is hard to be fitted by the Breit-Wigner function. K-matrix fit and cloudy bag model contain $\overline{K}N$ and $\Sigma\pi$ scattering amplitudes to reproduce the lineshape of the $\Lambda(1405)$. From these results, it has been suggested that the the $\Lambda(1405)$ strongly couples to the meson-baryon channel.

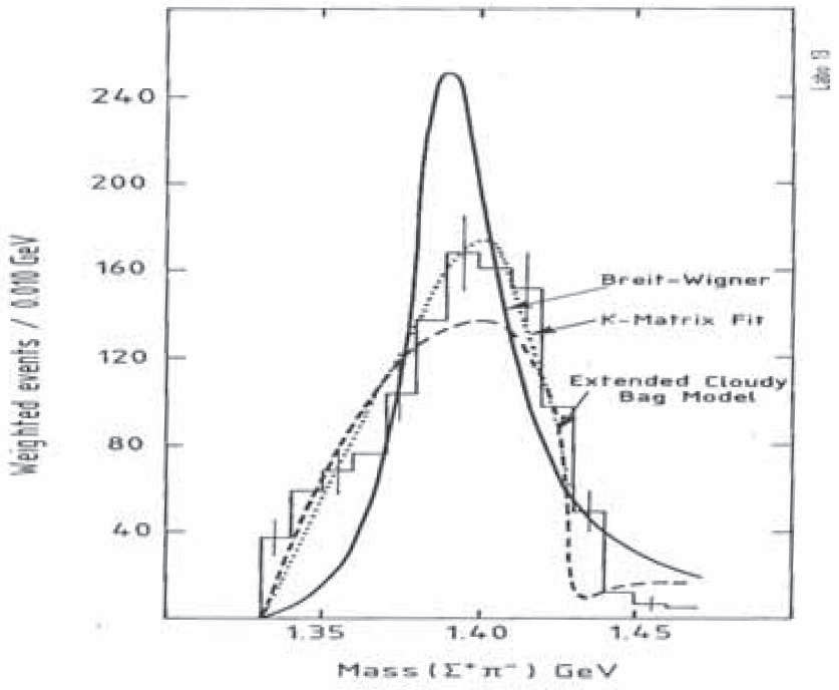

Figure 1.1: Invariant mass spectrum of the $\Lambda(1405)$ measured by Hemingway via the $K^- p \to$ $\pi^-\pi^+\Lambda(1405)$ reaction.

Recently, two more experimental studies have been reported. Prakhov *et al.* measured the cross section for $K^-\ p \to \pi^0\pi^0\Sigma^0$ reaction and observed that the contribution of $\pi^0\Lambda(1405)$ production dominates in this reaction [13]. In Figure 1.2, the solid and dashed histograms show the mass spectra of the $\Lambda(1405)$ obtained by Prakhov *et al.* and Thomas *et al.*, respectively. Magas *et al.* compared their model calculation with this data and claimed the evidence of the second pole of the $\Lambda(1405)$ [14]. The mass peak positions of the $\Lambda(1405)$ calculated by Magas *et al.* are indicated by the triangles. The mass peak positions of these two spectra are different.

The peak position measured by Prakhov *et al.* is around 1.41 GeV/c^2, while that measured by Thomas *et al.* is 1.39 GeV/c^2. According to the model calculation by Magas *et al.*, the second pole of the $\Lambda(1405)$ is enhanced in the $K^-\ p \to \pi^0\pi^0\Sigma^0$ reaction, and the peak position of the mass spectrum of $\Lambda(1405)$ is shifted to the higher mass side. Thus, they claimed the evidence of the second pole of the $\Lambda(1405)$.

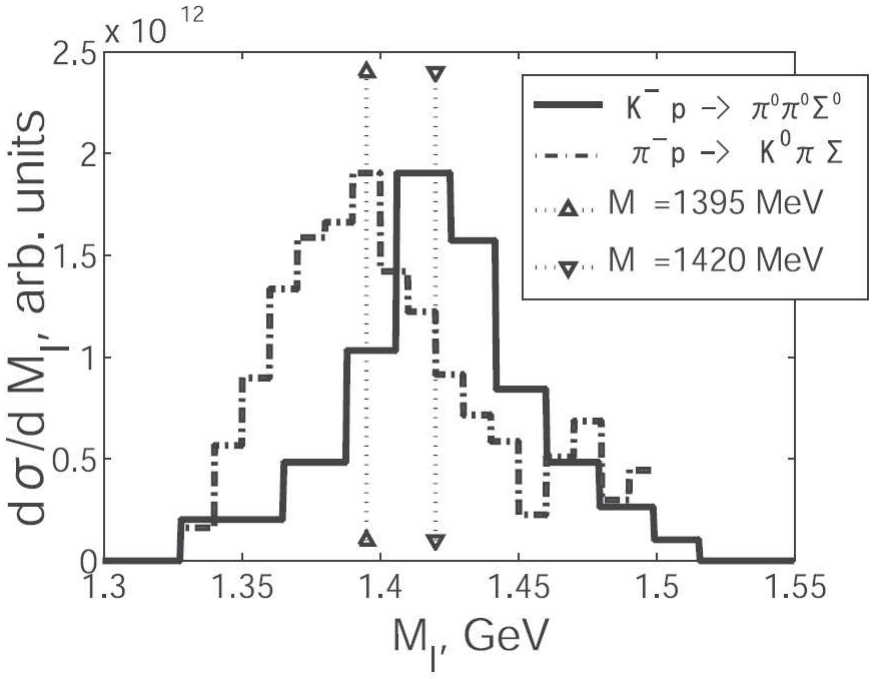

Figure 1.2: Mass spectra of the $\Lambda(1405)$measured by Prakhov *et al.*(solid) and Thomas *et al.*(dashed). The triangles indicate the mass peak position of the $\Lambda(1405)$ calculated by Magas *et al.*

Zychor *et al.* measured the lineshape and the production cross section of the $\Lambda(1405)$ via the $pp \to pK^+\Lambda(1405) \to pK^+\pi^0\Sigma^0$ reaction [15]. In Figure 1.3, the invariant mass spectrum of the $\Lambda(1405)$ measured by Zychor *et al.* is shown by closed circles together with the lineshape of the $\Lambda(1405)$ measured by Hemingway (solid histogram) and Thomas *et al.* (dashed histogram). The lineshape observed by Zychor *et al.* was consistent with those obtained by Hemingway and Thomas *et al.*

As seen above, the mass peak position and width of the $\Lambda(1405)$ are not determined clearly.

1.2 Photoproduction of hyperon resonances

The photoproduction of the Λ and Σ^0 hyperons off protons has been studied with high statistics data [16, 17, 18, 19], mainly motivated by missing resonances which could couple to the KY channels [20].

At SPring-8/LEPS, the photoproduction of the $\Lambda(1116)$ and $\Sigma^0(1192)$ on the proton has been measured by Sumihama *et al.* [19]. The K^+'s from a liquid hydrogen target were measured

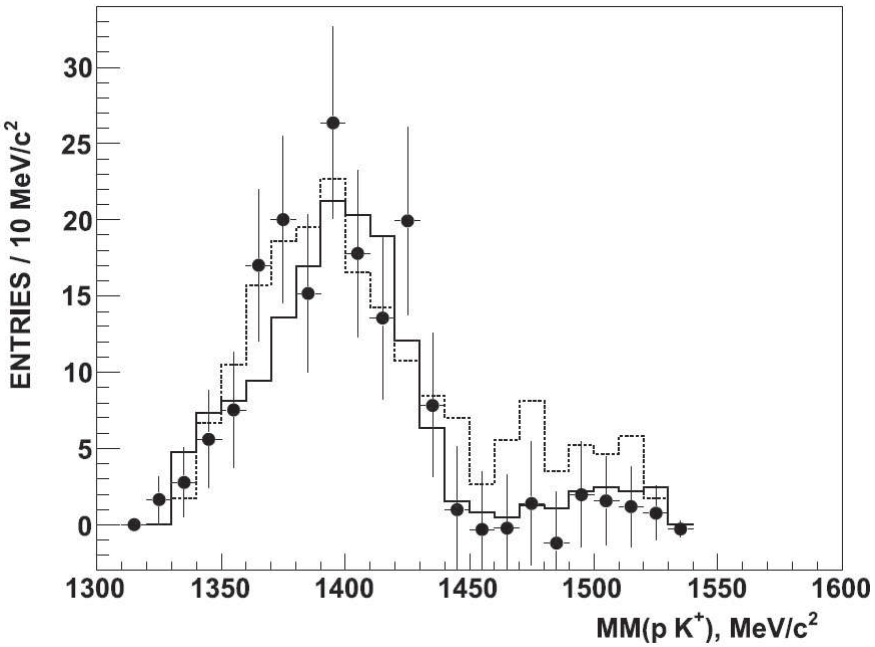

Figure 1.3: The invariant mass spectrum of the $\Lambda(1405)$. The spectrum measured by Zychor *et al.* is shown by closed circles. The spectra obtained by Hemingway and Thomas *et al.*are shown by the solid and dashed histograms, respectively. The solid and dashed histograms are normalized to the height of the spectrum measured by Zychor *et al.*

at the forward angles by the LEPS spectrometer. The statistics of this data set were sufficiently high to determind the differential cross sections accurately for the ground state Λ and Σ^0 hyperons. However, it is impossible to separate the $\Lambda(1405)$ and $\Sigma^0(1385)$ from missing mass of the $\gamma\ p \to K^+ Y^*$ reaction, $MM(K^+)$, because the spectra of the $\Lambda(1405)$ and the $\Sigma^0(1385)$ have a overlapped region. It is necessary to detect decay products from the hyperon resonances in addition to the K^+ to separate the $\Lambda(1405)$ and the $\Sigma^0(1385)$.

J.K.Ahn *et al.* measured the lineshape of the $\Lambda(1405)$ at SPring-8/LEPS via the $\gamma p \to K^+\Lambda(1405) \to K^+\pi^\pm\Sigma^\mp$ reaction [21]. In the measurement done by J.K.Ahn *et al.*, both a K^+ and a charged pion were detected by the LEPS spectrometer, and the Σ^+ or Σ^- was identified from a missing mass of the $\gamma\ p \to K^+\pi^\pm X$ reaction. The observed lineshape of the $\Lambda(1405)$ in the $\pi^+\Sigma^-$ and $\pi^-\Sigma^+$ modes are shown in Figure 1.4, respectively. The peak positions in two decay modes seem different, which can be understood as the result of the interference of the isospin 0 and 1 amplitudes of $\Sigma\pi$ scattering. The theoretical spectra obtained by Nacher *et al.* [9] are shown as dotted lines, which show a good agreement with the experimental data. In the measurement done by J.K.Ahn *et al.*, the contamination from the $\Sigma^0(1385)$ production was not studied because it was impossible to identify all of the decay products from the hyperon resonances due to the limited acceptance.

D.S.Ahn measured the differential cross sections and the photon beam asymmetries for $\gamma\ p \to K^+\Sigma^0(1385)/\Lambda(1405)$ reaction at SPring-8/LEPS [22]. In the measurement done by D.S.Ahn, the $\Sigma^0(1385)$ and the $\Lambda(1405)$ were not separated and it was found that the differ-

ential cross sections for $\Sigma^0(1385)/\Lambda(1405)$ had a forward peak at higher photon energy regions and the differential cross sections at the lower photon energy were almost flat and slightly decreased at the very forward angle. Then, it is suggested that the K^* exchange(natural parity exchange) for the $\Sigma^0(1385)$ is dominant at the higher photon energy regions and the K^- exchange(unnatural parity exchange) for the $\Lambda(1405)$ is dominant at the lower photon energy regions.

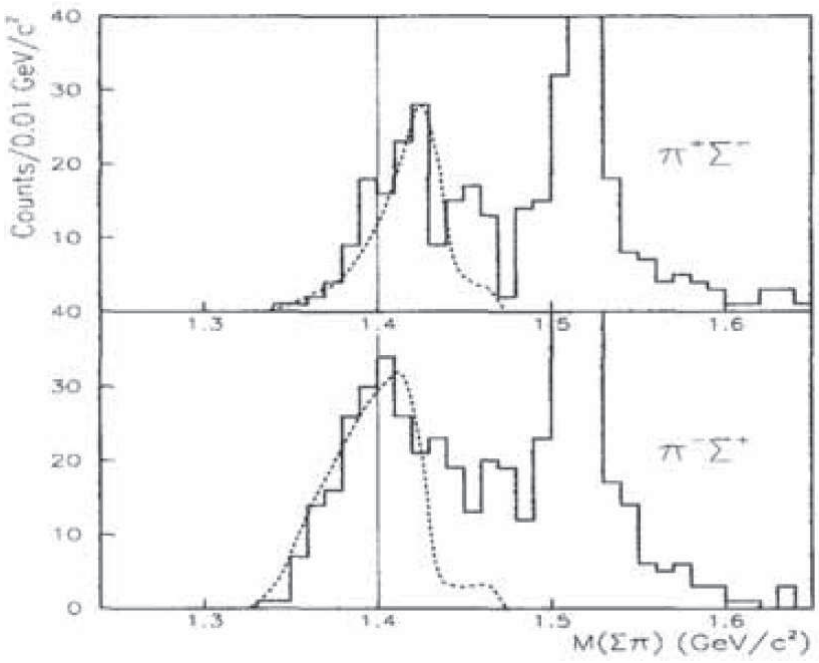

Figure 1.4: Invariant mass spectra of the $\Lambda(1405)$ measured by J.K.Ahn at LEPS [21]. The theoretical spectra by Nacher *et al.*[9] are shown as the dotted lines.

Theoretically, Nacher *et al.* [9] predicted the cross section of the $\Lambda(1405)$ photoproduction to be 5 μb/GeV at the peak of the invariant mass spectrum of the $\Lambda(1405)$ using a chiral unitary model. Lutz and Soyeur calculated the differential cross section for the sum of the $\Sigma(1385)$ and $\Lambda(1405)$ photoproduction using a chiral coupled-channel effective model [26]. In both theoretical calculations, the effect of the interference between the $\Lambda(1405)$ and $\Sigma^0(1385)$ production amplitudes was neglected.

The production mechanism for the $\gamma p \to K^+ Y^*$ reaction are shown in Figure 1.5, where Y^* stands for a hyperon resonance,$\Lambda(1405)$ or $\Sigma^0(1385)$. Figure 1.5(a) shows the t-channel $\overline{K}$ and $\overline{K}^*$ meson exchange diagram. The s-channel diagram shown in Figure 1.5(b) contains the contributions from nucleon and Δ resonances. The u-channel diagram shown in Figure 1.5(c) contains the contributions from hyperons ans their resonances. Figure 1.5(d) represents the contanct term required by the gause invariance.

In the SPring-8/LEPS, K^+'s produced by the $\gamma\ p \to K^+ Y^*$ reaction is detected in the forward angles, and hyperon resonaces are produced with a small momentum transfer. In general, t-channel $\overline{K}$ meson exchange diagram (Fig1.5(a)) is dominant in such a kinematical region. The $\overline{K}NY^*$ vertex in Fig1.5(a) depends on the spin and parity of the hyperon resonances,

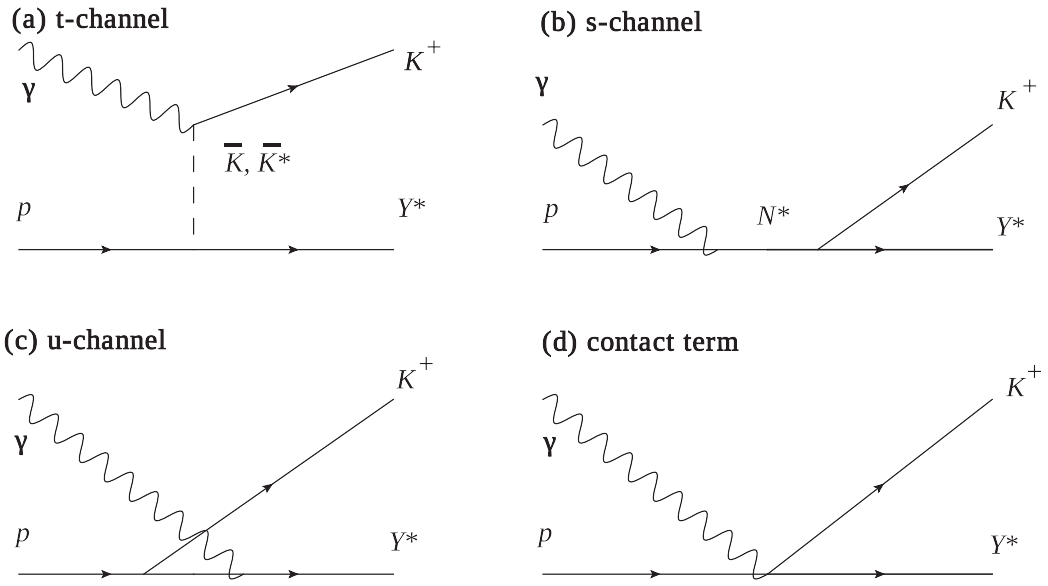

Figure 1.5: Feynman diagrams for the $\gamma p \rightarrow K^+ Y^*$ reaction.

$\frac{1}{2}^-$ for the $\Lambda(1405)$ and $\frac{3}{2}^+$ for the $\Sigma^0(1385)$, and shows the different energy dependence for each hyperon resonance. The $\overline{K}\Lambda^*$ vertex consists of the $\overline{K}\Lambda^*$ coupling constant, and does not depend on the three momentum transfer, q. On the other hand, the $\overline{K}\Lambda^*$ vertex contains $\partial_\mu \overline{K} N \Sigma^{*\mu} N$ term, and the T matrix is proportional to q. By taking account of an additional q-dependence due to the phase volume, the production cross section of $\Lambda(1405)$ is proportinal to q, and that of $\Sigma^0(1385)$ is proportional to q^3. Because the momentum transfer increases as the photon energy, the contribution of $\Sigma^0(1385)$ is expected to increase in higher photon energy region.

1.3 Previous experiment at LEPS using a Time Projection Chamber

A hyperon photoproduction experiment was carried out at SPring-8/LEPS facility using a Time Projection Chamber (TPC) together with the LEPS forward spectrometer [24]. In this experiment, $\gamma p \rightarrow K^+\Lambda(1405)$ reaction and $\gamma p \rightarrow K^+\Sigma^0(1385)$ reaction were studied in two photon energy regions of $1.5 < E_\gamma < 2.0$ GeV and $2.0 < E_\gamma < 2.4$ GeV, at $0.8 < \cos\Theta_{K^+CM} < 1.0$, where E_γ and Θ_{K^+CM} stand for the photon energy and the angle of K^+momentum with respect to the beam axis in the center of mass system, respectively. Closed circles in Figure 1.6 show the experimantal data measured by the LEPS TPC experiment. Figure 1.6(a) and (b) show the missing mass spectra of $\gamma\ p \rightarrow K^+X$ at photon energy region of $1.5 < E_\gamma < 2.0$ GeV and $2.0 < E_\gamma < 2.4$ GeV, respectively. The data were fitted with background spectra obtained by Monte Carlo simulation and the line shape predicted by Nacher *et al.* The solid

lines show the contribution of the $\Lambda(1405)$.

The production ratio of $\Lambda(1405)$ to $\Sigma^0(1385)$ was measured to be 0.54 ± 0.17 and 0.074 ± 0.076 for $1.5 < E_\gamma < 2.0$ GeV and $2.0 < E_\gamma < 2.4$ GeV, respectively.

The differential cross sections for $\gamma p \to K^+\Lambda(1405)$ and $\gamma p \to K^+\Sigma^0(1385)$ reactions were also obtained combining this production ratio and the results of another experiment at LEPS. The differential cross sections for the $\Sigma^0(1385)$ production were found to be $0.80 \pm 0.092(stat.)\ ^{+0.062}_{-0.27}(syst.)$ μb at $1.5 < E_\gamma < 2.0$ GeV and $0.87 \pm 0.064(stat.)\ ^{+0.13}_{-0.067}(syst.)$ μb at $2.0 < E_\gamma < 2.4$ GeV. For $\Lambda(1405)$production, the differential cross section was found to be $0.43 \pm 0.088(stat.)\ ^{+0.034}_{-0.14}(syst.)$ μb at $1.5 < E_\gamma < 2.0$ GeV and an upper limit of 95% confidence level was determined to be 0.19 μb at $2.0 < E_\gamma < 2.4$ GeV.

The measured production ratio of $\Lambda(1405)$ to $\Sigma^0(1385)$ decreased in the higher photon energy region. This result suggests that $\Lambda(1405)$ and $\Sigma^0(1385)$ have different production mechanisms.

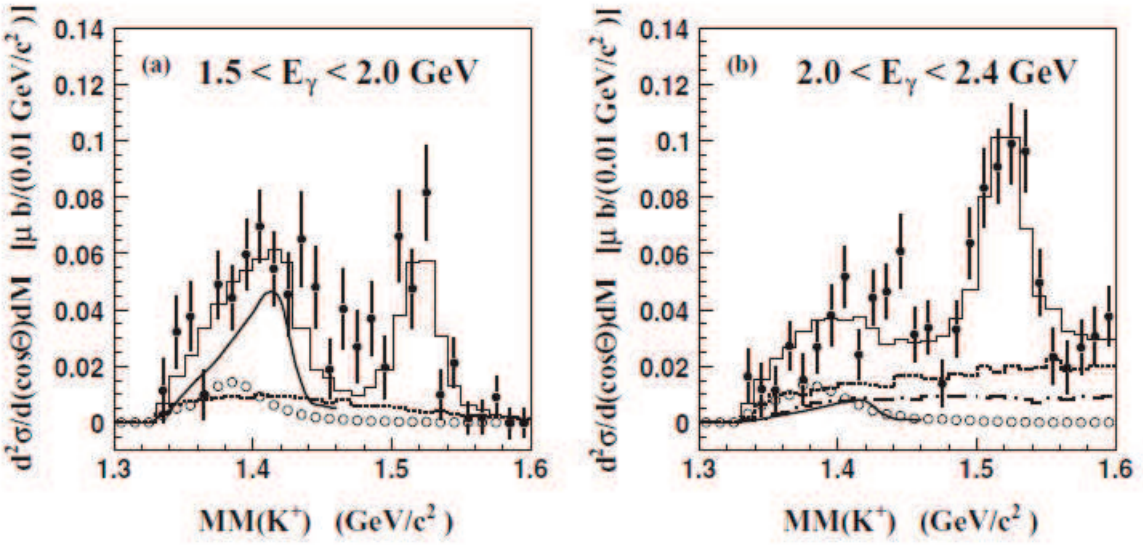

Figure 1.6: The missing mass spectra of the reaction $\gamma p \to K^+ X$ ($MM(K^+)$) obtained by Niiyama *et al.* . The spectra are shown in two photon energy ranges: (a) $1.5 < E_\gamma < 2.0$ GeV and (b) $2.0 < E_\gamma < 2.4$ GeV .

Recently, Moriya *et al.* measured lineshape, total/differential cross sections of $\Sigma^0(1385)$, $\Lambda(1405)$ and $\Lambda(1520)$ photoproduction at CLAS[23]. The measured differential cross sections of the $\Sigma^0(1385)$, $\Lambda(1405)$ and $\Lambda(1520)$ photoproduction are shown in Figure 1.7. The differential cross sections($\frac{d\sigma}{dcos\Theta_{K^+CM}}$) for these hyperons increase according to the forward angles in all the photon energy regions, and it is noticeable in the higher photon energy bins. These results are compared to the differential cross sections of the $\Lambda(1405)$ photoproduction obtained by LEPS TPC experiment (blue points) at the Wbin 1-4 regions. They are almost similar to those obtained by LEPS TPC experiment in the lower photon energy regions(Wbin 1-2), but they are significantly different at the higher photon energy regions(Wbin 3-4). It was found that they are distinctly larger than the results obtained by LEPS TPC experiment at the higher photon

energy regions. On the other hand, it was found that the results of CLAS measurement for $\Sigma^0(1385)$ were similar to those obtained by LEPS TPC experiment. A theoretical calculation by Oh *et al.* [25] using an effective Lagrangian was then compared with the total cross section of $\Sigma^0(1385)$ photoproduction measured by the CLAS experiment, and the contributions from nucleon resonances were discussed.

1.4 Physics motivation

It is quite important to investigate the photon energy dependence of $\Lambda(1405)$ photoproduction. The mechanisms of hyperon photoproduction reflect on the photon energy dependence.

Nam *et al.*[27] suggested s-channel dominance for $\Lambda(1405)$ photoproduction to explain the decrease of $\Lambda(1405)$ photoproduction at higher photon energy region shown by the LEPS TPC experiment. Figure 1.8 shows the cross section for $\Lambda(1405)$ photoproduction calculated by [27].

However, the measurement was performed at only two photon energy regions in the LEPS TPC experiment. It is necessary to measure the cross section at higher energy region to conclude the behavior of the photon energy dependence of $\Lambda(1405)$ photoproduction.

In addition, the statistical uncertainty of the LEPS TPC experiment is large because the yield of $\Lambda(1405)$ photoprodution on a free proton was extracted from the data of CH_2 target, subtracting the contribution from Carbon.

In order to confirm the results of the previous LEPS TPC experiment precisely with high statistics and perform a new measurement at higher photon energy region, a new experiment was carried out at SPring-8/LEPS with a liquid hydrogen target and a photon beam with maximum photon energy of 3 GeV. In order to detect decay products of hadrons nearby the liquid hydrongen target, a new Time Projection Chamber was developed.

In this thesis, the differential cross sections for $\gamma p \rightarrow K^+\Lambda(1405)$ and $\gamma p \rightarrow K^+\Sigma^0(1385)$ reaction were measured in three photon energy range, $1.5 < E_\gamma < 2.0$ GeV, $2.0 < E_\gamma < 2.4$ GeV and $2.4 < E_\gamma < 3.0$ GeV. We obtained the cross sections at $2.4 < E_\gamma < 3.0$ GeV as new results.

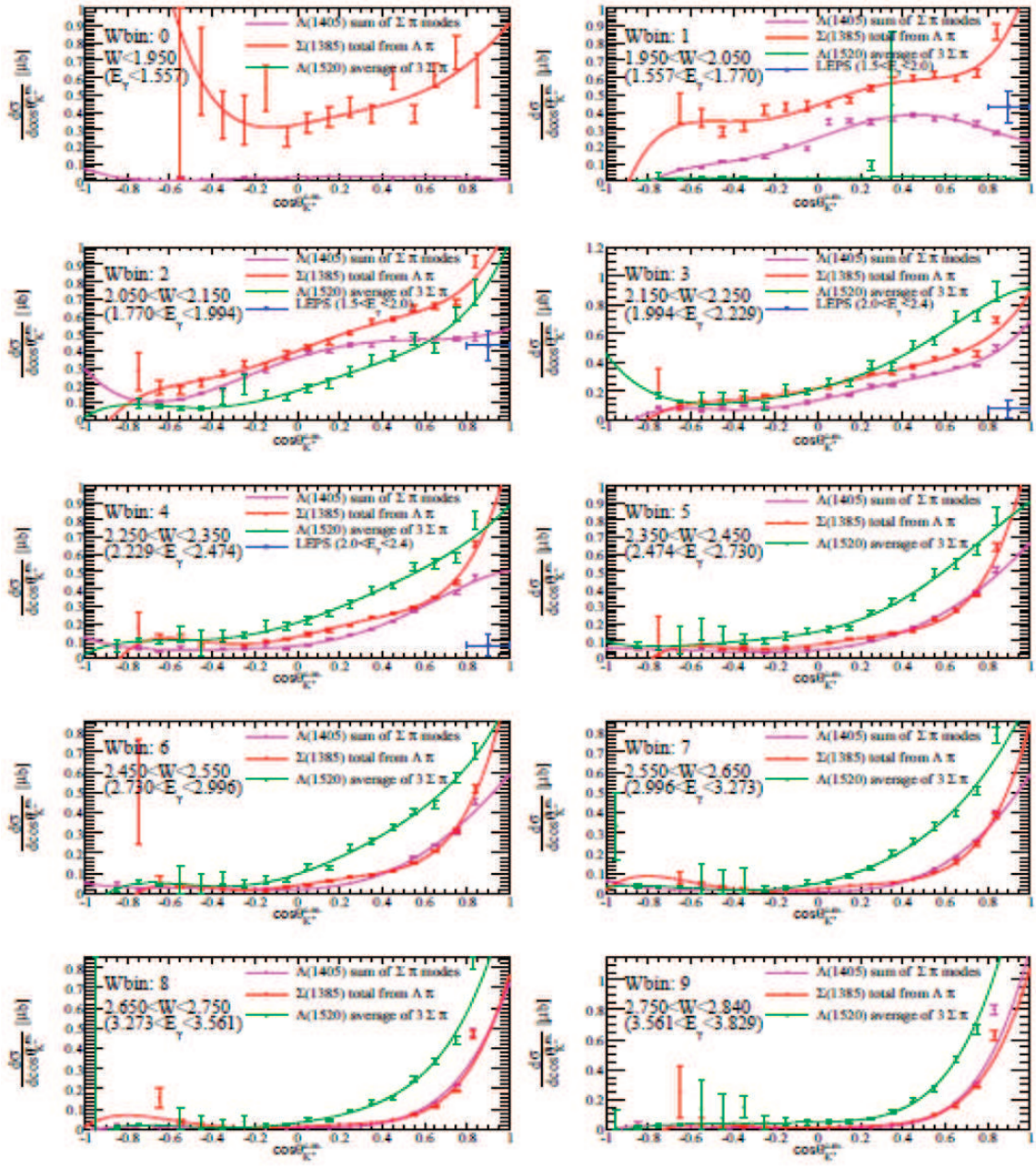

Figure 1.7: Differential cross sections for $\Sigma^0(1385)$(red), $\Lambda(1405)$(magenta) and $\Lambda(1520)$(green) photoproduction measured at CLAS.

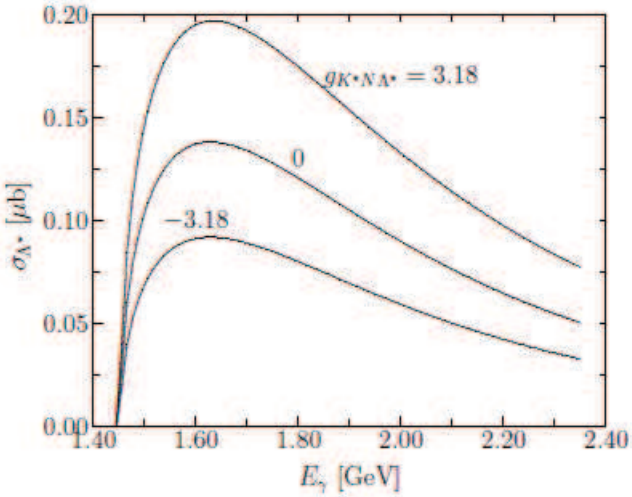

Figure 1.8: The total cross section for $\Lambda(1405)$ photoproduction calculated by Nam *et al.*[27].

Chapter 2

Experiment

The experiment was performed at the SPring-8/LEPS facility. The SPring-8/LEPS facility provides a linear-polarized photon beam with a high intensity and a large degree of polarization. The linear-polarized photons are produced by the backward-Compton-scattering process of laser photons from circulating 8-GeV electrons in the storage ring. Since the energy of the electron beam in SPring-8 is 8 GeV, the photon beam with a few GeV energy can be produced.

The LEPS magnetic spectrometer has been used to detect Kaons. The Kaon tracks are identified by measuring momenta and time-of-flights. The SPring-8/LEPS facility and the LEPS spectrometer are described in detail in this chapter.

2.1 SPring-8 facility

The SPring-8 (Super-Photon ring-8 GeV) is a third-generation synchrotron-radiation (SR) facility which has been completed in 1997. Third-generation facilities are optimized to get a high-brightness SOR light-source by using insertion devices, mainly undulators. There are three third-generation SR facilities with $E_e > 5$ GeV, in the world. They are ESRF (Grenoble), APS (Argonne) and SPring-8 (Japan). SPring-8 is the largest and brightest. The energy of circulating electrons in SPring-8 is 8 GeV.

The accelerator complex of SPring-8 is composed of an injector linac, a booster synchrotron, and a low-emittance and high-brightness storage ring. Figure 2.1 shows the schematic view of the accelerator complex. Electrons are generated at an electron gun and are accelerated to an energy of 1 GeV in the injector linac with a length of 140 m. A 1 GeV electron beam is transported to the booster synchrotron with a 396 m circumference, and are accelerated up to 8 GeV. The 8-GeV electron beam is injected from the synchrotron into the storage ring with a 1436 m circumference and stored.

The 8-GeV electrons circulate in the storage ring with a frequency of 0.2088 MHz. The time interval of the successive bunches for electrons is 1.966 nsec. There are 2436 bunches on the circle in the storage ring. Electrons are filled in some bunches with various filling patterns. The maximum current of the 8 GeV electron beam is 100 mA. The electron beam has a small emittance of $\varepsilon = 6$ nm·rad with the average beam widths of $\sigma_x = 75$ μm and $\sigma_y = 25$ μm in the horizontal and vertical directions.

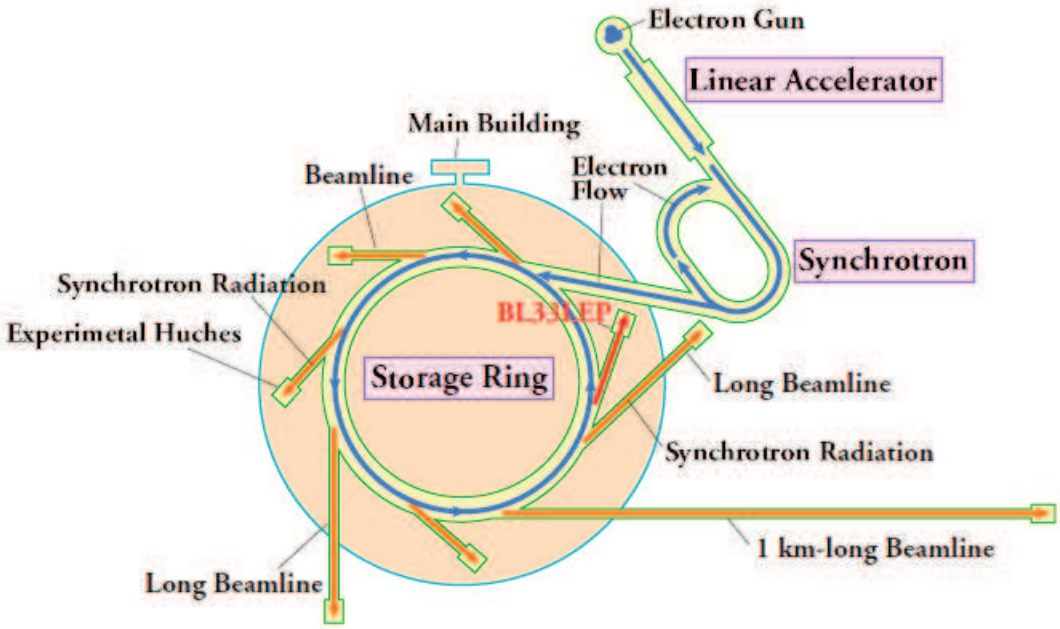

Figure 2.1: Schematic view of the accelerator complex of SPring-8.

2.2 LEPS facility

At the Laser-Electron-Photon facility at SPring-8 (LEPS), a multi-GeV photon beam is produced by the backward-Compton-scattering (BCS) process of laser photons from the circulating 8-GeV electrons [28].

The schematic view of the LEPS beam line is shown in Figure 2.2. The beam line consists of three parts; (a) Laser-electron collision part in the storage (SR) ring, (b) Laser hutch for laser injection, and (c) Experimental hutch where a spectrometer is placed. The BCS process is illustrated in the figure. Laser photons which are optimized in the laser hutch are injected to the storage ring. We have a 7.8 m long straight section between two bending magnets in the storage ring as shown in Figure 2.2. In this straight section, the BCS process takes place if a laser photon collides with a 8-GeV electron. Photons produced by the BCS process are provided to the experimental hutch and irradiate a target. The recoil electrons are detected by a tagging system placed at the exit of the bending magnet to measure the photon beam energy. A series of experiments by using the BCS photon beam started in 2000. The BCS process and devices to produce a linear-polarized photon beam are described in this section.

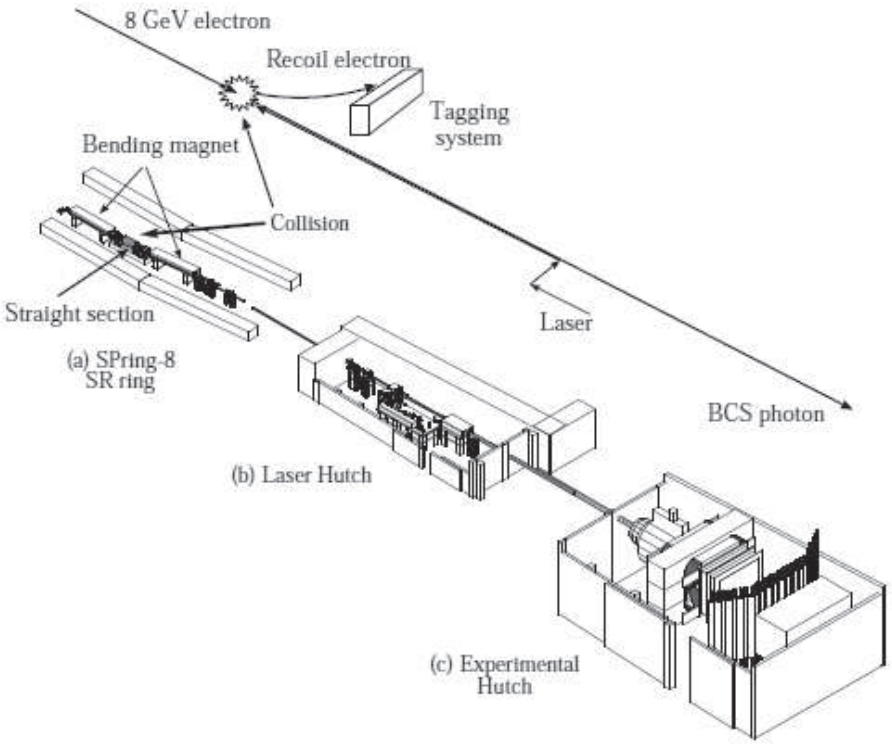

Figure 2.2: Schematic view of the LEPS facility at SPring-8. The facility consists of three parts;(a) Laser-electron collision part in the storage (SR) ring, (b) Laser hutch for a laser injection, and (c) Experimental hutch. A schematic explanation of the collision between an electron and a laser photon in backward-Compton scattering is inserted in the figure.

2.2.1 Backward Compton scattering

The general properties of the backward-Compton-scattering process in the laboratory system are described in this section. Figure 2.3 shows the kinematic values of the backward-Compton-scattering process. If a laser photon with an energy k_1 strikes an electron with a high energy E_e with a relative angle $\theta_1 \simeq 180°$, it is scattered with a scattering angle of θ_2. If $E_e \gg k_1$, the scattered photon is directed strongly in the backward direction due to the Lorentz boost. The scattered photon (BCS photon) gains an enormous energy from the electron by

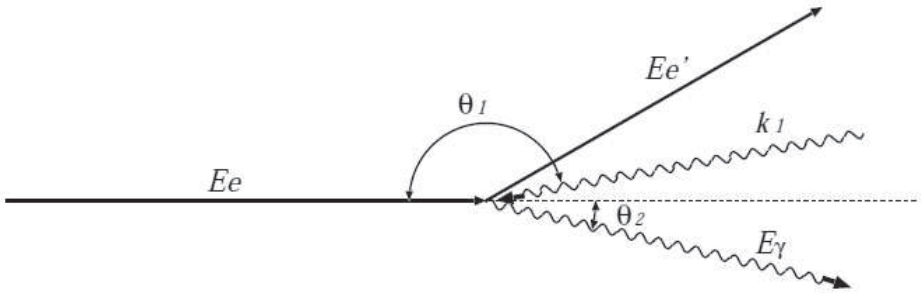

Figure 2.3: Kinematic variables of the backward-Compton-scattering process in the laboratory frame.

the Fitzgerald-Lorentz effect in the recoil process. The energy of a BCS photon E_γ is denoted as

$$E_\gamma = k_1 \frac{1 - \beta cos\theta_1}{1 - \beta cos\theta_2 + \frac{k_1(1-cos\theta)}{E_e}} \tag{2.1}$$

where β is an incident electron velocity in unit of the speed of light and $\theta = \theta_2 - \theta_1$. Assuming $\gamma = E_e/m_e \gg 1$, $\beta \simeq 1$, $\theta_1 \simeq 180°$ and $\theta_2 \ll 1$, Eq. (2.1) can be rewritten as

$$E_\gamma = \frac{4E_e^2 k_1}{m_e^2 + 4E_e k_1 + \theta_2^2 \gamma^2 m_e^2}, \tag{2.2}$$

where m_e is the electron mass of 0.511 MeV and $\gamma \sim 16,000$ at $E_e = 8$GeV. The maximum energy of a BCS photon (Compton edge) is obtained at $\theta_2 = 0°$:

$$E_\gamma^{max} = \frac{4E_e^2 k_1}{m_e^2 + 4E_e k_1}. \tag{2.3}$$

The differential cross section of the BCS process is written as a function of the BCS photon energy [30]:

$$\frac{d\sigma}{dE_\gamma} = \frac{2\pi r_e^2 a}{E_\gamma^{max}} (\chi + 1 + cos^2\alpha) \tag{2.4}$$

$$a = \frac{m_e^2}{m_e^2 + 4E_e k_1} \tag{2.5}$$

$$\chi = \frac{\rho^2(1-a)^2}{1-\rho(1-a)} \tag{2.6}$$

$$cos\alpha = \frac{1-\rho(1+a)}{1-\rho(1-a)} \tag{2.7}$$

$$\rho = \frac{E_\gamma}{E_\gamma^{max}} \tag{2.8}$$

where $\gamma_e = 2.818$ fm is the classical electron radius. Figure 2.4 shows the differential cross sections for the BCS process between 8 GeV incident electrons and laser photons with a wavelength 355 nm. Photons with the sub-GeV energy can be efficiently obtained by the BCS process.

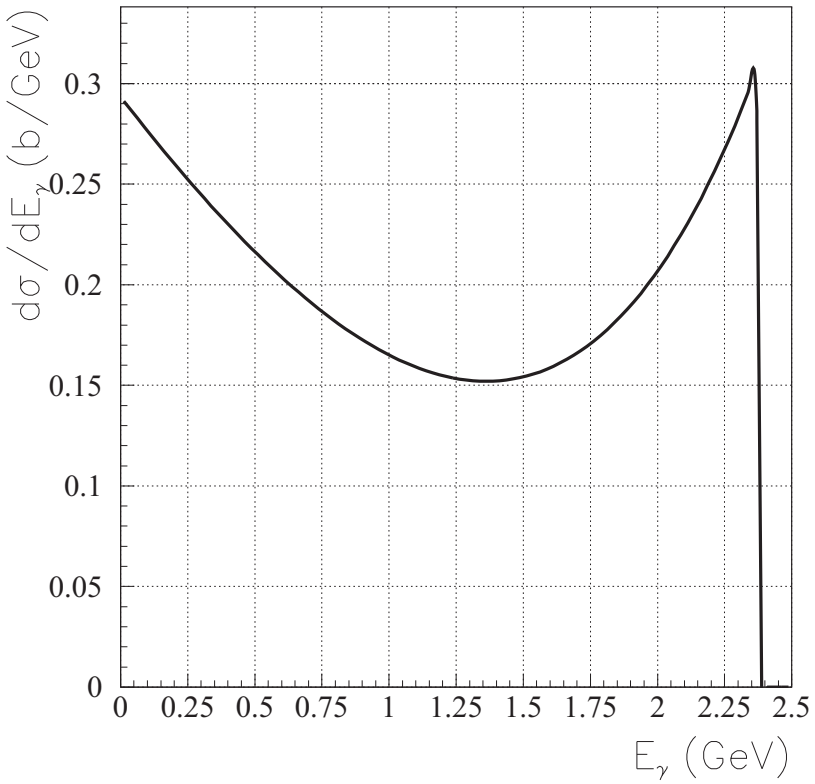

Figure 2.4: Differential cross sections of the BCS process with the 8 GeV incident electron beam for laser photons with a wavelength of 355 nm.

The linear (circular) polarized BCS photons can be made by using linear (circular) polarized

laser photons. When a laser photon is polarized, the polarization is transferred to a BCS photon. The degree of polarization (P_γ) of a BCS photon is proportional to that of a laser photon (P_{laser}) [30]. The linear polarization is given by

$$P_\gamma = P_{laser}\frac{(1-cos\alpha)^2}{2(\chi+1+cos^2\alpha)}. \quad (2.9)$$

The circular polarization is given by

$$P_\gamma = P_{laser}\frac{(2+\chi)cos\alpha}{(\chi+1+cos^2\alpha)}. \quad (2.10)$$

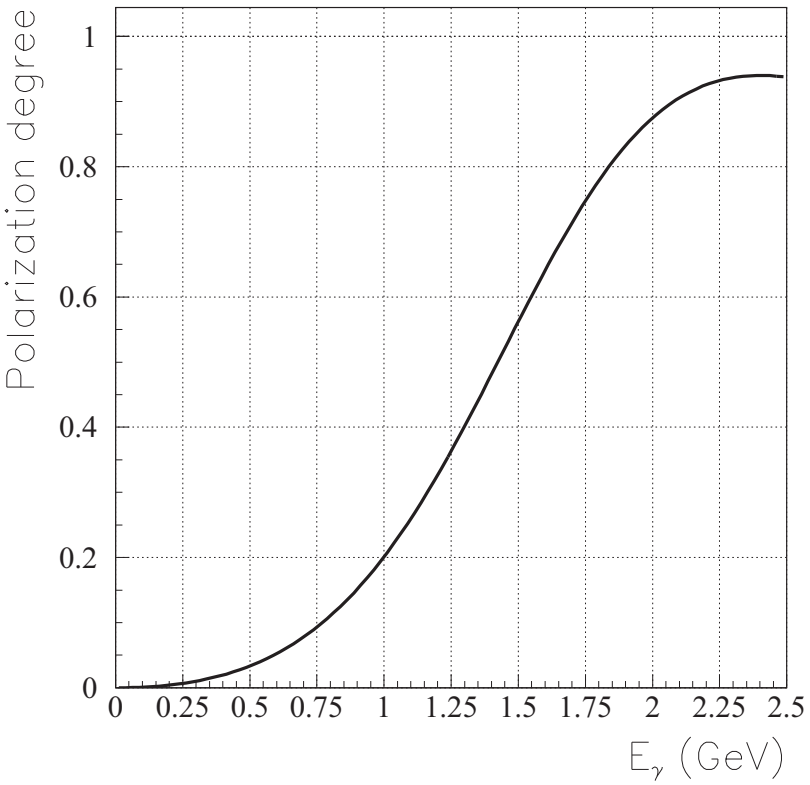

Figure 2.5: Polarization of the BCS photon as a function of E_γ by using the 8 GeV incident electron beam when the laser photon is 100% polarized. The wavelength of the laser photon is 355 nm. (a):Linear polarization and (b):Circular polarization.

Figure 2.5 shows the linear and circular polarizations of a BCS photon as a function of E_γ by using the 8 GeV incident electron beam when the polarization of a laser photon is

100%. The degree of polarization is maximum at the Compton edge ($\theta_2 = 0°$). The spin-flip amplitude for highly relativistic electrons vanishes, and scattered photons almost retain the initial laser polarization at the Compton edge. In the case of the linear polarization, the maximum polarization is obtained as $P_\gamma = P_{laser}\frac{2a}{1+a^2}$ from Eq. (2.9). The linear polarization is about 94% at the maximum energy when the incident electron with $E_e = 8$ GeV and a 355 nm laser with 100% polarization are used.

In the present experiment, a linear-polarized photon beam was produced by a laser with a wavelength of 257 nm and that with a wavelength of 355 nm . The experiment started with a laser with a wavelength of 257 nm (Coherent Sabre). However, Sabre laser system was broken in the middle of the experiment (9th July 2008). Then it was replaced with a laser with a wavelength of 355 nm (Coherent Paladin). The size of the BCS photon beam was obtained to be $\sigma_x \sim 3.5$ mm and $\sigma_y \sim 2.0$ mm. The size difference between σ_x and σ_y is due to the emittance of the 8-GeV electron beam.

2.2.2 Laser operating system

Figure 2.6 shows the schematic view of the laser system. Laser photons from two laser systems can be injected into strage ring simultaneously in order to achieve high intensity of LEP beam. In this experiment, one laser injection was performed.

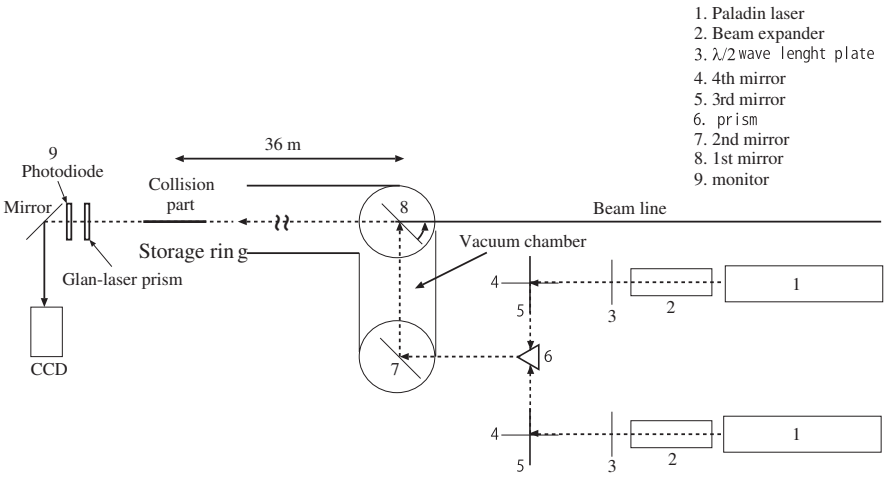

Figure 2.6: Schematic view of the laser operating system

In this experiment, Ar laser (Coherent Sabre) and , solid-state laser (Coherent Paladin) were used as a photon source. The laser oscillates with a single line mode with a wave length of 257 nm for Sabre and 355 nm for Paladin. The maximum LEP beam energy is about 2.975 GeV for Sabre and about 2.385 GeV for Paladin. The size of the laser beam is 1mm ϕ. The laser beam is vertically polarized. The beam intensity was typically 100kcps for Sabre and 1 Mcps for Paladin. The energy spectrum of the LEP beam measured by Tagging system are shown in Figure 2.7.

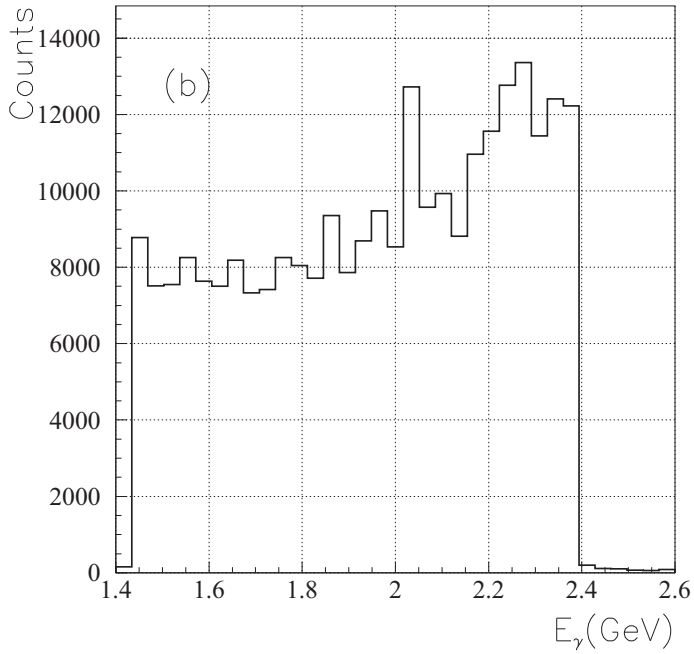

Figure 2.7: The energy spectra of LEP beam for the photon beam with maximum energy of 2.4 GeV.

The laser beams travel about 36 m before they collide with electron beam. The beam expanders are used to tune the beam size at the collision point. The beam expanders enlarge and focus the laser beams by a concave lens and a convex lens made of UV grade quartz. The magnification factor of the expander is 28 (laser beam size after the expander is 28 mm).

The polarization of the laser beams are controlled by the $\lambda/2$ plates. Since the laser beams are vertically polarized, the optic axis of the $\lambda/2$ plates are set to be 0 degree when vertically polarized photons are used and set to be 45 degree when horizontally polarized photons are used. The polarization of the laser was changed once a day for data taking with Paladin. On the other hand, vartical polarization was kept for data taking with Sabre because beam intensity was low for Sabre and it was higher for vertically polarized photon than for horizontally polarized photon.

Four mirrors and one prism is used to guide the laser beam to the storage ring. The angle of 4th and 3rd mirrors are controlled by pulse motors to tune the direction of the laser beams. The 4th and 3rd mirrors are made of quartz with a size of 80 $\phi\times$ 12 t (mm). Two laser beams are reflected by both sides of the prism and guided to the 2nd mirror. Prism is made of quartz. Figure 2.8 shows the schematic view of the prism. The 2nd mirror and 1st mirror are put inside the vacuum chamber. They are made of Si base with aluminum coating which have good heat conductivity. Size of 2nd mirror is 100 $\phi \times$ 19 t (mm) and that of 1st mirror is $100\phi \times 6t(mm)$. 1st mirror is made thin because LEP beam pass it. 1st mirror is cooled by water circulation.

The polarization of the laser photons is measured by using laser photons which pass through the collision part. A Glan-laser prism is used as a polarimeter to measure the polarization. The Glan-laser prism has a special axis. Only photons with the polarization parallel to this axis can pass through the prism. By rotating the prism and measuring the intensity of the laser beam after the prism, the intensity distribution of the laser beam is obtained as a function of the rotation angle ϕ. The intensity is measured by a photo-diode (HAMAMATSU S1406-05). Figure 2.9(a) and (b) show the intensity distribution measured by the photo-diode for vertically and horizontally polarized laser photons. The data is fitted by a function of $\sin\phi$. The polarization angle and degree are determined by this fitting. The laser beam is optimized to have the maximum polarization.

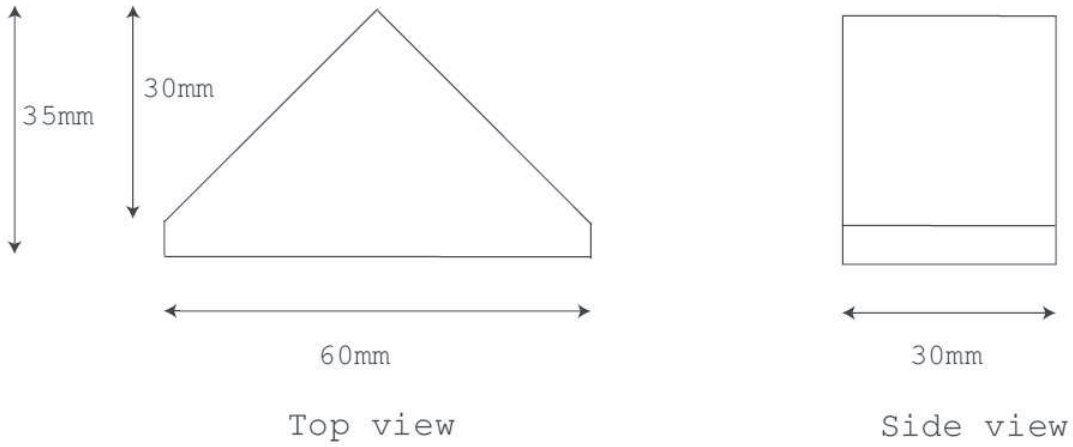

Figure 2.8: Schematic view of the prism

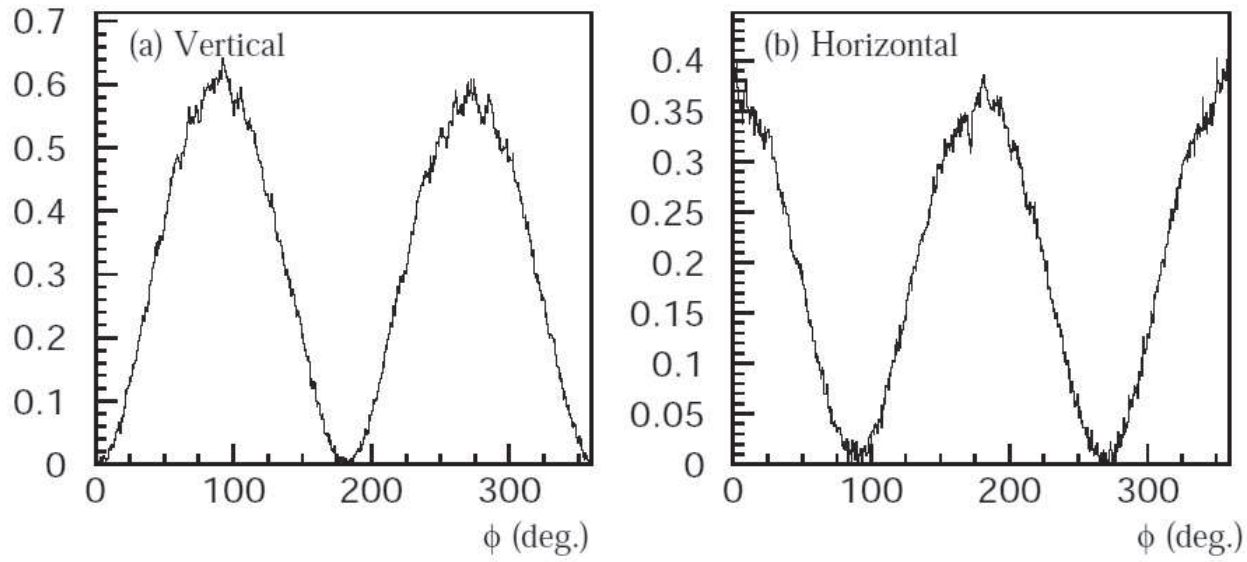

Figure 2.9: Intensity distribution of the laser beam measured by the photo-diode for (a) vertically polarized laser photons and for (b) horizontally polarized laser photons. The distribution is fitted by a function of sinϕ.

2.3 Tagging system

The energy E_γ of the BCS photon beam is determined by the recoil electron energy $E_{e'}$ as

$$E_\gamma = E_e - E_{e'}. \tag{2.11}$$

The energy of the 8-GeV circuiting electron E_e was calculated on the basis of measured field distributions of magnets in the storage ring. The energy was determined as 7.975 $\pm$ 0.003 GeV [31]. The energy $E_{e'}$ is measured by a tagging system located in the storage ring. Since an electron scattered by the BCS process looses its energy, it is relatively strongly bent and deviates from the normal orbit in the 8-GeV ring when it passes through the bending magnet placed at the end of the straight section (see Figure 2.2). The tagging system is installed at the exit of the bending magnet to detect the recoil electrons.

Figure 2.10 shows the structure of the tagging system. The tagging system is placed at the outside of a beam vacuum pipe for the 8 GeV electron beam. The tagging system covers a region 4.0 - 6.6 GeV in the energy of recoil electrons. This energy region corresponds to the energy of the BCS photons 1.5 - 3.0 GeV. The lower limit of 1.5 GeV is due to the fact that the tagging system can't be positioned closer to the nominal orbit of the 8 GeV electrons.

A hit position of an electron track is measured by the TAG-SF. The TAG-SF consists of two layers (TAG-SFF and TAG-SFB). Each fiber layer consists of 55 fiber bundles. Each fiber bundle is made of six fibers with the cross section of 1×1 mm^2. A schematic view of the fiber is shown in Figure 2.11. There exist 4.2 % inefficient region in one fiber. Two layers are arranged with an overlap of 0.5 mm to cover the inefficient region of the one layer. The signal from fiber bundles are read by PMT (HAMAMATSU R5900-00-M4, H6568-10).

The trigger of the tagging system is cleaned up by taking a coincidence of the TAG-SF and the TAG-PL. TAG-PL consists of 2 layers of 5 plastic scintillation counters. The size of the plastic scintillator is 10.0 mm high, 7.4 mm wide, and 3.0 mm thick. The plastic scintillator which is closest to the 8-GeV electron beam has the width of 5.5 mm. The plastic scintillators are arranged with an overlap of 2.7 mm. The signal of the TAG-PL is read through the photo-multiplier-tube (HAMAMATSAU H3164-10).

2.3.1 Beam line setup

The BCS photon beam travels from the collision point to the experimental hutch through the laser hutch. Figure 2.12 illustrates the setup of the beam line. There are some materials in the path of the photon beam. They are the first mirror, aluminum windows of the beam pipes and a X-ray absorber. When the photon beam hits these materials, some of photons convert to e^+e^- pairs. The materials and their conversion rate to e^+e^- pairs are summarized in Table 2.1. The first mirror is made of silicon with a thickness of 6 mm. Since the mirror is tilted by 45° to inject laser photons into the storage ring, the effective thickness is thus $6 \times \sqrt{2}$ mm. Capton sheets are used as windows of beam pipes, the exit of a beam pipe from the SR ring, and the enter and exit of a beam pipe which connects the laser hutch and experimental hutch. An Al plates is used in total in the beam line. A lead absorber with a thickness of 2.0 mm is placed after the beam pipe from the SR ring to absorb X-rays. The detectors of a spectrometer are protected with this absorber from a radiation damage. The thickness of 2.0 mm is determined by the operation of the detectors and the radiation safety. The conversion rate of the photon

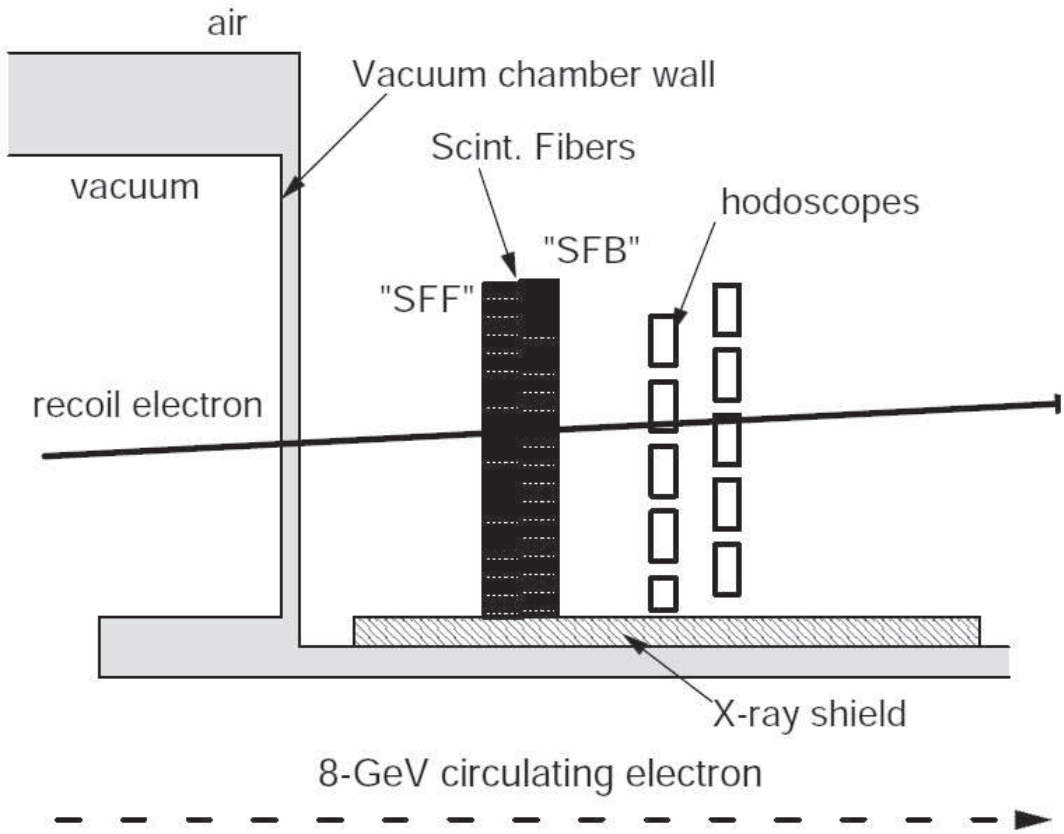

Figure 2.10: Schematic view of the tagging system

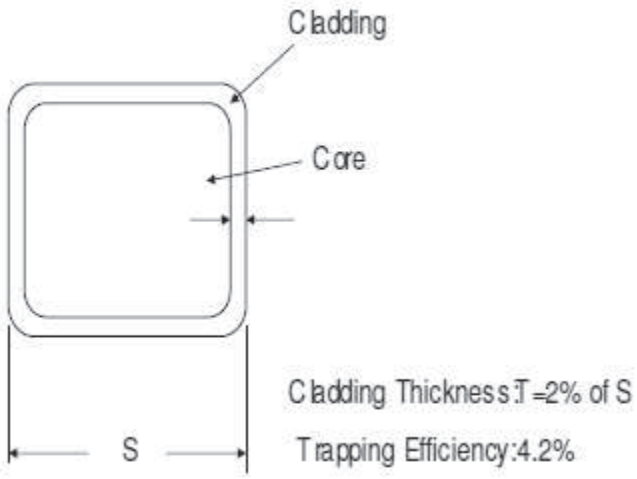

Figure 2.11: Schematic view of the fiber

beam is 32.5 % in total. The intensity of the photon beam is reduced by about 32.5 % before it arrives at a target in the experimental hutch. The transmission of the photons from the reaction point to the target was measured by the tagging counter and gamma counters. The electron with a energy of around 6.7 GeV, which corresponds to the photon energy of around 1.3 GeV, hits the wall of the shield and create electro magnetic shower. Although the shower events hits Tagging counter, these events are discarded at the analysis. The measured effective transmission including the effect of shower is around 53 %.

Table 2.1: Materials inserted in the beam line.

	Material	Radiation length (mm)	Thickness (mm)	Conversion rate (%)
First mirror	Si	93.6	$6\times\sqrt{2}$	6.77
Vacuum windows	Al	89.0	0.55×3	0.44×3
Absorber	Pb	5.6	2.0	24.25

The e^+e^- pairs created in the materials should be removed before a target. To remove the e^+e^- pairs, we use a sweep magnet located in the laser hutch. Figure 2.13 shows the structure of the sweep magnet. The size of the iron yoke is 176 mm high, 560 mm wide, and 1000 mm long. Two permanent magnets are installed in the iron yoke. The size of each magnet is 35 mm high, 58 mm wide, and 1000 mm long. They are faced with a gap of 44 mm. The strength of the magnetic field is 0.6 T at the center. The e^+e^- pairs produced at the first mirror, the aluminum window, the X-ray absorber and the residual gas in the beam pipe are removed from the beam line by the sweep magnet. Lead collimaters are placed at the upstream and downstream positions of the sweep magnet. The thickness of the upstream

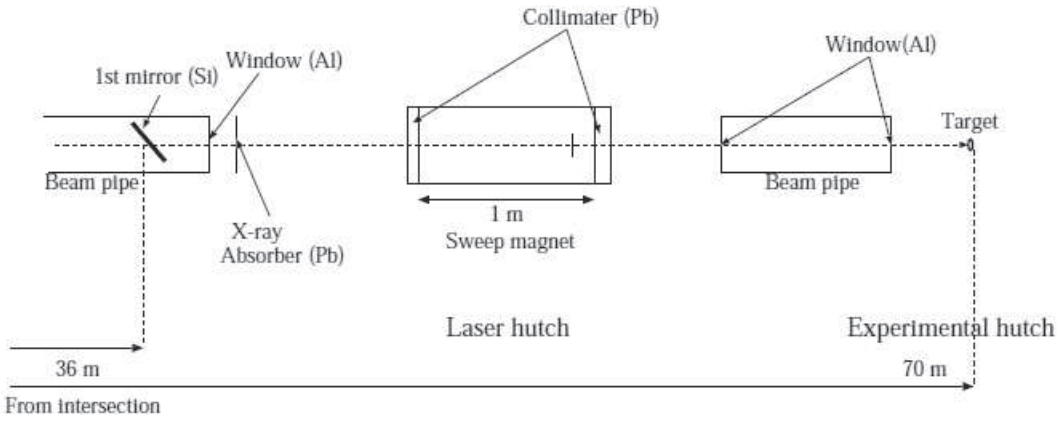

Figure 2.12: Schematic view of the LEPS beam line setup.

(downstream) collimaters is 50 (150) mm. The upstream (downstream) collimaters have a hole with a diameter of 20 (25) mm. The e^+e^- pairs with a momentum below 2.1 GeV/c are blocked by the downstream collimator. The other e^+e^- pairs with a momentum above 2.1 GeV/c pass through the hole of the downstream collimator.

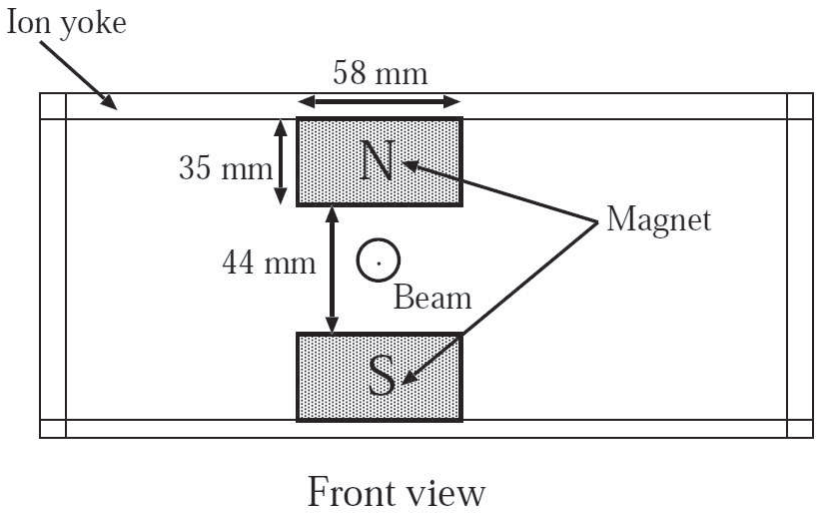

Figure 2.13: Structure of the sweep magnet.

2.4 LEPS spectrometer

The LEPS spectrometer is located in the experimental hutch to identify charged particles produced at the target. Figure 2.14 shows the LEPS spectrometer. The incidence direction

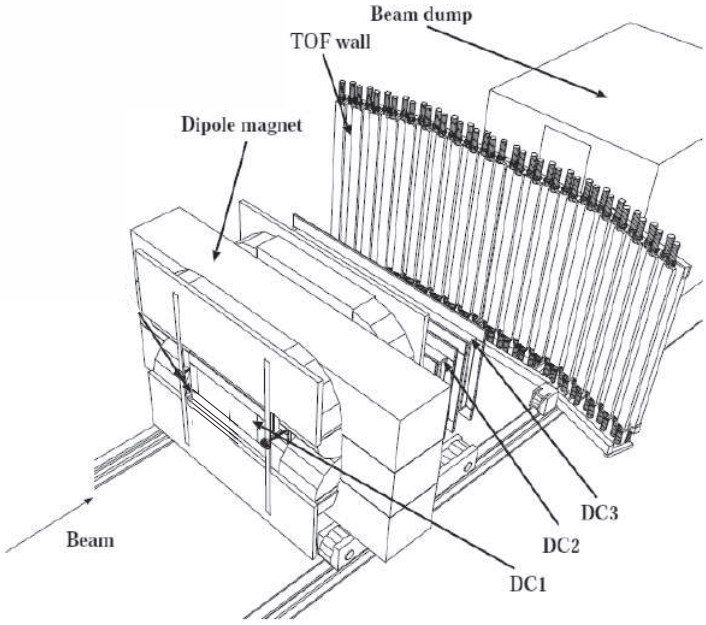

Figure 2.14: Overview of the LEPS spectrometer.

of the photon beam is displayed in the figure. The LEPS spectrometer consists of trigger counters, a dipole magnet, four drift chambers (DC0, DC1, DC2 and DC3), and a TOF wall. Charged particles produced at the target are defined by the trigger counter. The four drift chambers are used as tracking devices with the dipole magnet to measure momenta of charged particles. A time-of-flight is measured by using the TOF wall. A beam dump is placed behind the spectrometer for the purpose of a radiation shielding.

2.4.1 Trigger counters

Upstream-veto counter

The photon beam is partly converted to e^+e^- pairs until achieving to the target in the air in beam line, Al windows of the beam pipe or the collimators. These e^+e^- pairs were identified using the upstream veto counter, and vetoed at the trigger level. This counter is a plastic scitillator located at just downstream of the buffer collimator in the experimental hatch. The

size is 620mm high, 620mm wide, and 3 mm thick. A 2-inch fine-mesh PMT is connected to the plascit scintillator through a light guide.

Inner counters

The liquid hydrogen target was surrounded by six plastic scintillation counters. These inner counters are used to detect the charged particles nearby the target and to determine the start timing of trigger. The size of a scintillator is 230mm long and 542mm wide. The thickness is 3 mm. A scintillator is bent with 30 degree at 170mm-long to detect forward-going particles and has tapered shape to be combined with other inner scintillators in hexagonal shape. A fine-mesh PMT is attatched to one side of a scintillator through fiber light guides. Figure 2.15 and 2.16 show a schematic view of an inner scintillator and a photograph of the combined inner scintillators, respectively.

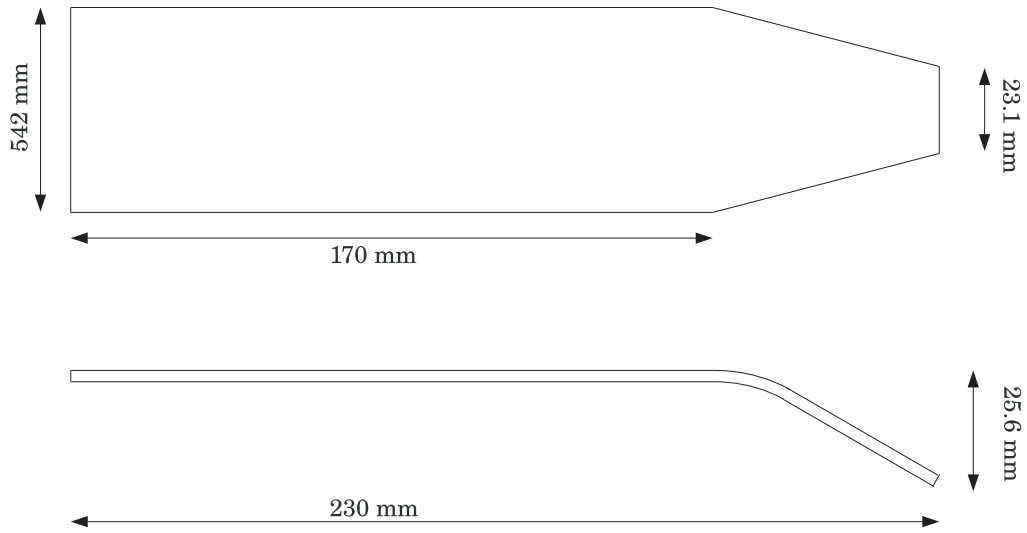

Figure 2.15: A schematic view of an inner scintillator.

Outer counters

Twelve plastic scintillation counters were set around the TPC. These outer counters detect the charged particles from the target. The conincidence signal of inner counters and outer counters makes logical trigger. The size of a scintillator is 850mm long and 145mm width. The

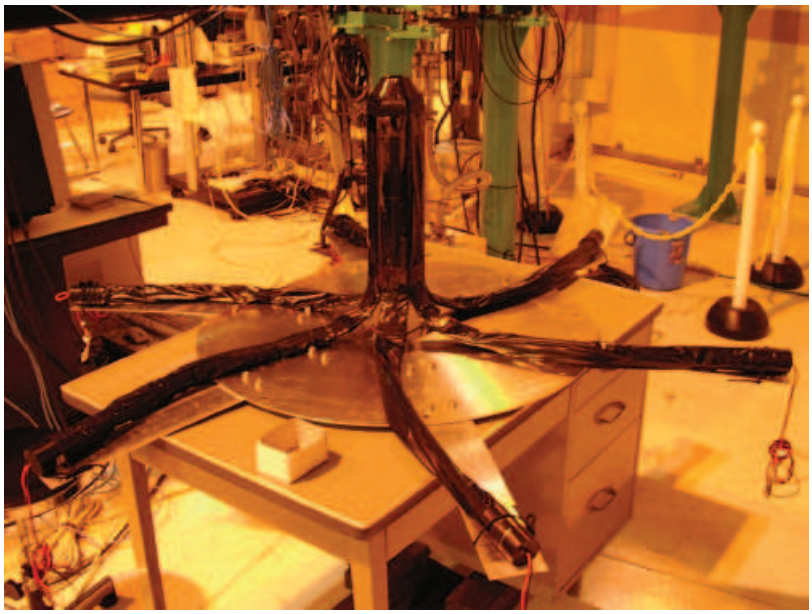

Figure 2.16: Picture of combined inner scintillation counters.

thickness is 5 mm. Two fine-mesh PMT's are attached to a scintillator through light guides. Each side of the TPC is covered by two outer scintillators.

The configuration of inner counters and outer counters is shown in Figure 2.18.

Figure 2.17: Picture of outer scintillation counters.

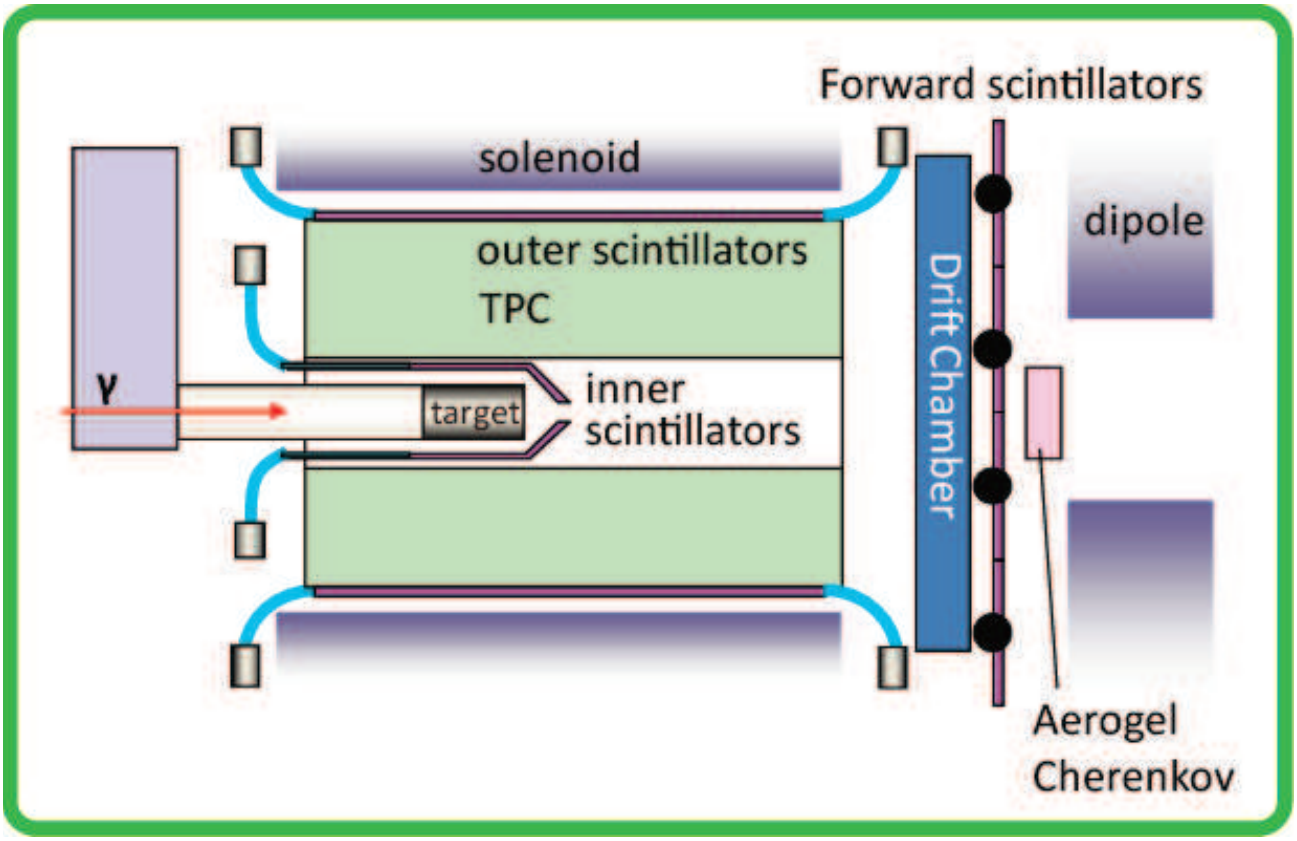

Figure 2.18: Inner scintillation counters and outer counters

2.4.2 e^+e^- Blocker

The e^+e^- pairs produced at the target spread out mostly in the median plane by the magnetic field in the dipole magnet because they emerge with a small angle. Some of electrons or positrons with a low energy come out beyond the acceptance of the beam dump which is located behind the spectrometer, and hit directly thin walls of the experimental hutch. This causes a problem in terms of radiation safety. The e^+e^- blocker is used in the dipole magnet to block low energy particles. The schematic view of the e^+e^- blocker is shown in Figure 2.19.

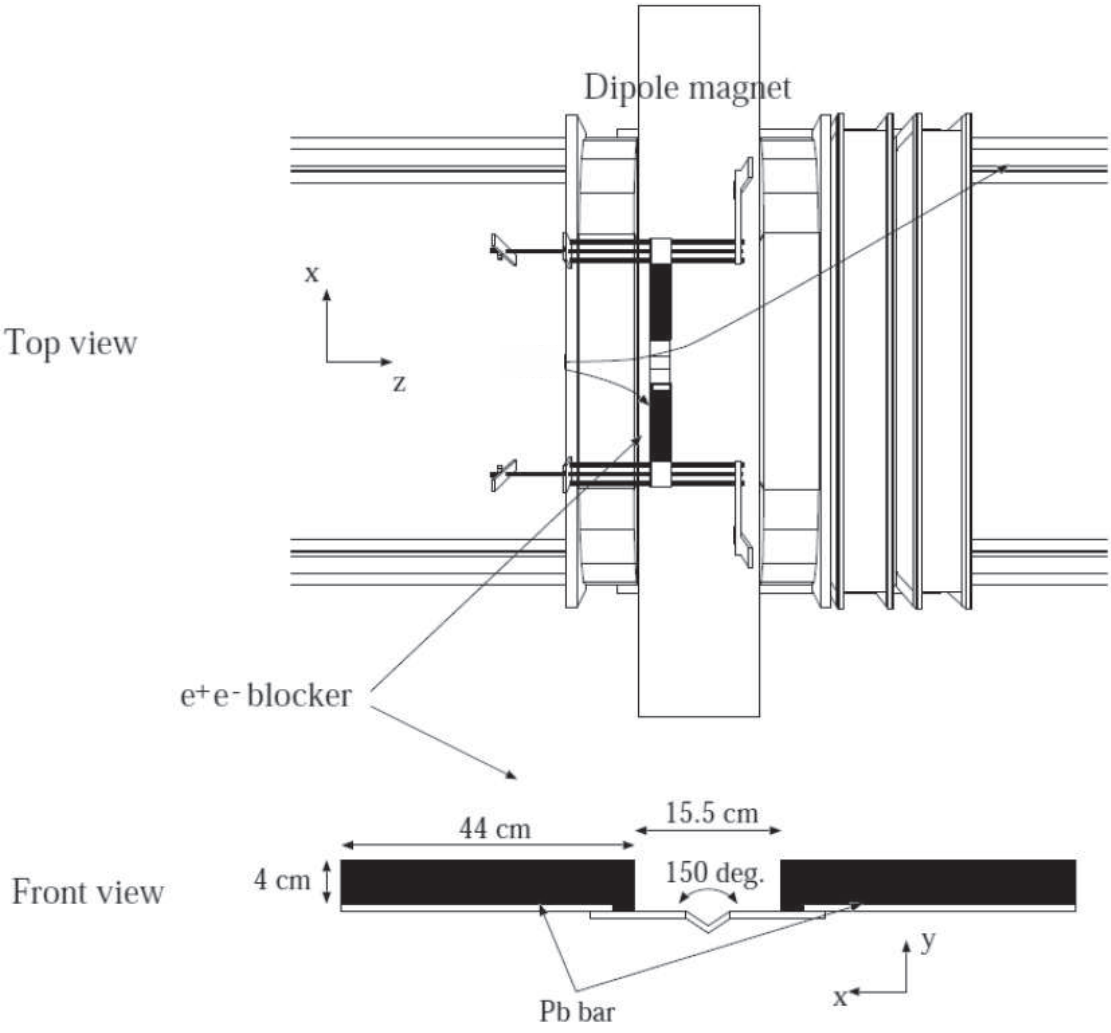

Figure 2.19: Drawing of the e^+e^- blocker.

The e^+e^- blocker with two lead bars is placed 20 cm downstream of the center of the dipole magnet. The size of each Pb bar is 4 cm high, 44 cm wide, and 10 cm thick. The gap distance

between two Pb bars is 15.5 cm. The e^+e^-'s with above 1 GeV/c momentum can go through the gap. The gap distance can be changed by using the small pieces of the Pb blocks. The e^+e^- pair emerges mostly asymmetrically in energy. In most cases, one of pairs is blocked by the blocker, while the other survives and escapes through the 15.5 cm gap and is stopped by the beam dump. The Pb bars are supported by two thin channels with a 0.2 cm thickness. A V-shaped thin bar (SUS) with a thickness of 0.5 cm connects a thin channel with one another in the center. The V-shape structure opens at 150° and has 1.5 cm in depth to let the photon beam pass through (see Figure 2.19). The blocker is put down by the weight itself and the center in the y-direction is -7 mm.

2.4.3 Drift chambers

A tracking of a charged particle is performed by using hit information from four MWDC's (multi wire drift chambers). DC0 and DC1 are located upstream of the dipole magnet. DC0 has the active area of 600 mm diameter and 6 wire planes, y1,y2,u1,u2,v1 and v2. The inclination angle of the y, u and v wires are 0°, 60° and 120° with respect to the horizontal plane, respectively. One wire plane of DC0 consists of sense wires and field wires. The distance between two sense wires is 14 mm. The wire planes are positioned with 14 mm spacing. Cathode planes made of Alminized mylar (12.5 μm thick) are installed between wire planes. DC1 has the active area of 600 mm $\times$ 300 mm. Figure 2.20 shows a drawing of field, shield and sense wires in DC1. DC1 has 6 planes, x1, x2, u1, u2, v and x3. The x3 wires are made additionally because a charged particle begins to be spread out by the magnetic field in DC1. Sense wires of x1-x2 and u1-u2 are positioned with a 6 mm spacing and wires of x3 and v are positioned with a 12 mm spacing. The field wires are arranged in a hexagonal shape. The shield wires are positioned along the windows to shape the electric field. The inclination angle of the u and v wires is 45° with respect to the horizontal plane. DC2 and DC3 are installed downstream of the dipole magnet and have the active area of 2000 mm $\times$ 800 mm. Both DC2 and DC3 have 5 planes, x1, x2, u1, u2 and v. The design of DC2 and DC3 is the same as DC1 as shown in Figure 2.20, but there is no x3 wires in DC2 and DC3. Sense wires of x1-x2 and u1-u2 are positioned with a 10 mm spacing, and the wires of v are positioned with a 20 mm spacing. The u and v direction are inclined by 30° with respect to the vertical plane. The material of the sense wires is gold-plated tungsten (Au-W) and the wire diameter is 25 and 30 μm for DC1 and DC0, DC2, DC3, respectively. The field and shield wires are made of Au-BeCu with a diameter of 80 μm and 100 μm for DC0 and DC1, DC2, DC3, respectively. The windows are made of mylar with a thickness of 125 μm. The design parameters of the DC's are shown in Table 2.2. The gas mixture used to operate the DC's is 70 % argon and 30 % isobutane. The efficiency is more than 98% and is typically 99%.

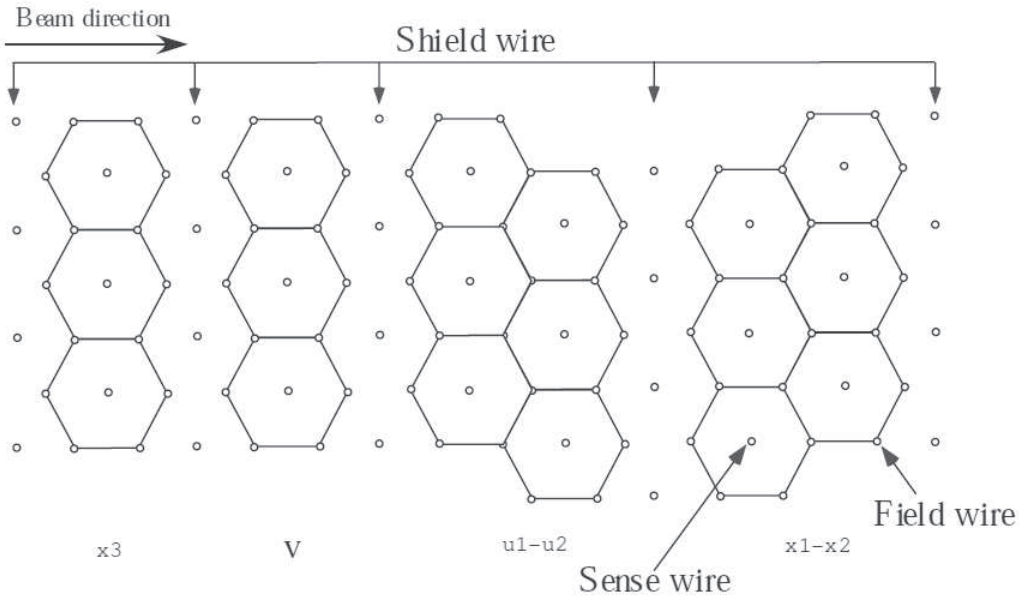

Figure 2.20: Drawing of field, shield and sense wires in the multi wire drift chamber, DC's.

Table 2.2: Design parameters of the MWDC's. The location of the center of each DC is along the z-axis. The location of z=0 is defined as the center of the dipole magnet.

	Coordinate	Orientation	Number of sense wire	Wire spacing (mm)	Active area	Location z (cm)
DC0	y1-y2	90°	48	14	ϕ600 mm	-832.0
	u1-u2	30°	48	14		
	v1-v2	150°	48	14		
DC1	x1-x2	0°	48	6	x = 600 mm	-466.0
	u1-u2	45°	48	6	y = 300 mm	
	v	135°	48	12		
	x3	0°	48	12		
DC2	x1-x2	0°	104	10	x = 2000 mm	860.5
	u1-u2	120°	78	10	y = 800 mm	
	v	60°	79	20		
DC3	x1-x2	0°	104	10	x = 2000 mms	1260.5
	u1-u2	120°	78	10	y = 800 mm	
	v	60°	79	20		

2.4.4 TOF wall

Time-of-flights of charged particles are measured by a TOF wall. The TOF wall is placed downstream of the DC3 with a full angular coverage of the LEPS spectrometer. Figure 2.21

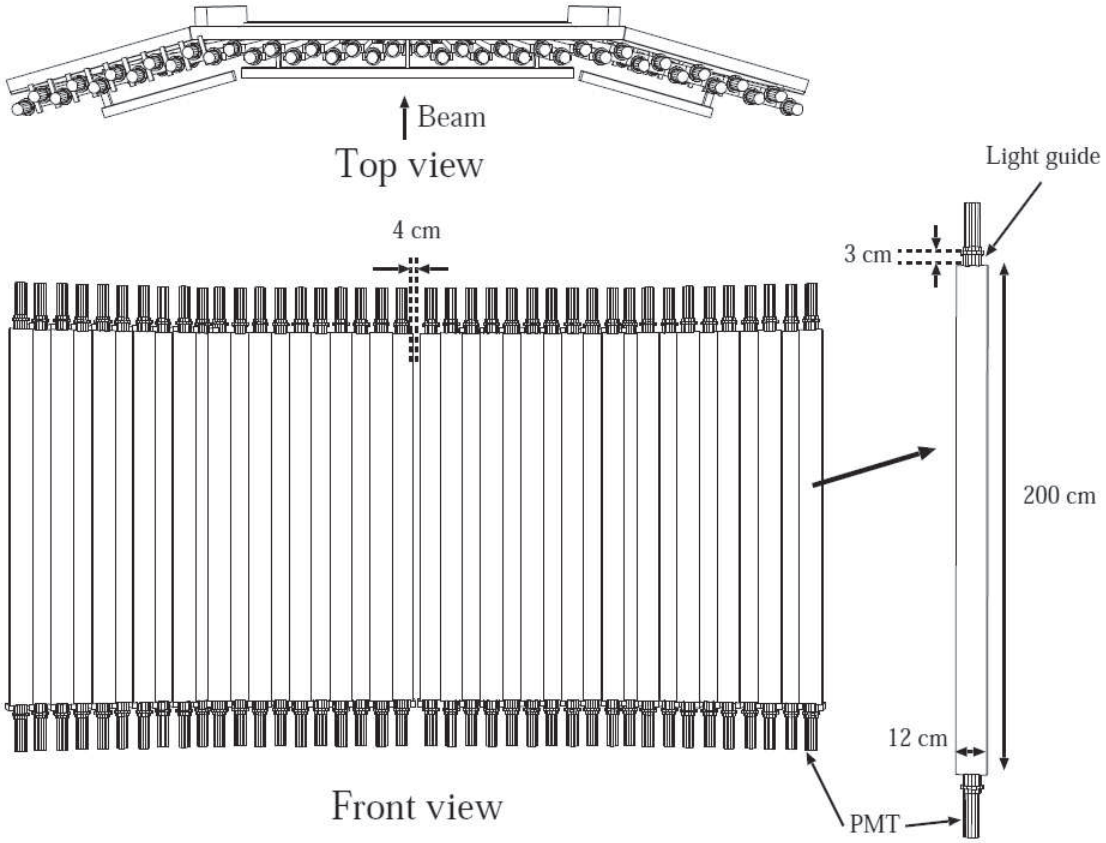

Figure 2.21: Drawing of the TOF wall.

shows a schematic view of the TOF wall and drawing of a TOF counter. The TOF wall consists of 40 plastic scintillator bars (BC-408). The size of a plastic scintillator bar (TOF counter) is 200 cm long, 12 cm wide, and 4 cm thick. Two 2-inch PMT's (HAMAMATSU H7195) are attached to both sides through a light guide with a thickness of 3 cm. Each bar is overlapped with adjacent bars by 1 cm. Sideway bars are aligned in the planes tilted by $\pm$ 15 degrees as shown in the top view of Figure 2.21. Ten bars are arranged in the right side and ten bars are placed in the left side. A 4-cm gap between the two TOF counters at the center allows for the photon beam to pass through. The TOF wall is movable on the rails between 1.5 and 4.5 m away from the center of the dipole magnet. In the present experiment, the z-position of the TOF wall was set at 3151.5 mm away from the center of the dipole magnet.

2.4.5 Dipole magnet

A dipole magnet is used as a momentum analyzer magnet to bend charged particles. The magnet is placed at the center of the spectrometer. The magnet has an aperture with 55 cm high and 135 cm wide. The length of the pole along the beam is 60 cm. Figure 2.22 shows the

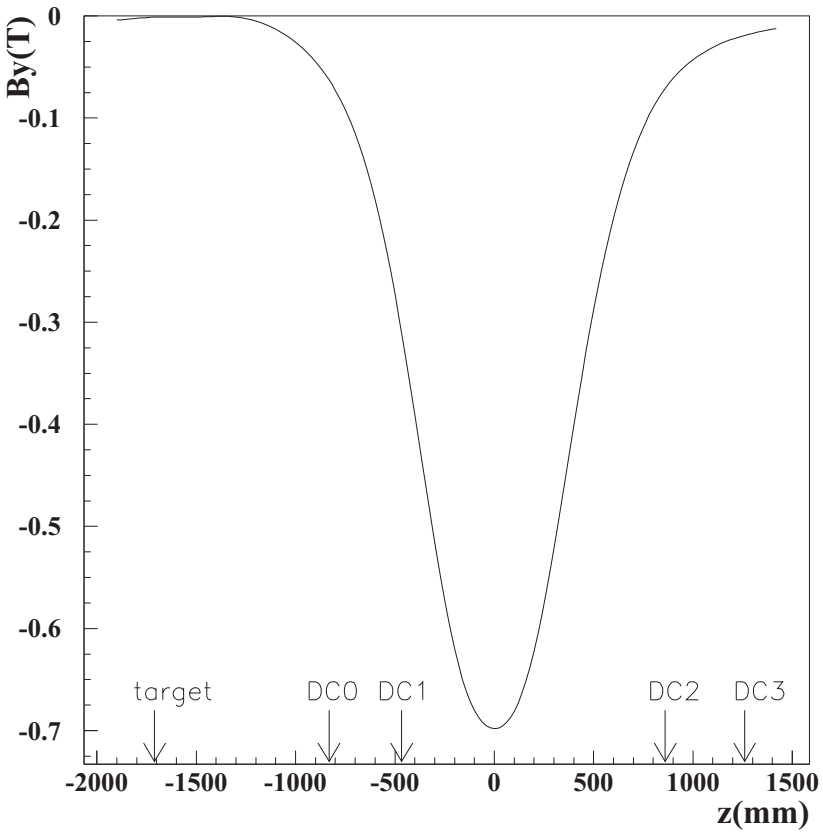

Figure 2.22: Distribution of the magnetic field B_y as a function of the z-position at x=0 and y=0. The position of z=0 corresponds to the center of the dipole magnet.

distribution of the magnetic field B_y along the y-direction as a function of the z-axis at x=0 and y=0. We used the TOSCA simulation program to obtain the distribution. The magnetic field was measured with a hole probe and the measured distribution was compared with the result obtained by the TOSCA simulation. They show a good agreement and then we used the distribution of the magnetic field obtained by TOSCA in the tracking. The direction of the magnetic field is from down to up. The strength of the magnetic field is 0.7 T (1.1 T) at the center when the current is set at 800 A (1510 A). The current was set at 800 A for the present experiment.

2.4.6 Solenoid magnet

A superconducting solenoid magnet was used to momentum-analyze the charged particles detected by the TPC. The magnitude of the magnetic field was 2 Tesla at the center of the magnet. The solenoid magnet has an aperture of 300 mm in radius. The center of the magnet was placed at -1617 mm along the beam axis from the center of the dipole magnet. The center of the target was at -1710 mm. The magnetic field was measured with a hole probe and the measured distribution was compared with the result obtained by the TOSCA simulation. The distribution of the magnetic field obtained by TOSCA was used in the tracking. Figure 2.23 shows the distribution of the z-component of the magnetic field, B_z, calculated by TOSCA as a function of the z-coordinate on the beam axis (x=0,y=0).

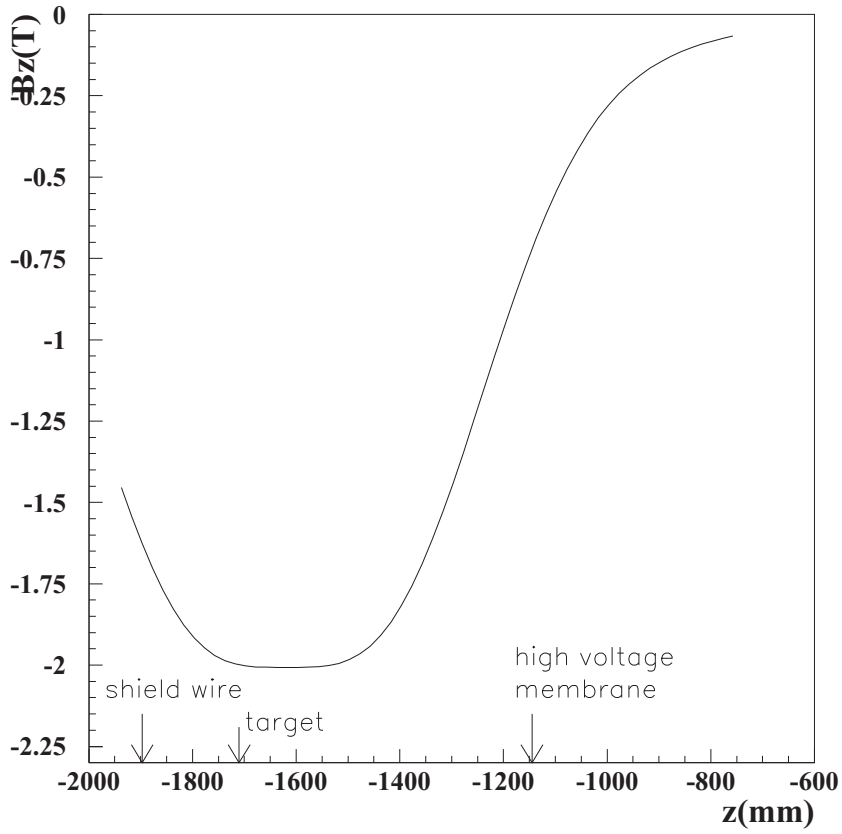

Figure 2.23: Distribution of the z-component of the solenoid magnetic field B_z as a function of the z-coordinate on the beam axis (x=0,y=0).

2.4.7 RF signal

The 508 MHz radio frequency (RF) system is used in the 8-GeV storage ring to recover the energy loss of circulating electrons due to synchrotron radiation. A time interval of the successive bunches of the RF to accelerate the electrons is 1.966 nsec. The RF signal is used to determine a start timing for the time-of-flight measurement. Figure 2.24 shows a circuit diagram for the RF signals. The prescaler modules are 17K32 508-MHz 30 bit counters made by DIGITAL LABORATORY. The RF signals are prescaled with a factor 1/87. Three output logic signals are made. Two output signals are read by the FASTBUS TDC 1875S module and are used in the time-of-flight measurement. One output signal is delayed by 86 nsec relative to the other signal. The RF logic signal and the delayed signal are prepared to prevent the event loss due to the dead time of the trigger timing. The other signal from the prescaler with a factor 1/87 is read by the prescaler module with a prescale factor of 1/28. Three output signals are made. The two output signals are delayed by 1.8 μsec and 3.6 μsec relative to the other signal. These three signals are read by the FASTBUS TDC 1877A module. The data was used to study the accidental rate in the tagging system.

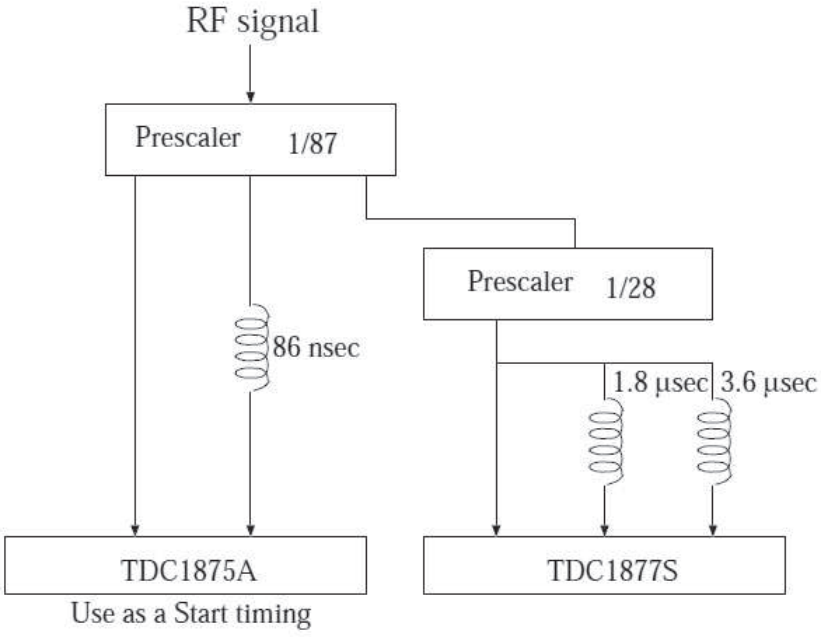

Figure 2.24: Circuit diagram for RF signals

2.5 The liquid hydrogen target

A liquid hydrogen target was used in the experiment. Figure 2.25 and 2.26 show a schematic view of the target system and that of the target cell, respectively. The target system has a long nose. The length of the nose is 700 mm. The target cell is attached at the distal end of the nose. The target cell has a cylindrical shape and is made of capton film. The length of the cell is 150 mm and the diameter is 40 mm. The target cell was covered by a CFRP cap in order to maintain as a vacuum and reduce materials around the target cell. The thickness of the CFRP cap is 1 mm. The nose of the target system was inserted into the inner bore of the Time Projection Chamber and the center of the target cell was located at the 1710 mm upstream of the center of the dipole magnet.

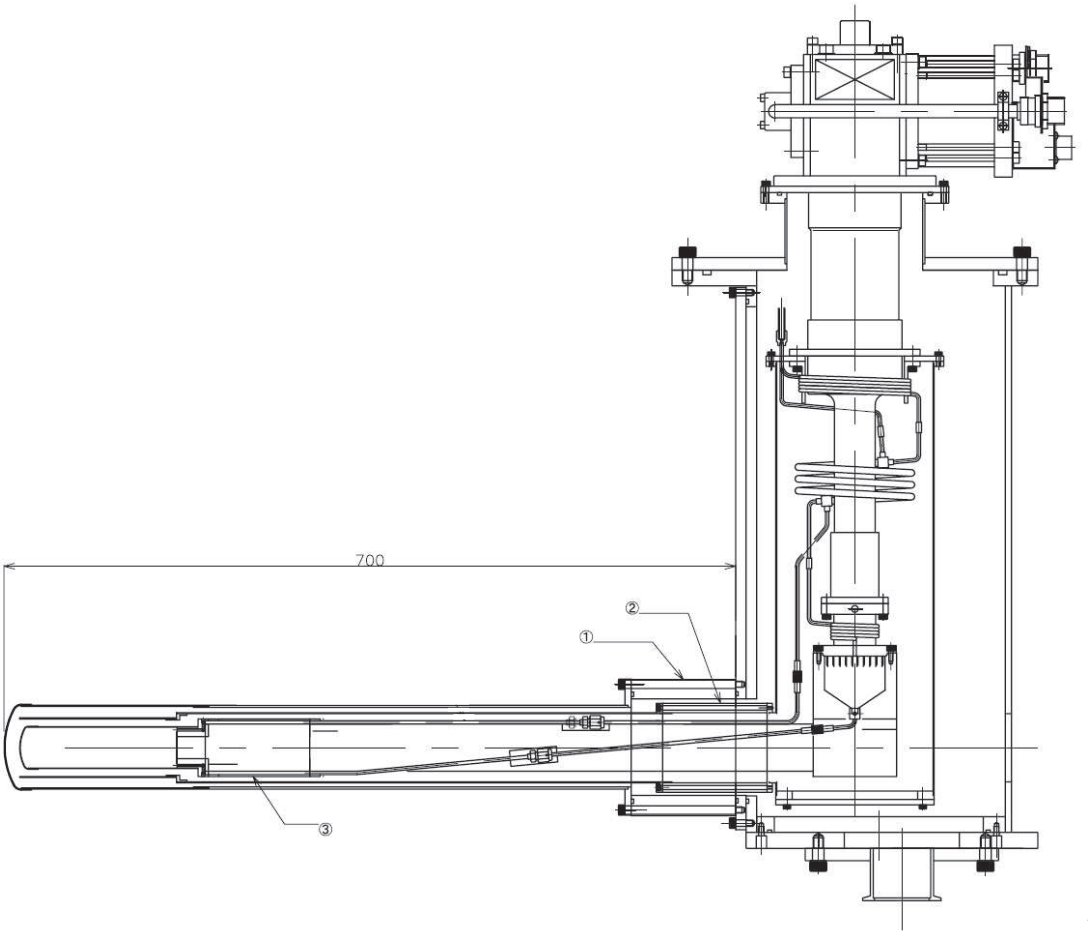

Figure 2.25: A schematic view of the liquid target system.

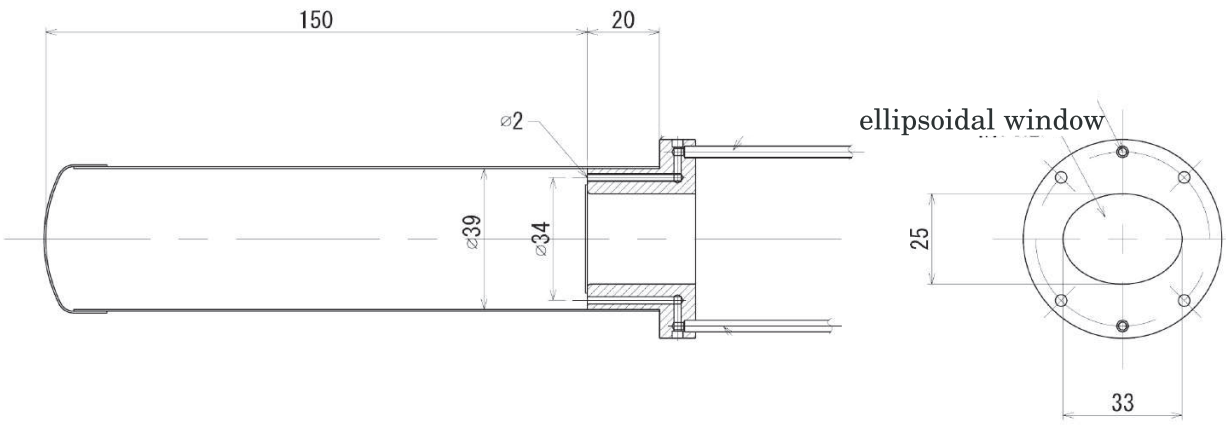

Figure 2.26: A schematic view of the target cell.

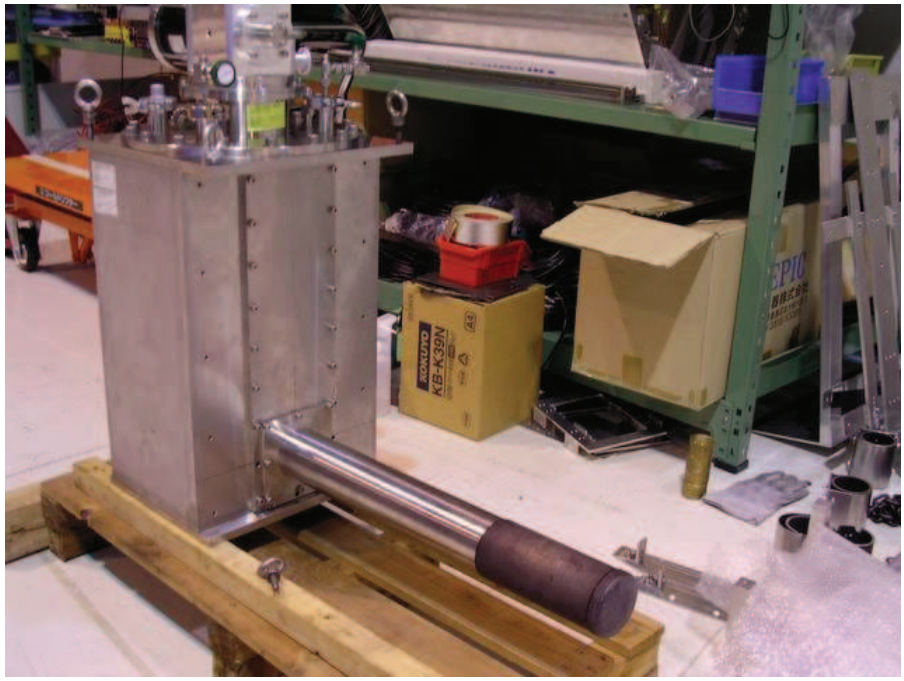

Figure 2.27: Picture of the target system.

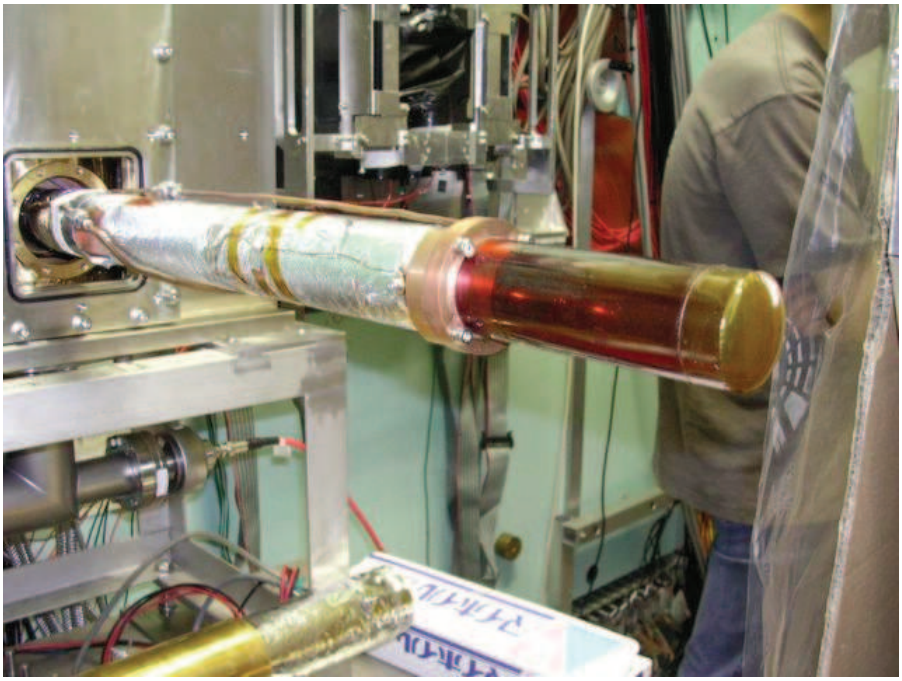

Figure 2.28: Picture of the target cell.

2.6 Time Projection Chamber

A time projection chamber (TPC) was used to detect charged particles nearby the liquid hydrongen target. Figure 2.29 shows an schematic view of the TPC.

The TPC has a shape of a hexagonal cylinder. The length is 910 mm and the circumradius of the hexagon is 280 mm. The TPC has also a hexiagonal bore with a circumradius of 60 mm. The liquid hydrogen target was inserted into this bore.

The active volume of the TPC has a length of 760 mm and were filled with an argon-methane (90 % : 10 %) gas mixture (P10 gas) at atmospheric pressure. A charged particles emitted from the target ionizes electrons and ions from argon atoms in the active volume.

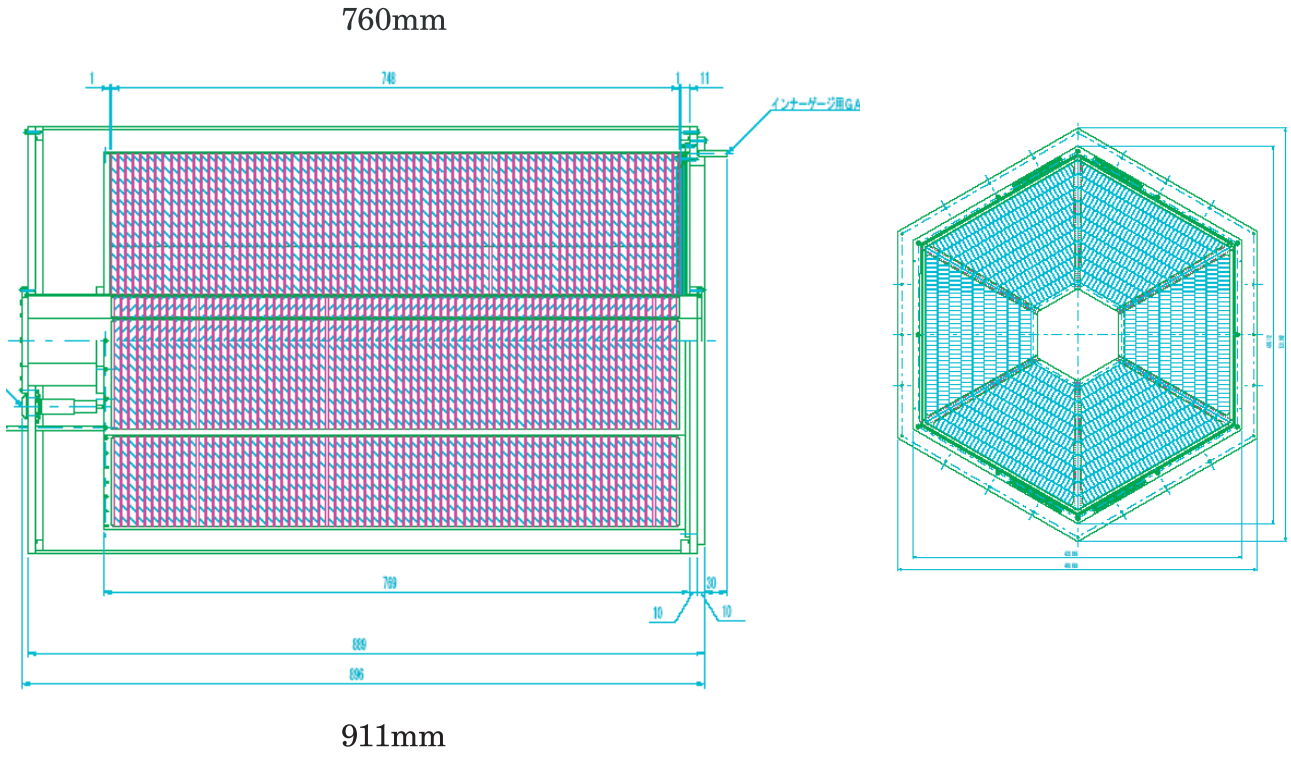

Figure 2.29: A schematic view of the Time Projection Chamber.

2.6.1 High voltage membrane and field cages

The ionized electrons in the active volume of the TPC drift towards the readout plane at the upstream end in an axial magnetic field of 2.0 T generated by a solenoid magnet and an electrical field of 160 V/cm which is parallel to the magnetic field. The electric field is formed by the high voltage membrane installed at the downstream end of the active volume and field strips evapolated on the field cages. The TPC has inner and outer cages and field strips are

evapolated on the both sides of each field cage. Figure 2.31 and 2.32 show the outer and inner field cage, respectively.

The high voltage membrane and the field cages is made of a copper-coated kapton and the frame of the field cages is made of G10. The electrodes are connected to a resister chain mounted on the outside of each cages. The field cage was operated with voltage of 12.1 kV and an electric field of 160 V/cm was generated.

The strength of the electric field was determined by a simulation of electric field in the TPC using GARFIELD[29]. The maximum drift velocity of ionized electrons (52 mm/μs) can be achieved in P10 gas with electric field of 160 V/cm.

2.6.2 Gas amplification part

The gas amplification part of the TPC consists of a gate wire plane, a shield wire plane, a sense wire plane and a cathode pad plane.

In order to protect the gas amplification part against discharge, the gate wire plane prevents drift electrons from reaching the sense wire plane until a trigger signal is created. However, we did not operate the gate wire plane because the gas amplification part survived the beam intensity without operation of the gate wire plane.

The shield wires were set to be -60 V to form the uniform electric field of 160 V/cm between the high voltage membrane and the shield wire plane to form the electric field in the amplification region.

The sense and potential wires are streched alternately with 5 mm spacing in the sense wire plane, and they are parallel to pad layers. The sense wires and the potential wires were set to be +1.57 kV and +200V, respectively, to form the amplification field around the sense wires.

Characteristics of the wire planes are summarized in Table 2.3.

Table 2.3: Characteristics of the wire planes of TPC.

	sense	potential	shield	gate
material	Au-W	Au-BeCu	Au-BeCu	Au-BeCu
diameter (μm)	20	80	50	50
wire spacing (mm)	5	5	2.5	2.5
distance from pad plane (mm)	4	4	8	13
the number of wires	54	30	59	58

An electron avalanche created at a sense wire induces signals on the cathode pads. The induced signals are read through cathode pads. The cathode pad plane of the TPC is devided into 6 sectors. Each sector has 9 pad layers. The innermost layers have 13 pads and the outermost layers have 37 pads. The number of pads included in a layer is incremented by 3 towards outside. The size of a cathode pad is 14.5 mm long and 5.1 mm wide. The gap between neighbouring pads is 0.5 mm. Each sector has 225 pads. Totaly, 1350 cathode pads are read out. The sense wires are stretched over 3 sectors, bending at a boundary of neighbouring sectors. The potential, shield and gate wires are stretched over 6 sectors. The schematic view of cathode pad plane is shown in Figure 2.29.

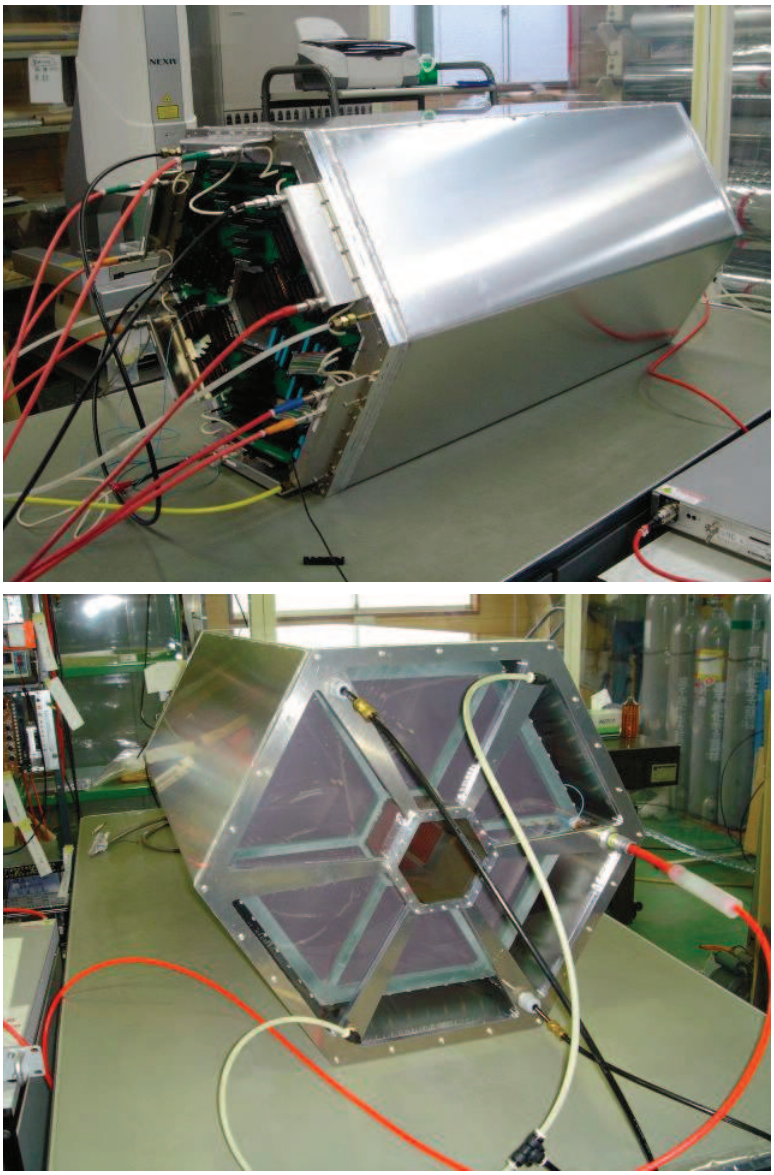

Figure 2.30: The overall views of the Time Projection Chamber. The top and down pictures show upstream and downstream side of the TPC, respectively.

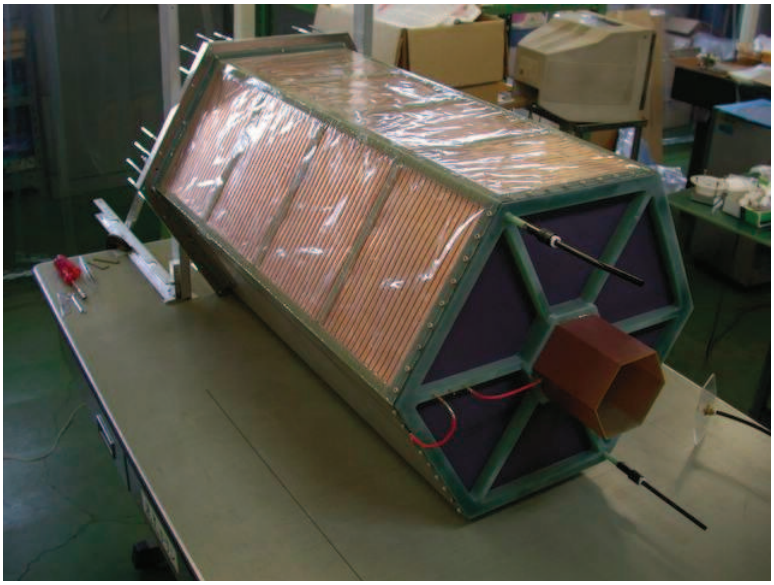

Figure 2.31: Picture of the outer field cage.

Figure 2.32: Picture of the inner field cage.

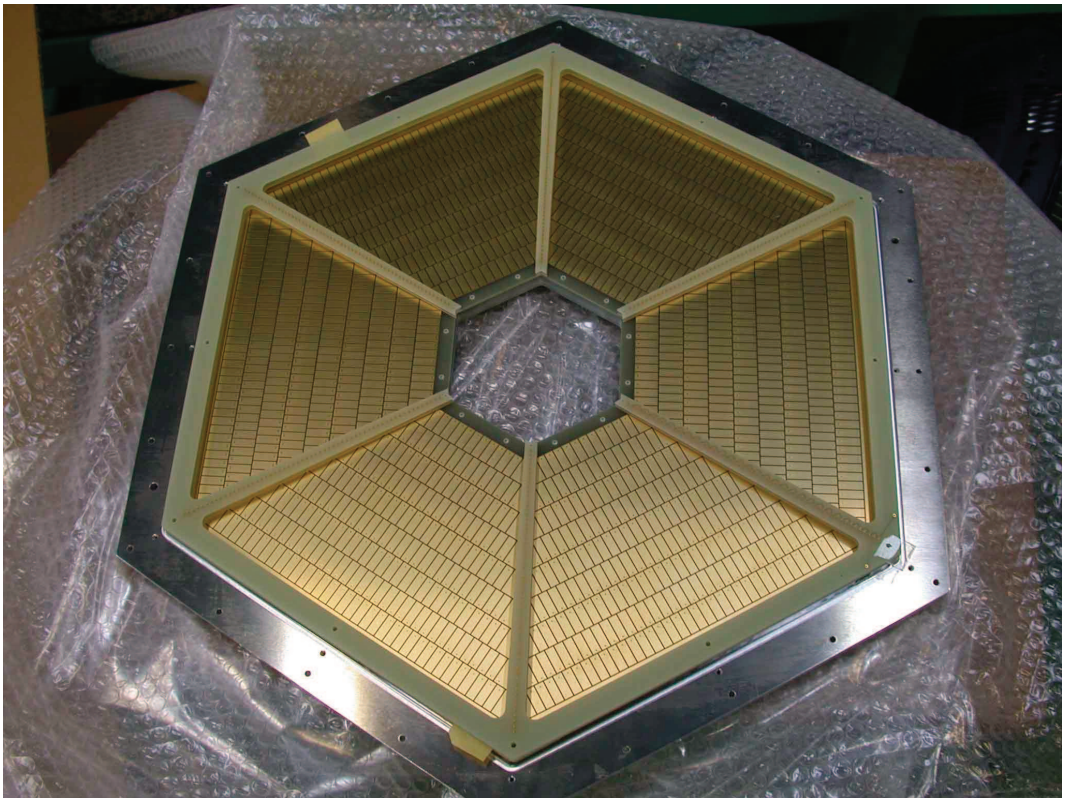

Figure 2.33: Picture of the pad plane of the TPC.

Figure 2.34 shows a sample of event detected by the TPC. The cathode pads are shown in yellow. The pads which have induced signals are shown in red, blue and green and each color correnponds to the pulse height. Five tracks can be seen in the cathode pad plane and these are the projection of the charged tracks in the active volume. Using informations of the drift time, hit coordinates in the drift direction are calculated and three dimensional tracks are reconstructed.

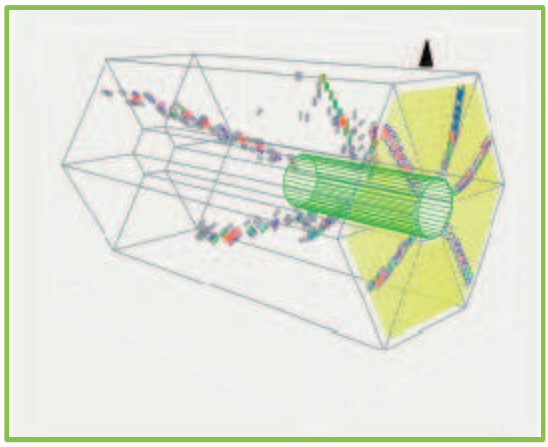

Figure 2.34: A sample of event detected by the TPC. Five tracks can be seen.

2.7 Electronics and Triggers

Electronics and circuits used for the detectors, and the trigger logic are described in this section. LeCroy 4300B FERA (Fast Encoding & Readout ADC) modules are used in

Table 2.4: Readout modules (digitizers) for detectors

Detector	ADC	TDC	used as trigger
TAG-PL	FERA	FASTBUS 1875A/1877S	TAG
TAG-SF	-	FASTBUS 1877S	TAG
UPveto	FERA	FASTBUS 1875A	UPveto
DC's	-	FASTBUS 1877S	-
TOF	FERA	FASTBUS 1875A	-
TPC inner	FERA	FASTBUS 1875A	Sector
TPC outer	FERA	FASTBUS 1875A	Sector
RF	-	FASTBUS 1875A/1877S	-

the CAMAC system to read analog signals from the hodoscopes in the tagging system, the upstream-veto counter, the TPC inner, the TPC outer and the TOF counters. LeCroy FASTBUS 1877S TDC modules are used in the FASTBUS system to read the discriminated signals from the TAG-SFF and TAG-PL and the drift timing from the drift chambers. The FASTBUS 1877S TDC module provides the time resolution of 0.5 nsec/channel and the 1 μsec dynamic range. LeCroy FASTBUS 1875A TDC modules are used in the FASTBUS system to read the discriminated signals from the TAG-PL, upstream-veto counter, the TPC inner the TPC outer and the TOF counters, and RF signals. The FASTBUS 1875A TDC module provides the timing resolution of 0.025 nsec/channel with the 100 nsec dynamic range. The modules used for a signal readout are summarized in Table 2.4.

Signals from the TPC were amplified by charge-sensitive preamplifiers and shaping amplifiers. The shaping amplifier is the CR-(RC)4 type band-pass filter. The waveform of signals was digitized by the flash analogto-digital converter (FADC) module of 10 bit resolution and 40 MHz sampling rate. The FADC modules which were used in the previous LEPS TPC experiment (9U-VME) were used in this experiment. However, the new TPC has more read out channels than the previous TPC. Then, new FADC modules (6U-VME) which has the same specification as the existing FADC were added. The data are read through the VME bus-line. The baseline and the RMS noise were measured every five hours using data taken by the clock trigger. In order to reduce the data size, the zero-suppression for the data at the threshold of 3 of RMS noise was applied on FADC board. In addition, the noise which has the width of less than 4 time bins (100 nsec) were rejected before storing into the FIFO memory on the FADC module to reduce the data size.

Figure 2.35, 2.36 show readout diagrams for the TAG, the upstream-veto counter, TOF counters, and the TPC inner and outer counters, respectively.

TAG In the tagging system, OR signals from the TAG-PL and OR signals of TAG-SF are made. Then the AND signal of them are used in the trigger logic.

Upveto A logic signal from the upstream-veto counter is used as a veto signal.

TOF In the TOF system, a mean timing of the logic signals from the two PMT's of a TOF counter is made by a mean timer module (CAMAC C561). The signal from the mean timer module is read by the majority logic unit module 4532 (CAMAC). Usually, the signal of the multiplicity ≥ 1 is used in the trigger logic in LEPS experiments. In this experiment, TOF system was not used for trigger. The signal informations from TOF counters were recorded and analyzed.

TPC inner and outer TPC inner counters were read out by one PMT, and the logic signals were used for the trigger. TPC outer counters were read out by two PMT's and the mean timing of the signals were used as the logic signal from outer counters. The coincedence signal of inner and outer counter was used for trigger as described in the next item.

'Sector' trigger The 'Sector' trigger is the conincidence signal between an inner counter and one of six outer counters facing that inner counter. For example, Figure 2.38 shows 'Sector 1'. When inner couter 1 and at least one of outer counter 1-6 have coinsidense signals, 'Sector 1' trigger is generated. The 'SectorOR' trigger is generated if at least one 'Sector' trigger is generated. The 'SectorOR' can be written as

$$SectorOR = Sector1 \oplus Sector2 \oplus Sector3 \oplus Sector4 \oplus Sector5 \oplus Sector6 \quad (2.12)$$

where "$\oplus$" represents the OR logic.

The hardware trigger signal for data taking was formed from the logic signals from the TAG, the UPveto, the 'SectorOR' trigger. The UPveto signal is used as veto signal. Figure 2.37 shows a diagram of the trigger logic. The trigger logic can be written as

$$TAG \otimes \overline{UPveto} \otimes SectorOR \tag{2.13}$$

where "$\otimes$" represents the AND logic.

The trigger timing is determined by the timing of the fastest signal from the one of the inner scintillation counters and make the ADC gate signal, and TDC common start and stop signals.

2.8 Data summary

The experiment was performed from 29th January in 2008 to 1st August in 2008. The data was taken with liquid hydrogen (LH_2) target and lineally polarized photon beam. The experiment started with Sabre laser system (λ= 355 nm) which produced the photon beam with the maximum energy of 3 GeV. As already mentioned, Sabre laser system was broken on 9th July 2008, and it was replaced with Paladin laser system (λ= 355 nm) which produced the photon beam with the maximum energy of 2.4 GeV.

The total numbers of photons are 9.5×10^{11} and 1.5×10^{12} for Sabre and Paladin, respectively. Althogh the running period for Paladin is shorter than that for Sabre, the total number of photons for Paladin is higher than that for Sabre because the beam intensity for Paladin is much higher than that for Sabre.

The integrated luminosities are 2.6×10^{-1} pb^{-1} and 3.4×10^{-1} pb^{-1} for Sabre and Paladin, respectively. In the previous LEPS TPC experiment, the integrated luminosity for proton target is 1.7×10^{-1} pb^{-1}, and the photon energy range is $1.5 < E_\gamma < 2.4$ GeV. In this experiment, the integrated luminosity at the same E_γ range as the previous LEPS TPC experiment is 5.0×10^{-1} pb^{-1} and this is about three times larger than that of the previous LEPS TPC experiment. In the photon energy range of $2.4 < E_\gamma < 3.0$ GeV, the integrated luminosity is 1.0×10^{-1} pb^{-1}.

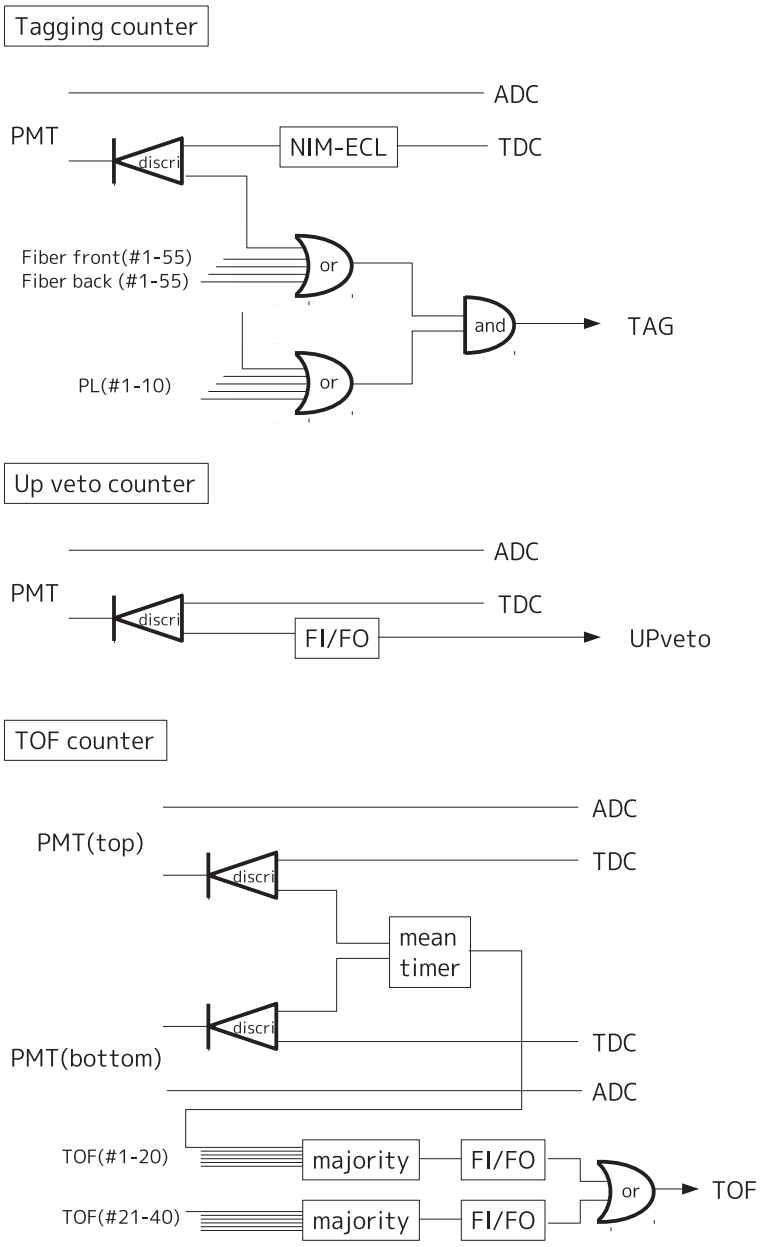

Figure 2.35: Diagram of the readout circuits for TAG, UPveto and TOF.

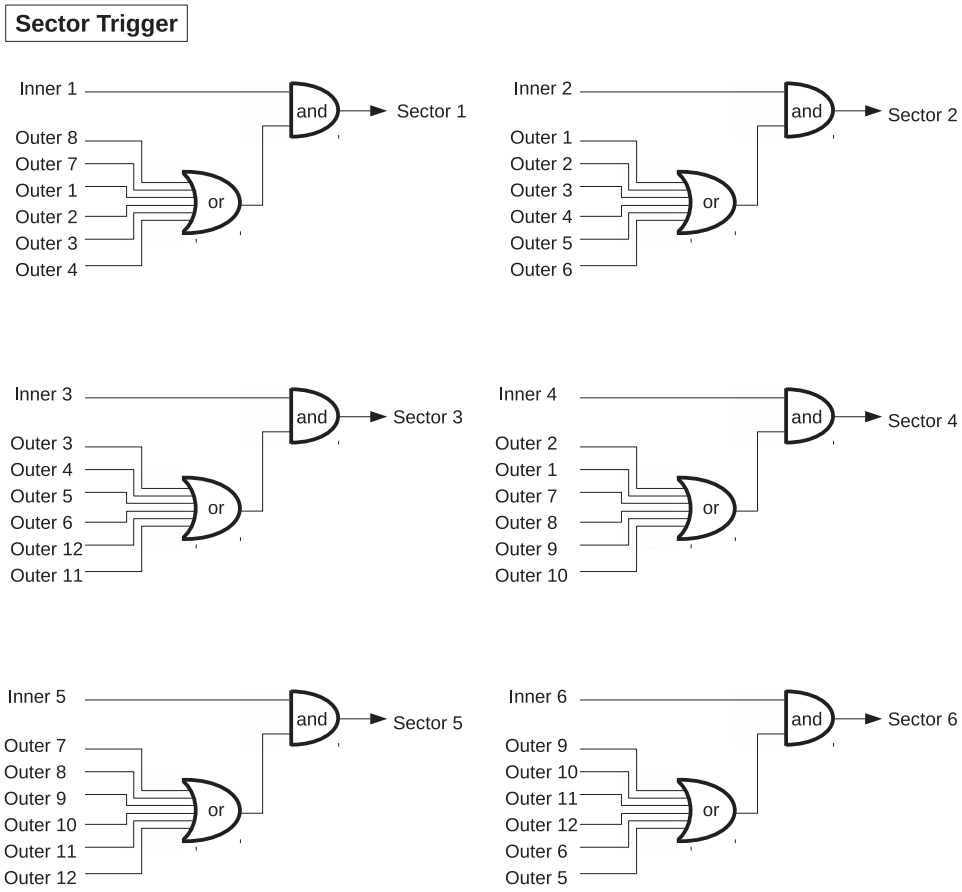

Figure 2.36: Diagram of the readout circuits for TPC inner and outer counters and Sector trigger logic.

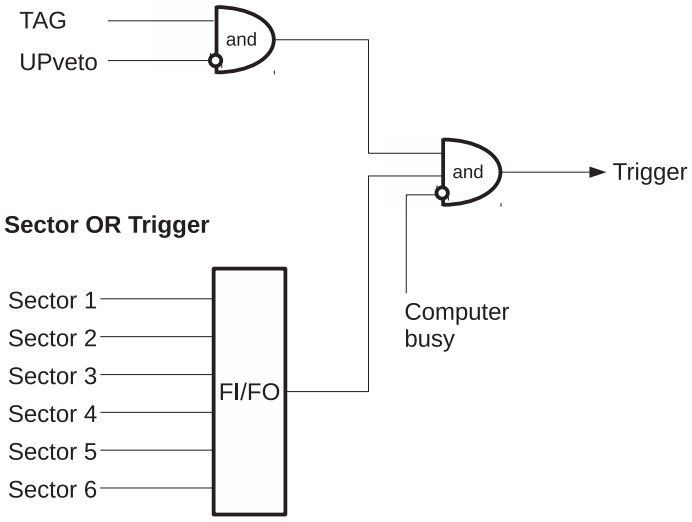

Figure 2.37: Diagram of the trigger logic for data taking.

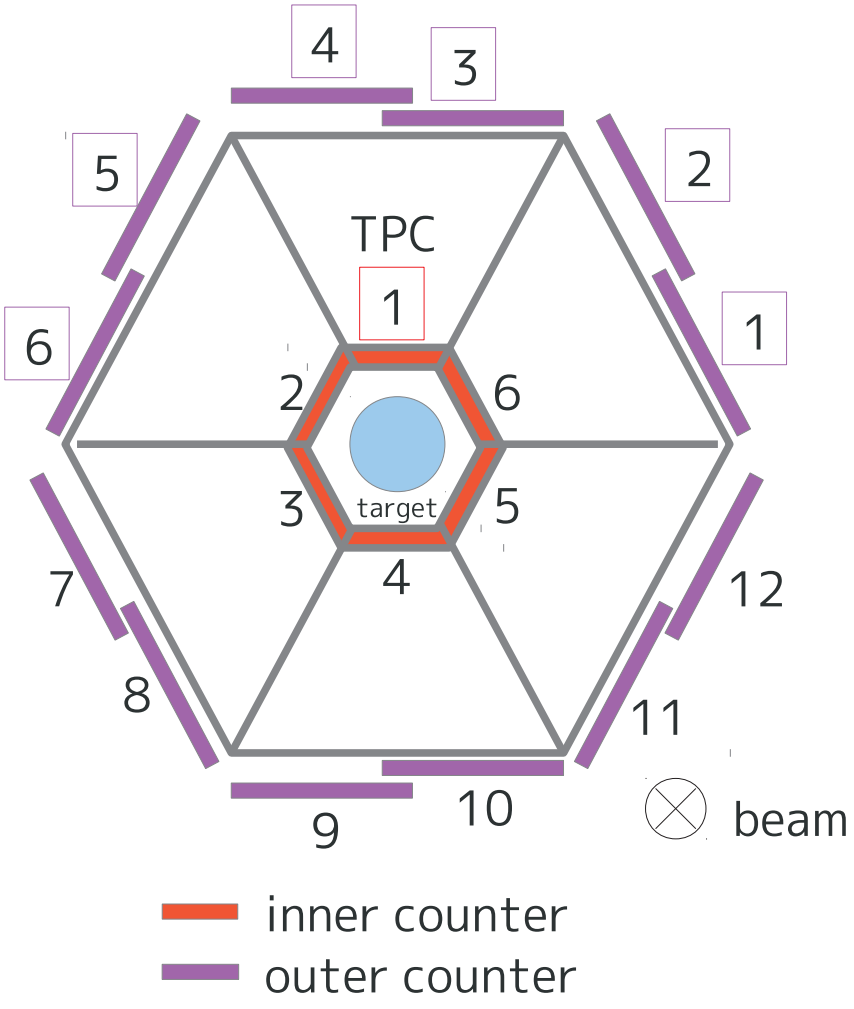

Figure 2.38: Logic of the 'Sector1' trigger. When inner couter 1 and at least one of outer counter 1-6 have coinsidense signals, 'Sector 1' trigger is generated.

Chapter 3

Data analysis

3.1 Event selection by the LEPS spectrometer

In this work, events in which a K^+ was identified by the LEPS spectrometer were analyzed and the spectra of hyperons were obtained from the missing mass distribution of the $\gamma p \rightarrow K^+ X$ reaction ($MM(K^+)$). The following cuts were applied for K^+ selection by LEPS spectrometer: (a) reconstructed mass selection, (b) rejection of decay-in-flight of K^+, (c) vertex seletion at the target.

3.1.1 Particle identification by the LEPS spectrometer

The momentum of a charged particle in the LEPS spectrometer was measured by reconstructing the trajectory using hit coordinates of the drift chambers. The flight length of the trajectory between target and TOF wall can be also obtained. The time of flight from the target to the TOF wall was measured by the TOF counters. Then we can calculate the velocity of a particle. The mass of a charged particle was reconstructed using measured momentum and velocity. Figure 3.1 shows the scatter plot of the momentum and reconstructed mass of particles. The mass resolution depends on the momentum and is expressd by the following function:

$$\sigma^2_{M^2} = 4M^4 \left(1 + \left(\frac{M}{p}\right)^2\right) a_1^2 + 4M^4 p^2 a_2^2 + 4p^2(p^2 + M^2) \left(\frac{c}{L} a_3\right)^2, \tag{3.1}$$

where a_1, a_2 and a_3 are paremeters, M is the nominal value (the PDG value) of the pion, kaon, and proton mass, and c is the speed of light. The pass length L is set to the typical value (4100 mm). The first, second and third terms correspond to the effect of the multiple scattering, the spatial resolution of the drift chambers, and the resolution of the time of flight, respectively. The parameters a_1, a_2 and a_3 were determined as a_1=0.008708, a_2=0.004216, a_3=0.129 by fitting the real data with function 3.1.

As a criteria of K^+ selection, 4 σ cut was applied. In additon, the boundary between pions and kaons is set to 0.15 GeV^2 because higher momentum pions and kaons can not be separated.

The boundary of the K^+ selection is shown in Figure 3.1.

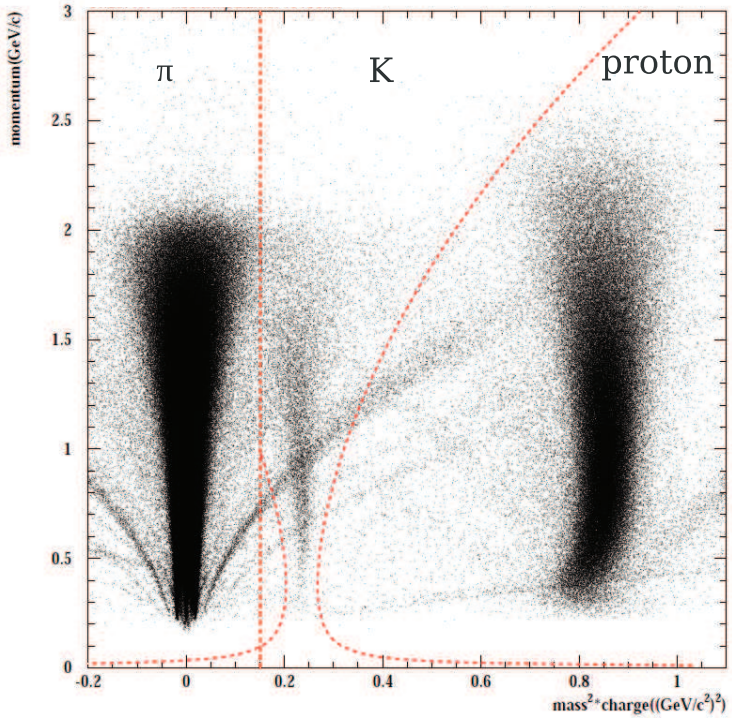

Figure 3.1: Scatter plot of the momentum and reconstructed mass of particles at forward spectometer. Dashed lines show K^+ selection boundary.

3.1.2 Rejection of decay-in-flight of K^+

In order to take into account the effect of multiple scattering of a particle in the LEPS spectrometer and the decay-in-flight of a pion or a kaon, the Kalman filter method was applied in the track reconstruction routine. After the track reconstruction, the χ^2 probability of track fitting was checked. If the χ^2 probability was less than 0.02, the hit in the drift chambers which has the largest χ^2 was removed from the track as an outlier and track fitting was applied again. This procedure was continued until the χ^2 probability became greater than 0.02 or 7 outliers were found. Figure 3.2 shows the distribution of the χ^2 probability of track fitting ($prob(\chi^2)$). The cut condition of $prob(\chi^2) > 0.02$ was required to reject decay-in-flight of K^+'s.

3.1.3 Reaction vertex cut

The closest point between a K^+ track and the beam axis (z-axis) was used for reaction vertex cut. Figure 3.3 shows the distribution of z coordinate of the closest point between a K^+ track and the beam axis. A peak corresponding to the liquid hydrogen target can be seen around z=-1700. The reaction vertex cut of -1935 mm $<$ vtz $<$ -1465 mm was applied. Cut boundaries are shown in figure 3.3.

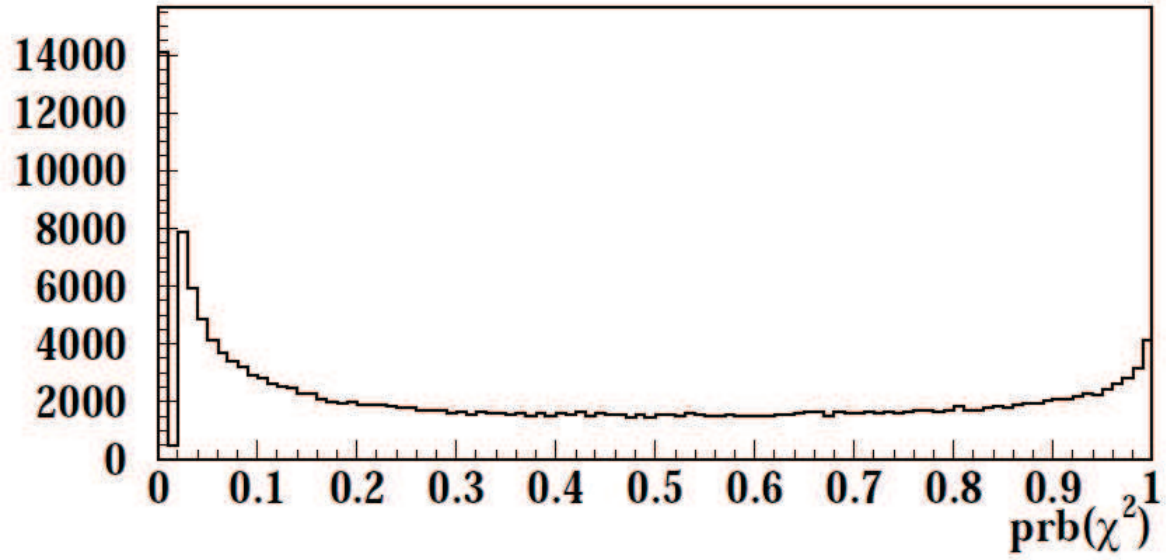

Figure 3.2: The distribution of the χ^2 probability of track fitting by LEPS spectrometer.

3.1.4 The missing mass spectrum of $\gamma p \rightarrow K^+X$ reaction

In this analysis, the spectra of hyperons were obtained from the missing mass distribution of $\gamma p \rightarrow\rightarrow K^+X$ reaction, $MM(K^+)$. Figure 3.4 shows the distribution of $MM(K^+)$. The peaks of $\Lambda(1116)$, $\Sigma^0(1192)$ and $\Lambda(1520)$ can be seen clearly. The bump around 1.4 GeV/c^2 corresponds to $\Sigma^0(1385)$ and $\Lambda(1405)$.

3.2 Track reconstrunction in the TPC

The reconstruction of tracks in the TPC was performed using three dimensional hit coordinates determined by signals from cathode pads. The signals from track hits were searched in the wave form of Flash ADC data and the pulse heights and drift time at the peak of pulse were obtained. Next, the cathode pad signals which were induced by the same avalanche were combined as a cluster in each layer. If the signals on the neighboring pads have over lap region in the drift time, these signals are combined as a cluster. The hit coordinates in the pad plane were obtained from the center of gravity of the charge induced on the cathode pads and anode wires. The number of pads included in a cluster is typically three. The hit coordinate in the direction of the pad raw was determined by taking the center of gravity of charges induced on these three pads assuming a Gaussian charge distribution on the cathode plane. The hit coordinate in the direction normal to the pad raw was determined by taking the center of gravity of hit signal of five anode wires closest to the cluster.

The hit coordinate in the direction normal to the pad raw, Y', was calculated as follows:

$$Y' = \frac{\sum_{i=1}^{5} w_i P_i y'_i}{\sum_{i=1}^{5} w_i P_i}, \tag{3.2}$$

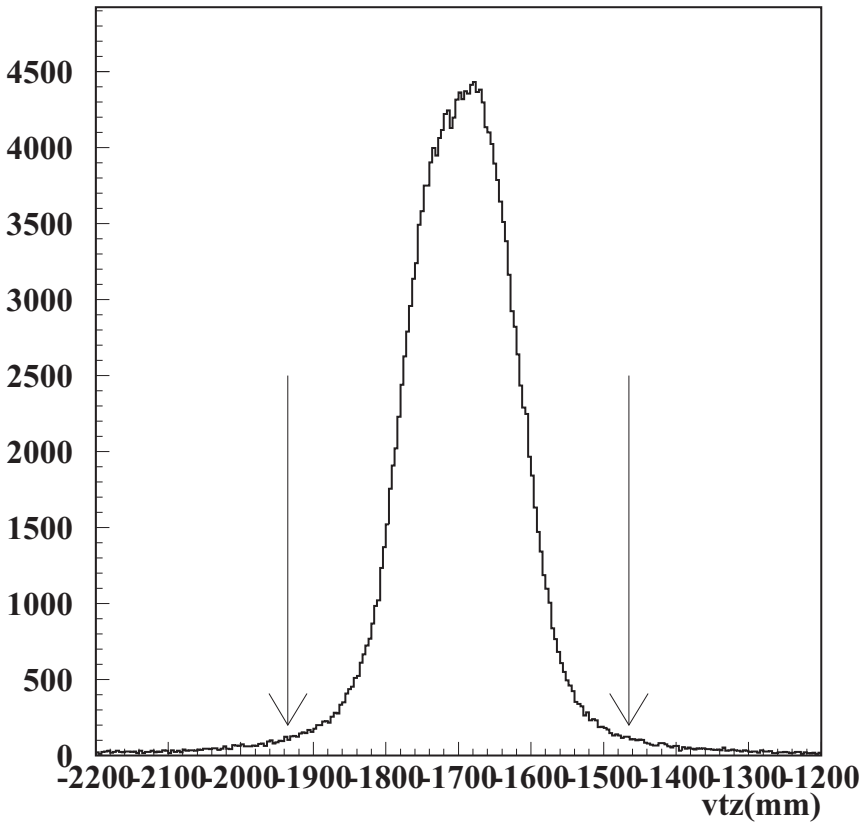

Figure 3.3: The distribution of z coordinate of the closest point between a K^+ track and the beam axis.

where w_i is weight of charge induced on cathode plane by i-th wire, P_i is the pulse height of the signal on the i-th wire, and y'_i is position of the i-th wire in the direction normal to the pad raw. The values of w_i were calculated using the method of mirror charges.

After obtaining the hit coordinates in the direction of the pad raw and the direction normal to the pad raw, hit coordinates were transformed into laboratory frame (X-Y plane).

The z component of hit coordinate was determined using drift time of ionized electrons. The drift time was obtained from the time at the one fifth of the highest signal in the cluster. The coordinate along the drift direction was obtained by reconstructing the drift path of ionized electrons by solving the equation of motion of electrons in the gas with the electric and magnetic field using the drift time.

A track was reconstructed from the coordinates of the clusters on all layers. At first, the clusters on the outermost three layers were selected and a helix was reconstructed from the selected clusters. Secondly, a cluster associating with the helix was searched in the next inner layer and registered to the track candidate. Thirdly, the helix parameters were obtained using all of the clusters registered to the track candidate. The third process were repeated until all layers were serched.

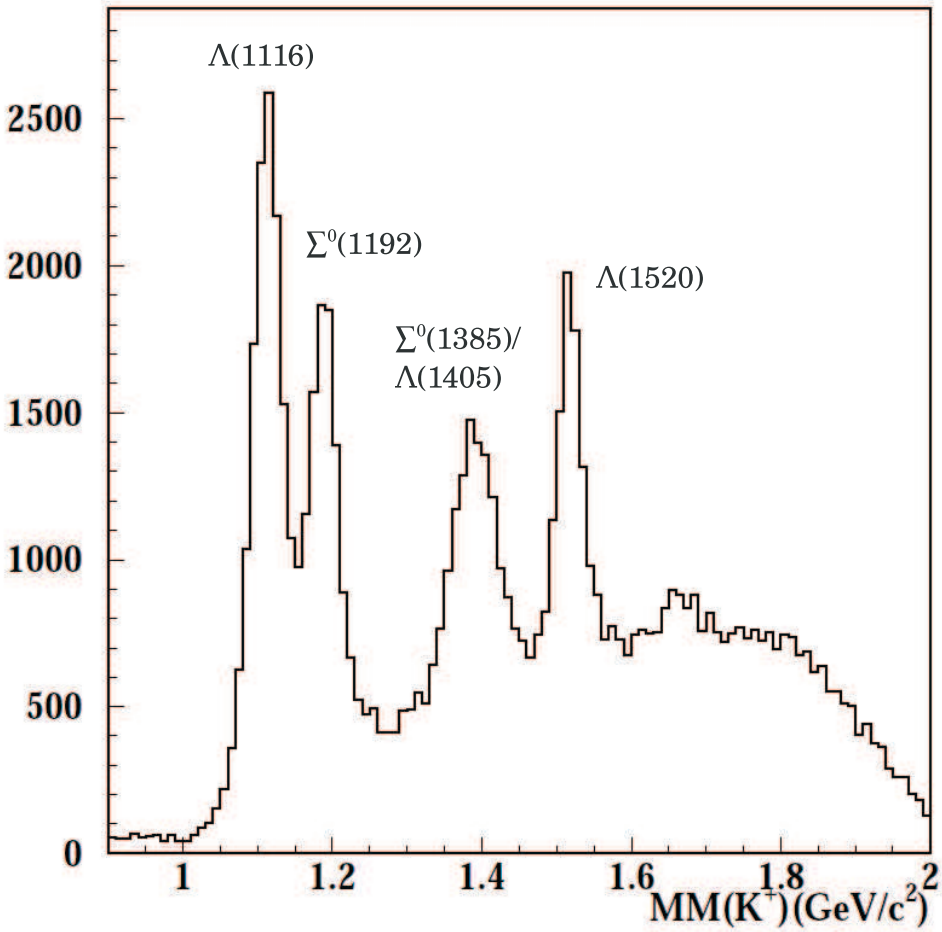

Figure 3.4: The missing mass distribution of $\gamma p \rightarrow K^+ X$ reaction

Runga-Kutta tracking was performed to reconstruct the track momentum, requiring at least four hits in a track candidate.

However the TPC has nine layers in each sector, the outermost and the innermost layers were not used for track reconstruction because the electric field near the field cage of the TPC was distorted and position resolution at these layers were quite bad. Totaly, we used seven layers for each sector for momentum reconstruction.

3.2.1 Particle identification by the TPC

The energy deposition and the momentum of a charged track in the TPC were used for particle identification. The energy deposition measured at a hit point in the TPC was defined as the integration of pulse shape induced on the middle pad of a cluster. In order to obtain dE/dx value, all the energy depositons at each hit included in a track were summed, and normalized by the number of hits. Figure 3.5 (a) and (b) show the most probable value (M.P.V) and σ of dE/dx distribution of π^- tracks as a funciton of momentum, respectively. Figure 3.6 (a) and (b) show the mean value and σ of dE/dx distribution of proton tracks

as a function of momentum, respectively. In Figure 3.5 and 3.6, black circle represents the real data and red circle reprecents the Monte Carlo simulation, respectively. Because $K^+$is identified by forward LEPS spectrometer in this analysis, we do not need to identify $K^+$by the TPC. Following cut conditions, (3.3) and (3.4), were required to identify pions and protons by the TPC,respectively:

$$\frac{dE/dx - M.P.V(\pi)}{\sigma(\pi)} < 8 \; and \; \frac{dE/dx - mean(p)}{\sigma(p)} < -0.5 \tag{3.3}$$

$$\frac{dE/dx - mean(p)}{\sigma(p)} > -3. \tag{3.4}$$

Figure 3.7 shows colleration between the dE/dx and the momentum of charged tracks detected by TPC.

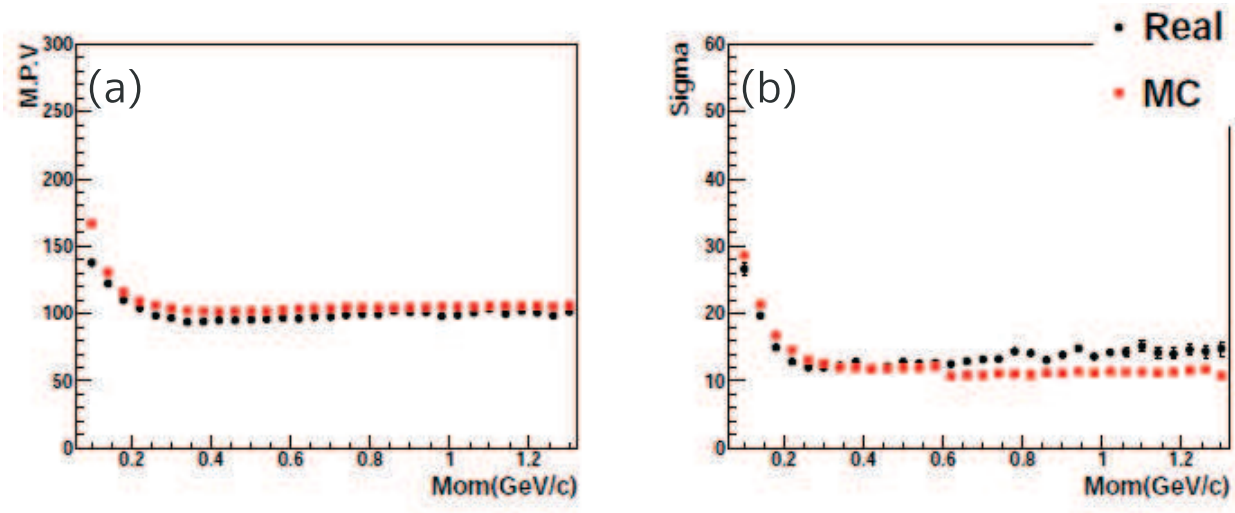

Figure 3.5: (a) The most probable value and (b) σ of dE/dx of π^- tracks as a function of momentum. Black and red circles correspond to the real data and Monte Carlo simulation, respectively.

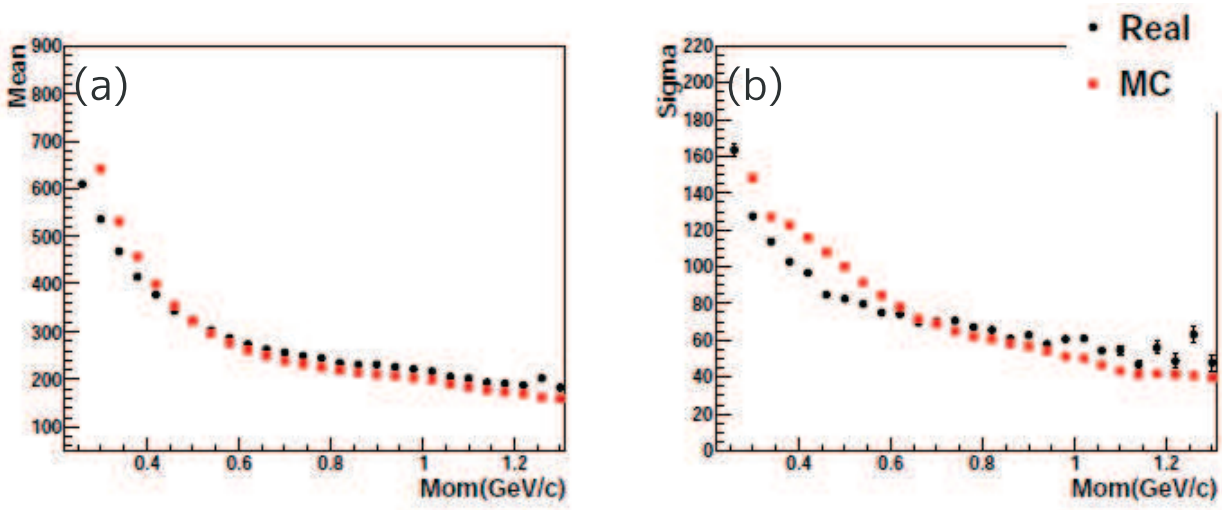

Figure 3.6: (a) The most probable value and (b) σ of dE/dx of π^-tracks as a function of momentum. Black and red circles correspond to the real data and Monte Carlo simulation, respectively.

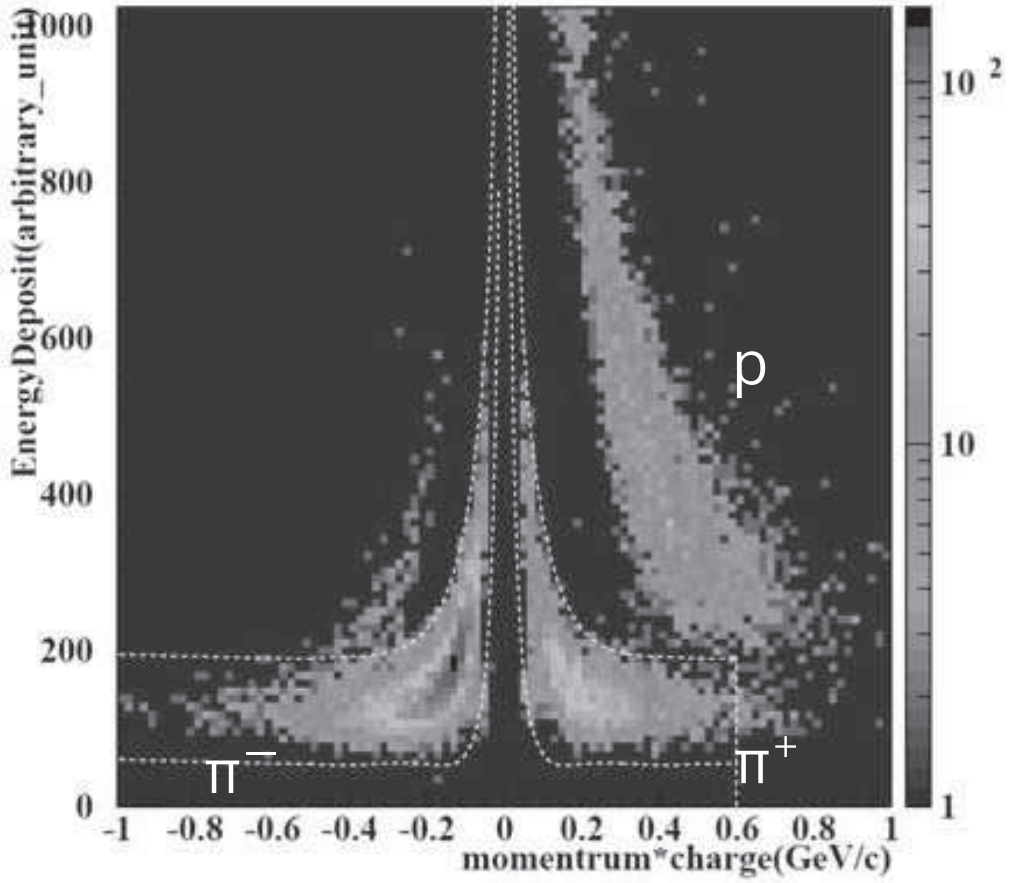

Figure 3.7: Correlation between the momentum and energy deposit in the TPC. The x and y axes represent the momentum × charge and the energy deposit of a track, respectively. The loci of p, π^+ and π^- can be seen clearly. The K^- locus is also seen in the negative charge region. The K^+ can not be seen because a K^+ is identified in the forward spectrometer for events in this plot.

3.3 Analysis for $\Sigma^0(1385)$ photoproduction

In this section, the analysis for $\Sigma^0(1385)$ photoproduction is described. Following reaction was focused for this analysis,

$$\begin{aligned} \gamma p &\rightarrow K^+\Sigma^0(1385) \\ &\rightarrow K^+\Lambda\pi^0 \\ &\rightarrow K^+p\pi^-\pi^0 \end{aligned} \tag{3.5}$$

For this analysis, events in which a K^+ was detected in the LEPS spectrometer and a proton and a π^- in TPC were selected. Λ was identified from the invariant mass of $(p\pi^-)$ pairs, and the π^0 was identified from the missing mass of $\gamma p \rightarrow K^+p\pi^-X$, $MM(K^+p\pi^-)$.

$\Lambda(1405)$ can not decay into $\Lambda\pi^0$ due to isospin conservation. On the other hand, $\Sigma^0(1385)$ has $\Lambda\pi^0$ decay branch of 87%. Therefore, the $\gamma p \rightarrow K^+\Sigma^0(1385)$ reaction events were identified from a peak in the missing mass of the $\gamma p \rightarrow K^+X$ reaction ($MM(K^+)$) for $K^+\Lambda\pi^0$ final state,

The main background reactions were $\Sigma^0\pi^0$ decay of $\Lambda(1405)$ and $\Sigma^+\pi^-$ decay of $\Lambda(1405)$ and $\Sigma^0(1385)$:

$$\begin{aligned} \gamma p &\rightarrow K^+\Lambda(1405) \\ &\rightarrow K^+\Sigma^0\pi^0 \\ &\rightarrow K^+\Lambda\gamma\pi^0 \\ &\rightarrow K^+p\pi^-\gamma\pi^0 \end{aligned} \tag{3.6}$$

and

$$\begin{aligned} \gamma p &\rightarrow K^+\Lambda(1405)/\Sigma^0(1385) \\ &\rightarrow K^+\Sigma^+\pi^- \\ &\rightarrow K^+p\pi^0\pi^-. \end{aligned} \tag{3.7}$$

The contamination of the reaction (3.6) was estimated from the missing mass of the $\gamma p \rightarrow K^+p\pi^-X$ reaction, $MM(K^+p\pi^-)$. X corresponds to π^0 and $\pi^0\gamma$ for $\Sigma^0(1385)$ production and the background of the reaction (3.6), respectively.

The contamination of the reaction (3.7) was estimated from the missing mass of the $\gamma\ p \rightarrow K^+\pi^-X$ reaction, $MM(K^+\pi^-)$, where X corresponds to $p\pi^0$ for the $\Sigma^0(1385)$ production, and X corresponds to Σ^+ for the background reaction (3.7).

The procedure of the analysis is as follows,

1. Selection of a K^+ in the LEPS spectrometer
2. Selection of a $p\pi^-$ pair in the TPC and identification of a Λ from invariant mass of $p\pi^-$ pair
3. Estimation of the contamination from $\gamma p \rightarrow K^+\Lambda(1405) \rightarrow \Sigma^0\pi^0$ reaction

4. Estimation of the contamination from $\gamma p \rightarrow K^+\Lambda(1405) \rightarrow \Sigma^+\pi^-$ reaction

5. Extraction of the yield of $\Sigma^0(1385)$ photoproduction from $MM(K^+)$ for the events in which Λ was identified after subtracting the contamination of the reaction (3.6) and (3.7).

3.3.1 Identification of $\Lambda(1116)$ by TPC

The invariant mass spectra of $p\pi^-$pairs ($M(p\pi^-)$) are shown in Figure 3.8. The peaks corresponding to the mass of Λ is clearly observed.

The $M(p\pi^-)$ distribution was fitted with Gaussian and linear background. The measured peak and width (RMS) were obtained to be 1115.3 $\pm$ 0.2 MeV/c^2 and 8.8 $\pm$ 0.3 MeV/c^2, respectively. The peak value was consistent with PDG value (1115.6 MeV/c^2) and the width was consistent with Monte Carlo simulation (8 MeV/c^2). The solid line in figure 3.8 shows fit results. The boundary of the Λ selection cut was determined as $M(p\pi^-) < 1.13$ GeV/c^2.

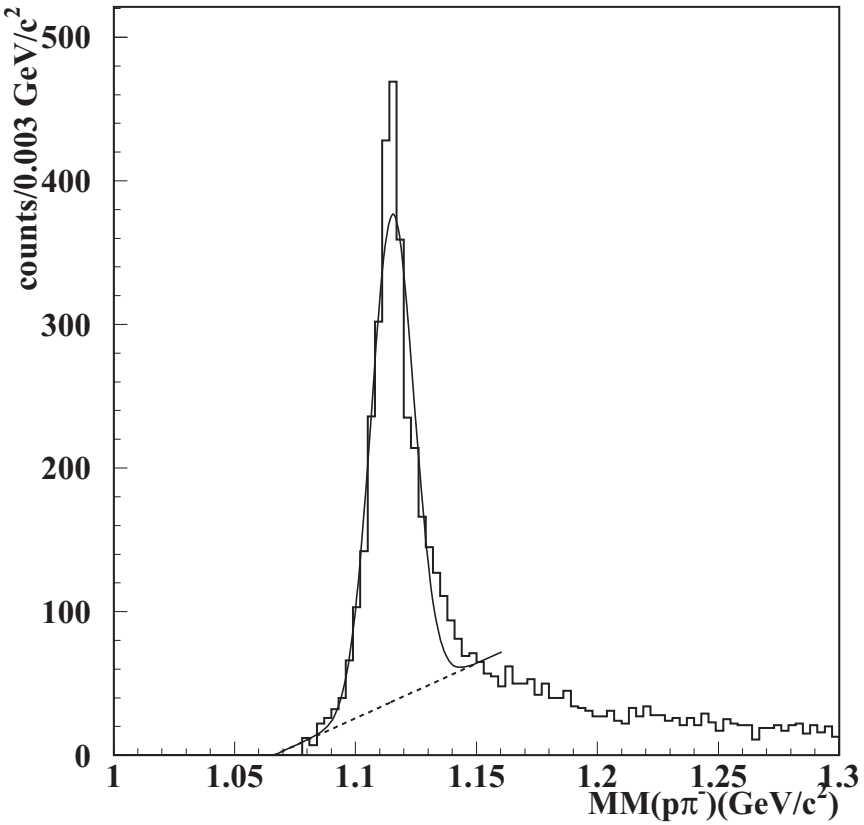

Figure 3.8: Invariant mass spectra of $p\pi^-$ pairs.

3.3.2 $MM(K^+)$ distribution for Λ tagged events

The distribution of $MM(K^+)$ for events which survived the Λ selection cut is shown in Figure 3.9(a). Figure 3.9(b) shows the distribution of $MM(K^+)$ around $\Lambda(1116)$ mass region. The mass peak positions were obtained by fitting two Gaussians to the data, assuming a linear background. The measured masses of $\Lambda(1116)$ and $\Sigma^0(1192)$ were 1115 $\pm$ 0.2 MeV/c^2 and 1190 $\pm$ 0.2 MeV/c^2, respectively. These were consistent with PDG value. The width of $\Lambda(1116)$ and $\Sigma^0(1192)$ were obtained as 19 $\pm$ 0.2 MeV/c^2 and 16 $\pm$ 0.3 MeV/c^2, respectively. These were consistent with the width of Monte Carlo simulation. Figure 3.9(c) shows $MM(K^+)$ distrubution around $\Lambda(1520)$ mass region. The mass of $\Lambda(1520)$ was obtained from a Breit-Wigner fit with a linear background assumption to be 1519 MeV/c^2. The obtained width (FWHM) was 29 MeV/c^2. The peak value and width were consitent width PDG value and Monte Carlo, respectively. The hyperon masses were measured correctly.

3.3.3 Background of $\gamma p \rightarrow K^+\Lambda(1405) \rightarrow K^+\Sigma^0\pi^0$

The contamination of the $\Lambda(1405)$ production (reaction (3.6)),

$$\begin{aligned} \gamma p &\rightarrow K^+\Lambda(1405) \\ &\rightarrow K^+\Sigma^0\pi^0 \\ &\rightarrow K^+\Lambda\gamma\pi^0, \end{aligned}$$

was estimated in three photon energy ranges: $1.5 < E_\gamma < 2.0$ GeV, $2.0 < E_\gamma < 2.4$ GeV, and $2.4 < E_\gamma < 3.0$ GeV. Figure 3.10 shows the squared missing mass of $\gamma p \rightarrow K^+ p\pi^- X$ reaction ($MM^2(K^+p\pi^-)$) after Λ selection cut and the cut of $\Lambda(1405)$ and $\Sigma^0(1385)$ selection, $1.3 < MM(K^+p\pi^-) < 1.45$ GeV/c^2.

The Black histograms in Figure 3.10 show the spectra obtained from data. The peaks in Figure 3.10(a), (b) and (c) correspond to π^0. The $MM^2(K^+p\pi^-)$ spectra of real data were fitted with the expected spectra of $\Sigma^0(1385)$ production and background reaction (3.6) generated by Monte Carlo simulation. The red and blue histogram show the Monte Carlo spectrum for $\Sigma^0(1385)$ production and background reaction (3.6), respectively. The contamination from $\gamma p \rightarrow K^+\Lambda(1405) \rightarrow K^+\Sigma^0\pi^0$ reaction was estimated from the results of fitting.

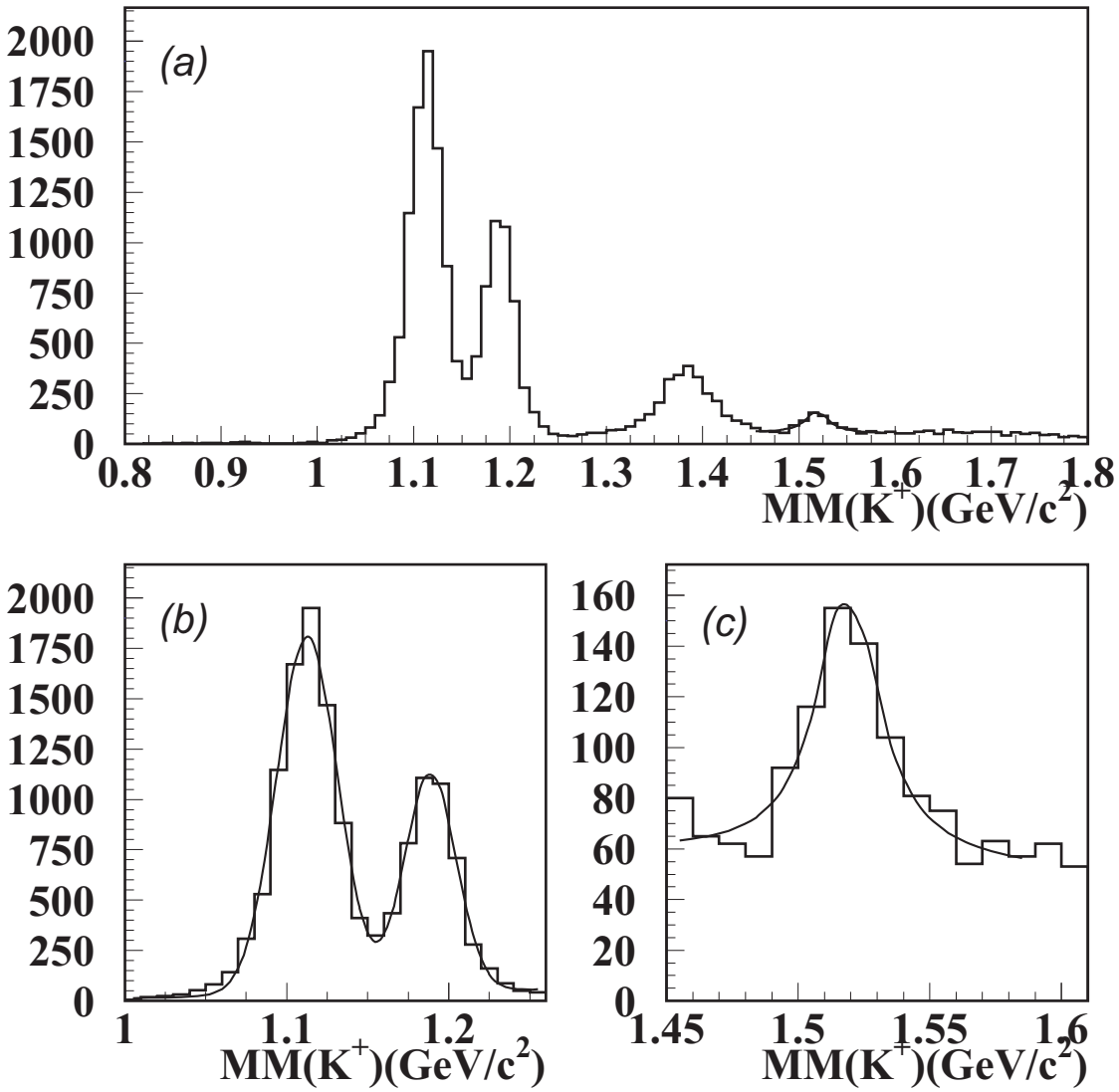

Figure 3.9: Missing mass of the $\gamma p \rightarrow K^+ X$ reaction after the Λ selection cut for all E_γ range: $1.5 < E_\gamma < 3.0$ GeV. (a) whole$MM(K^+)$ range, (b) around Λ and Σ^0 and (c) around $\Lambda(1520)$.

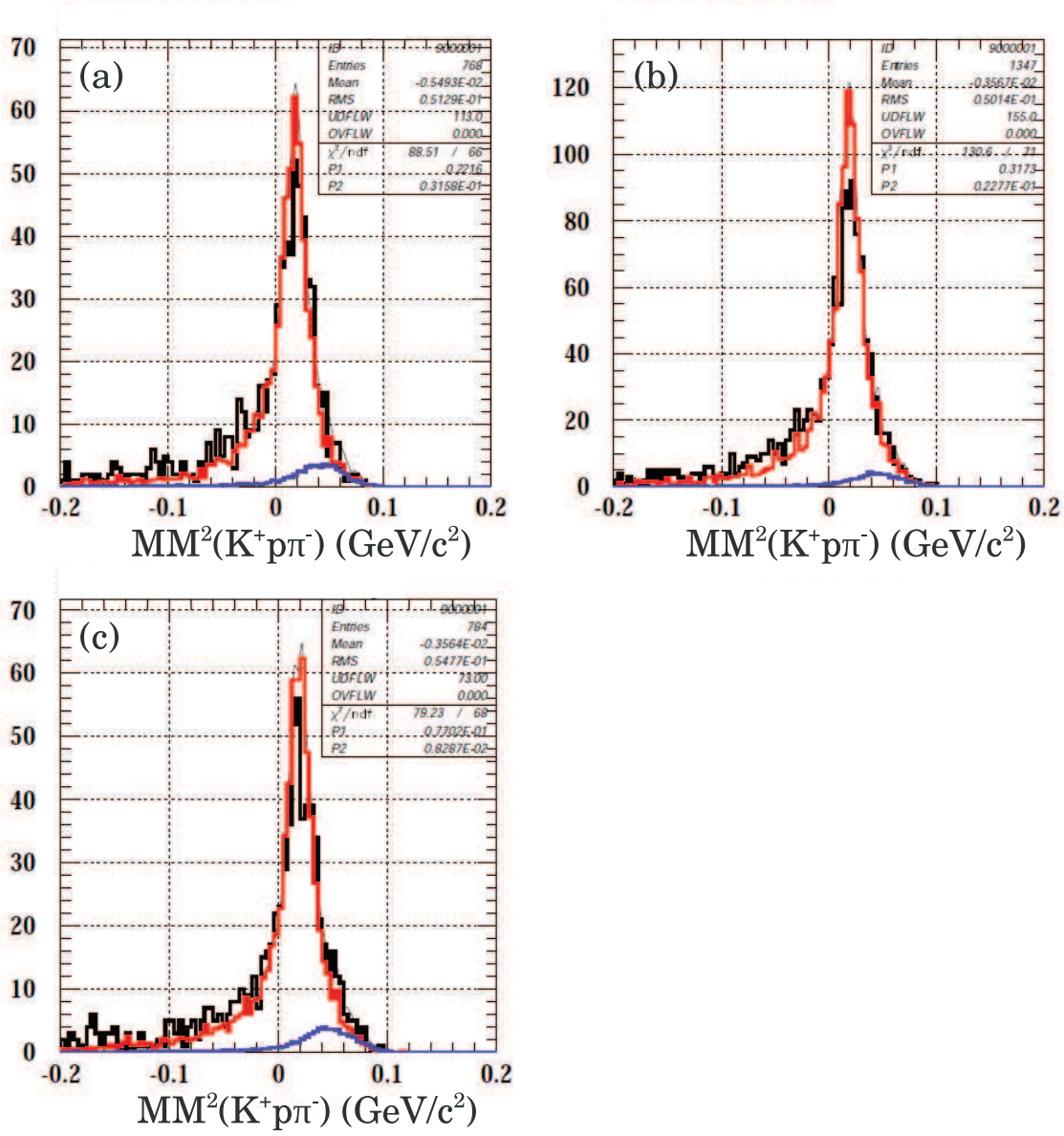

Figure 3.10: Distribution of the $MM^2(K^+p\pi^-)$ after the Λ selection cut and the cut of $1.3 < MM(K^+) < 1.45$ GeV/c^2 in three photon energy ranges: $1.5 < E_\gamma < 2.0$ GeV, $2.0 < E_\gamma < 2.4$ GeV and $2.4 < E_\gamma < 3.0$ GeV. The black histogram shows real data. The red and blue histogram show the shape of Monte Carlo simulation for $\gamma p \rightarrow K^+\Sigma^0(1385) \rightarrow K^+\Lambda\pi^0$ and $\gamma p \rightarrow K^+\Lambda(1405) \rightarrow K^+\Sigma^0\pi^0 \rightarrow K^+\Lambda\gamma\ \pi^0$, respectively.

3.3.4 Background of $\Lambda(1405)/\Sigma^0(1385) \rightarrow \Sigma^+\pi^-$ mode

The contamination from the reaction (3.7), $\gamma\ p \rightarrow K^+\Lambda(1405)/\Sigma^0(1385) \rightarrow K^+\Sigma^+\pi^- \rightarrow K^+p\pi^0\pi^-$, was estimated. Since the particles in the final state are the same as those of $\Sigma^0(1385) \rightarrow \Lambda\pi^0 \rightarrow p\pi^-\pi^0$ mode, these two reactions cannot be separated in $MM(K^+p\pi^-)$ distribution. Moreover, the distribution of $MM(K^+\pi^-)$ for $\Sigma^0(1385) \rightarrow \Lambda\pi^0$ reaction has a peak around 1.2 GeV/c^2 which is close to Σ^+ mass, 1.189 GeV/c^2. Figure 3.11(a) and 3.11(b) show the distributions of $MM(K^+\pi^-)$ for $\gamma\ p \rightarrow K^+\Sigma^0(1385) \rightarrow K^+\Lambda\pi^0 \rightarrow K^+p\pi^-\pi^0$ and $\gamma\ p \rightarrow K^+\Lambda(1405) \rightarrow K^+\Sigma^+\pi^- \rightarrow K^+p\pi^0\pi^-$ reactions generated by the Monte Carlo simulation, respectively. In Figure 3.11(b), a clear peak corresponding to Σ^+ can be seen in the $MM(K^+\pi^-)$ distribution for $\gamma\ p \rightarrow K^+\Lambda(1405) \rightarrow K^+\Sigma^+\pi^-$ reaction. In Figure 3.11(a), the peak position of the $MM(K^+\pi^-)$ distribution for $\gamma\ p \rightarrow K^+\Sigma^0(1385) \rightarrow K^+\Lambda\pi^0 \rightarrow K^+p\pi^-\pi^0$ is around 1.2 GeV/c^2 and close to Σ^+ mass. Therefore, $\gamma\ p \rightarrow K^+\Sigma^0(1385) \rightarrow K^+\Lambda\pi^0 \rightarrow K^+p\pi^-\pi^0$ and $\gamma\ p \rightarrow K^+\Lambda(1405) \rightarrow K^+\Sigma^+\pi^- \rightarrow K^+p\pi^0\pi^-$ reactions can not be separated in the $MM(K^+\pi^-)$ distribution.

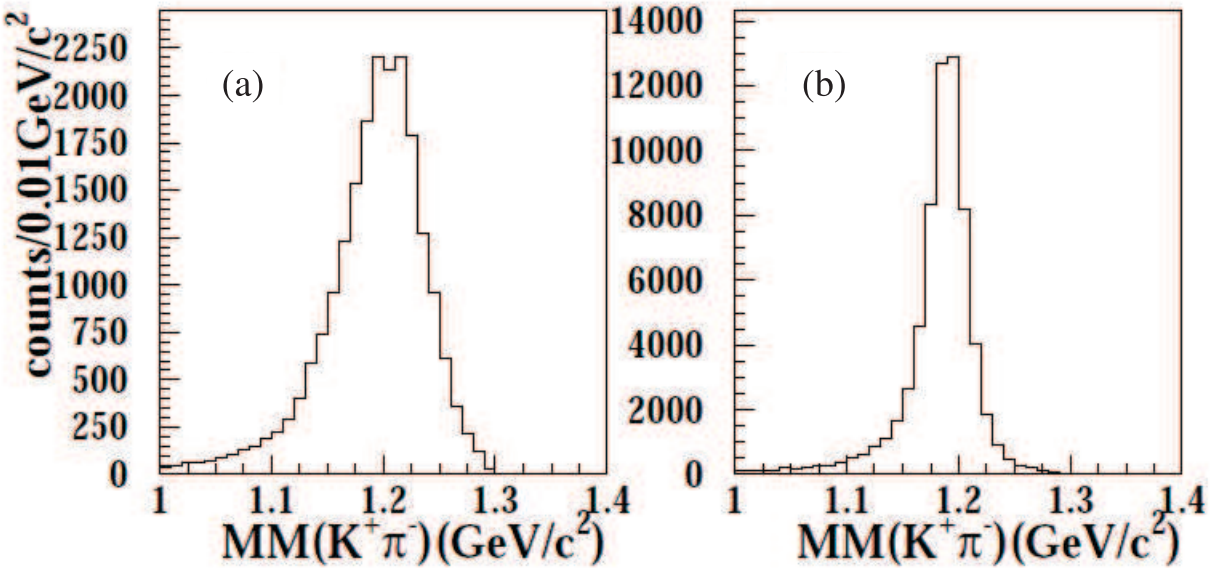

Figure 3.11: Distributions of $MM(K^+\pi^-)$ obtained by the Monte-Carlo simulation of the $\gamma\ p \rightarrow K^+\Sigma^0(1385) \rightarrow K^+\Lambda\pi^0 \rightarrow K^+p\pi^-\pi^0$ and $\gamma\ p \rightarrow K^+\Lambda(1405) \rightarrow K^+\Sigma^+\pi^- \rightarrow K^+p\pi^0\pi^-$ reactions. $MM(K^+\pi^-)$ distributions for $\Sigma^0(1385)$ and $\Lambda(1405)$ are shown in (a) and (b), respectively.

The contamination from the reaction (3.7) was estimated from the distribution of $MM(K^+\pi^-)$ for events which were rejected by the Λ selection cut. Figure 3.12 and 3.13 show the distribution fo $M(p\pi^-)$ for $\Sigma^0(1385) \rightarrow \Lambda\pi^0$ reaction and for $\Lambda(1405) \rightarrow \Sigma^+\pi^-$ reaction which were generated by the Monte Carlo simulation, respectively. The spectrum for $\Sigma^0(1385)$ production has a peak around Λ mass, while the one for $\Lambda(1405)$ production shows a broad distribution. The cut of $M(p\pi^-) > 1.13$ GeV/c^2 was applies to reject $\Lambda\pi^0$ decay of $\Sigma^0(1385)$.

The Black histogram in Figure 3.14 shows the distribuion of $MM(K^+\pi^-)$ which survived Λ rejection cut and the $\Lambda(1405)$ and $\Sigma^0(1385)$ selection cut, $1.30 < MM(K^+) < 1.45$ GeV/c^2.

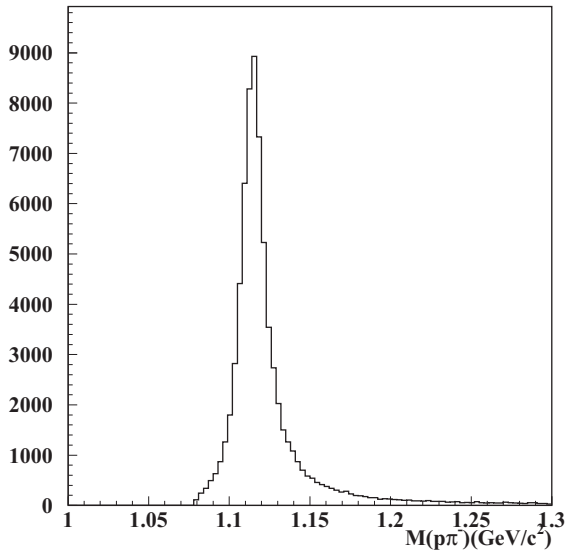

Figure 3.12: Distribution of the invariant mass of $p\pi^-$ pairs ($M(p\pi^-)$) obtained by the Monte-Carlo simulation of $\Sigma^0(1385)$ photoproduction.

The spectrum was fitted with the expected spectrum of $K^+\Lambda(1405)$ production generated by the Monte Carlo simulation and the back ground spectrum due to the particle misidentification by the LEPS spectrometer. The spectrum of $K^+\Lambda(1405)$ production generated by the Monte Carlo simuration is shown by red histogram.

The width of the peak corresponding to the Σ^+ was much wider in the real data than in the Monte Carlo simulation. Unfortunately, the reason of the larger width could not be specified in this analysis. Then, the systematic error of the yield of the reaction (6.1) was determined by estimating the yield of the reaction (6.1) twice, firstly assuming that there were no contribution to the peak from Σ^+ and secondly assuming that all contribution of the peak came from Σ^+.

3.3.5 Yield estimation of $\Sigma^0(1385)$

The black histograms in Figure 3.15 show $MM(K^+)$ distributions after the Λ selection cut at three photon energy regions, (a) $1.5 < E_\gamma < 2.0$ GeV, (b) $2.0 < E_\gamma < 2.4$ GeV and (c) $2.4 < E_\gamma < 3.0$ GeV. The yield in the $\Sigma^0(1385)$ mass region at each E_γ region was obtained by fitting the spectrum of $\Sigma^0(1385)$ together with the non-resonant $K^+\Lambda\pi^0$ production spectrum generated by Monte Carlo simulation. The red and blue histograms show the contribution of $\Sigma^0(1385)$ and non-resonant $K^+\Lambda\pi^0$ production , respectively. The obtained yields include the contaminations of (3.6) and (3.7) reactions. The yields of the $\Sigma^0(1385)$ production were estimated by subtracting the contamintaion of these reactions and corrected using the acceptance of selection cuts.

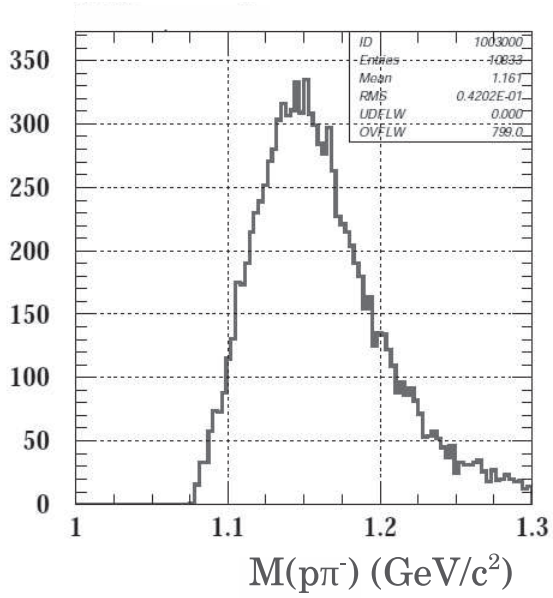

Figure 3.13: Distribution of the invariant mass of $p\pi^-$ pairs ($M(p\pi^-)$) obtained by the Monte-Carlo simulation of $\Lambda(1405)$ photoproduction.

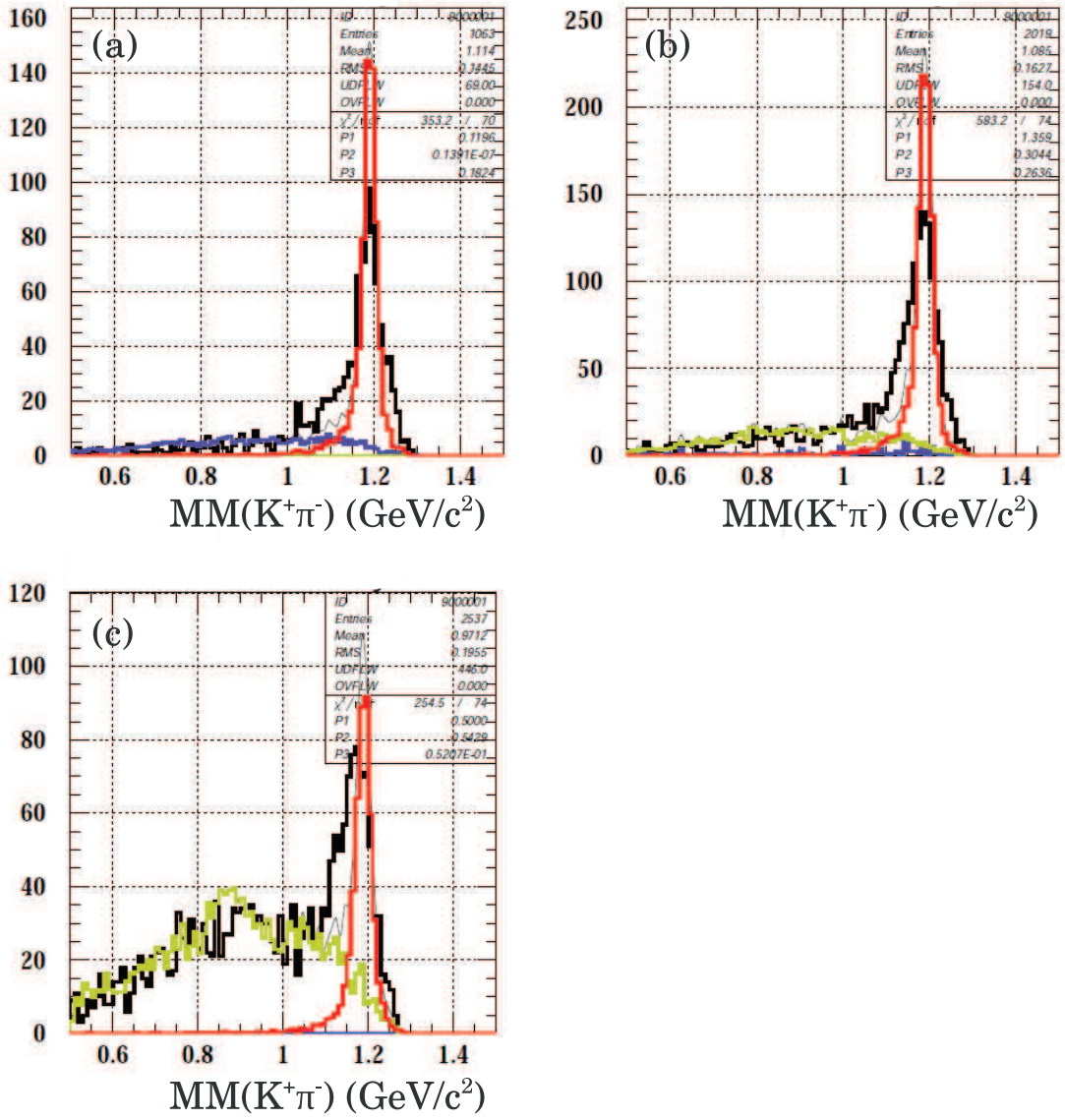

Figure 3.14: Distribution of the $MM(K^+\pi^-)$ after the Λrejection cut and the cut of $1.3 < MM(K^+) < 1.45$ GeV/c^2 in three photon energy ranges: (a) $1.5 < E_\gamma < 2.0$ GeV, (b) $2.0 < E_\gamma < 2.4$ GeV and (c) $2.4 < E_\gamma < 3.0$ GeV.

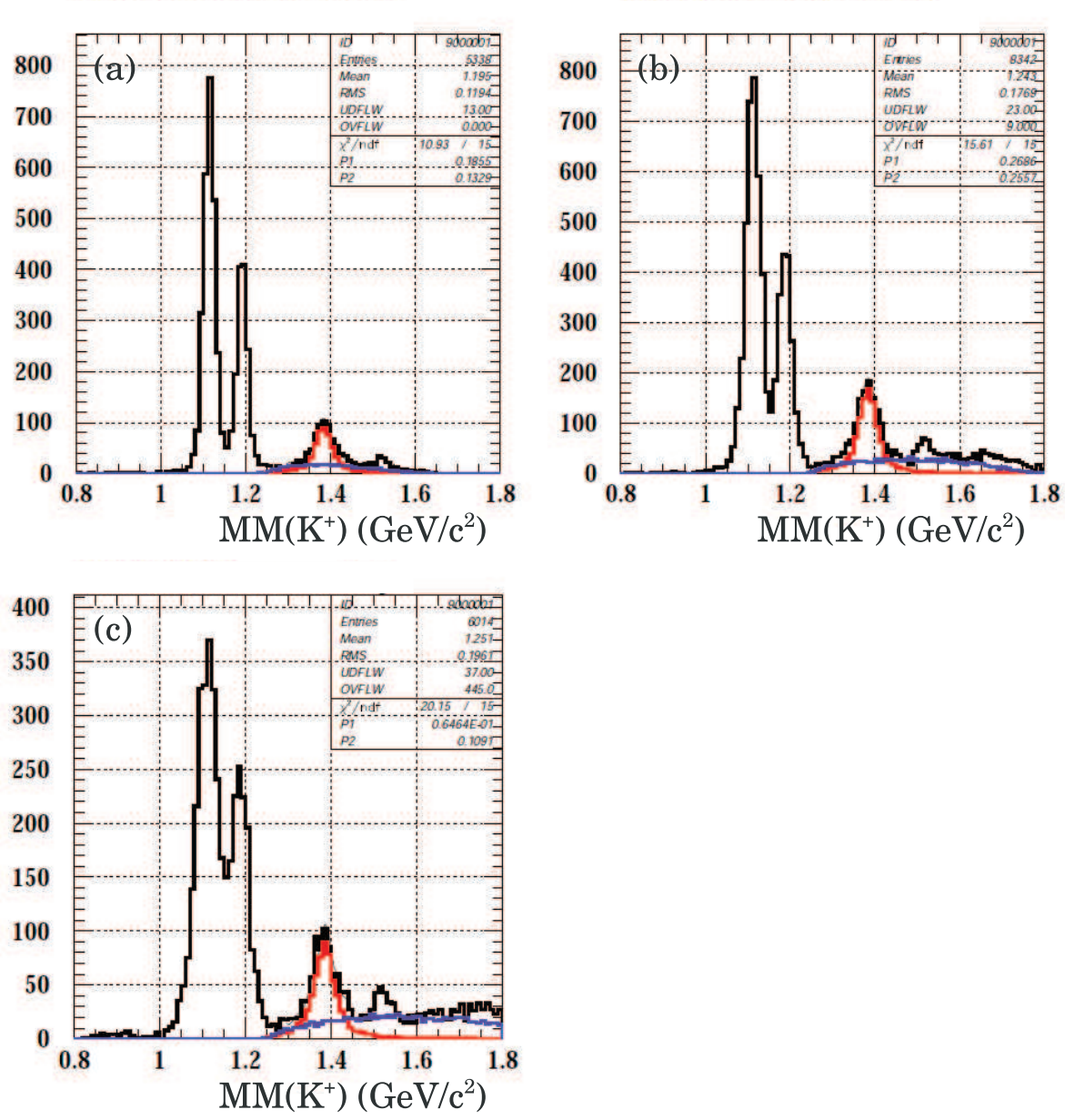

Figure 3.15: Missing mass of the $\gamma p \to K^+ X$ reaction after the Λ selection cut at each E_γ region: (a) $1.5 < E_\gamma < 2.0$ GeV, (b) $2.0 < E_\gamma < 2.4$ GeV, (c) $2.4 < E_\gamma < 3.0$ GeV. Black, red and blue histograms represent the real data, MC of $\Sigma^0(1385)$ and MC of non-resonant $\Lambda\pi^0$.

3.4 Analysis for $\Lambda(1405)$ photoproduction

In this section, the analysis for the measurement of $\Lambda(1405)$ photonproduction is described. Following reaction was focused to investigate the $\Lambda(1405)$ production,

$$\begin{aligned} \gamma p &\rightarrow K^+\Lambda(1405) \\ &\rightarrow K^+\Sigma^\pm\pi^\mp \\ &\rightarrow K^+ n\pi^+\pi^-. \end{aligned} \tag{3.8}$$

First of all, the K^+'s were identified by the LEPS spectrometer as same as the analysis of $K^+\Sigma^0(1385)$ production. Secondaly, neutrons were identified from the missing mass of the $\gamma p \rightarrow K^+\pi^+\pi^- X$ reaction ($MM(K^+\pi^+\pi^-)$) for events in which a $\pi^+\pi^-$ pair was identified by TPC. In high momentum region, a proton was misidentified as a π^+ since the energy deposition of the high momemtum proton become small, and the separation from π^+ is difficult. In order to eliminate these background events, an event selection cut was applied in the missing mass of the $\gamma p \rightarrow K^+ p\pi^- X$ reaction ($MM(K^+p\pi^-)$). Thirdly, a Σ^+ or a Σ^- was identified in the missing mass of the $\gamma p \rightarrow K^+\pi^\pm X$ reactions ($MM(K^+\pi^\pm)$). The events of $\Lambda(1405)$ production were purified using a kinematicac fit requiring $MM(K^+\pi^+\pi^-) = M_n$ and $MM(K^+\pi^\pm) = M_{\Sigma^\pm}$, where M_n and $M_{\Sigma^\pm}$ were the masses of the neutron and $\Sigma^\pm$, respectively. Then, the yield of the $\Lambda(1405)$ was extracted from a peak in the $MM(K^+)$ for the $K^+\Sigma^\pm\pi^\mp$ final state after subtracting the contamination from $\Sigma^0(1385) \rightarrow \Sigma^\pm\pi^\mp$mode which was estimated in the previous section and the contamination of $K^0(892)\Sigma^+$ production.

The procedure of the analysis is as follows,

1. selection of a K^+ by the LEPS spectrometer,
2. selection of a $\pi^+\pi^-$ pair by the TPC,
3. reduction of background events due to p/π^+ misidentification by TPC using $MM(K^+p\pi^-)$,
4. neutron selection in $MM(K^+\pi^+\pi^-)$,
5. Σ^+ or Σ^- selection by the kinematic fit.

3.5 Neutron identification

Neutrons were identified from the missing mass of the $\gamma p \rightarrow K^+\pi^+\pi^- X$ reaction ($MM(K^+\pi^+\pi^-)$), where the K^+ was detected by the LEPS spectrometer, $MM(K^+)$ was found to be in the mass region of $\Lambda(1405)/\Sigma^0(1385)(1.30 < MM(K^+) < 1.45$ GeV/c^2) and a $\pi^+\pi^-$ pair was identified by the TPC. Figure 3.16 shows the distribution of $MM(K^+\pi^+\pi^-)$. A peak corresponding to the neutron is clearly seen.

Figure 3.17 shows a correlation plot between the $MM(K^+\pi^+\pi^-)$ and the missing mass of $\gamma p \rightarrow K^+p\pi^-(MM^2(K^+p\pi^-))$, where a π^+ candidate was assumed as a proton and assined the proton mass. A locus of $MM^2(K^+p\pi^-) = (\pi^0$ mass) can be seen. This contamination was caused by protons which were mis-identified as π^+'s. These protons were produced by

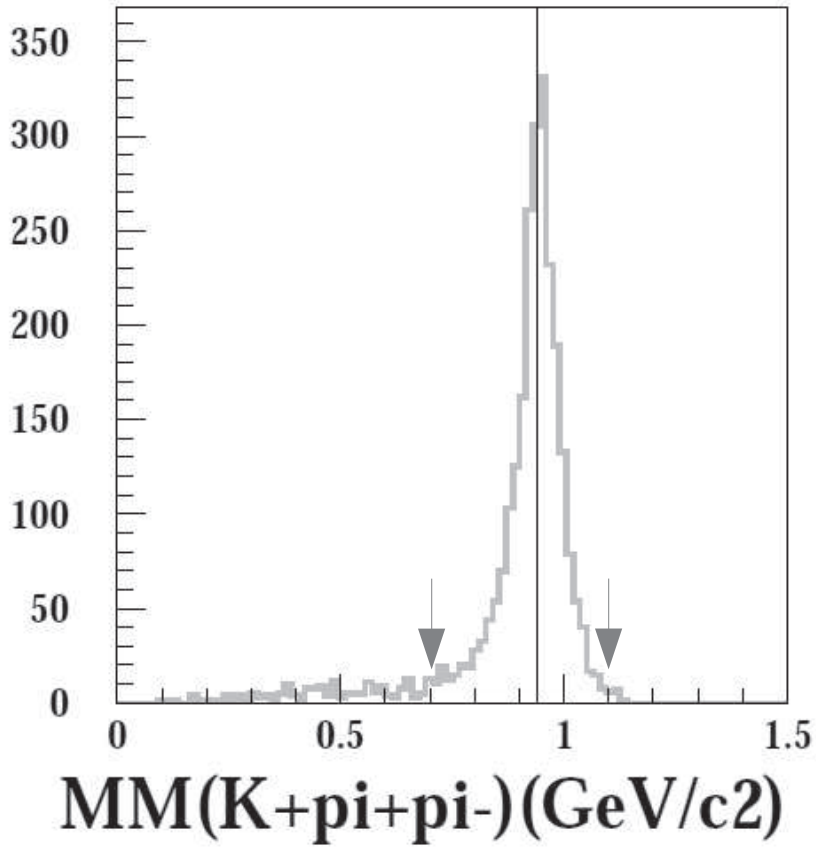

Figure 3.16: Distribution of the missing mass of the $\gamma p \rightarrow K^+\pi^+\pi^- X$ reaction, $MM(K^+\pi^+\pi^-)$.

either the $\gamma p \rightarrow K^+\Sigma^0(1385) \rightarrow K^+\Lambda\pi^0 \rightarrow K^+p\pi^-\pi^0$reaction or $\gamma p \rightarrow K^+\Lambda(1405) \rightarrow K^+\Sigma^+\pi^- \rightarrow K^+p\pi^0\pi^-$reaction. These background events can be eliminated by rejecting events for which $MM^2(K^+p\pi^-)$ corresponds to π^0 mass. The cut condition was set to be $MM^2(K^+p\pi^-) <$ -0.05 $(\mathrm{GeV/c^2})^2$.

The neutron selection boundries were set to $0.70 < MM(K^+\pi^+\pi^-) < 1.05$ GeV/c^2.

3.6 Event selection by the kinematical fit

The Σ^+ and Σ^- from the decay of the $\Lambda(1405)$ can be identified from the missing mass of the $\gamma p \rightarrow K^+\pi^- X$ reaction and $\gamma p \rightarrow K^+\pi^+ X$ reaction, respectively. Figure 3.18 shows the distributions of $MM(K^+\pi^-)$ and $MM(K^+\pi^+)$ for events which survived the neutron selection cut and the π^0 rejection cut. The peak corresponding to Σ^+ and Σ^- can be seen. Figure 3.19 shows the correlation between $MM(K^+\pi^+)$ and $MM(K^+\pi^-)$. Some of events are in the region where $MM(K^+\pi^+) \simeq MM(K^+\pi^-) \simeq 1.2$ GeV/c^2. For such events, it is impossible to separate the Σ^+ and Σ^- from the missing mass.

In order to separate Σ^+ and Σ^-, a kinematic fit was used with two constraints: $MM(K^+\pi^+\pi^-) = M_n$ and $MM(K^+\pi^\pm) = M_{\Sigma^\mp}$. The parameters for kinematic fit were, the photon energy (E_γ), the three momentum of the K^+, π^+ and π^-. The resolution of photon energy was obtained by

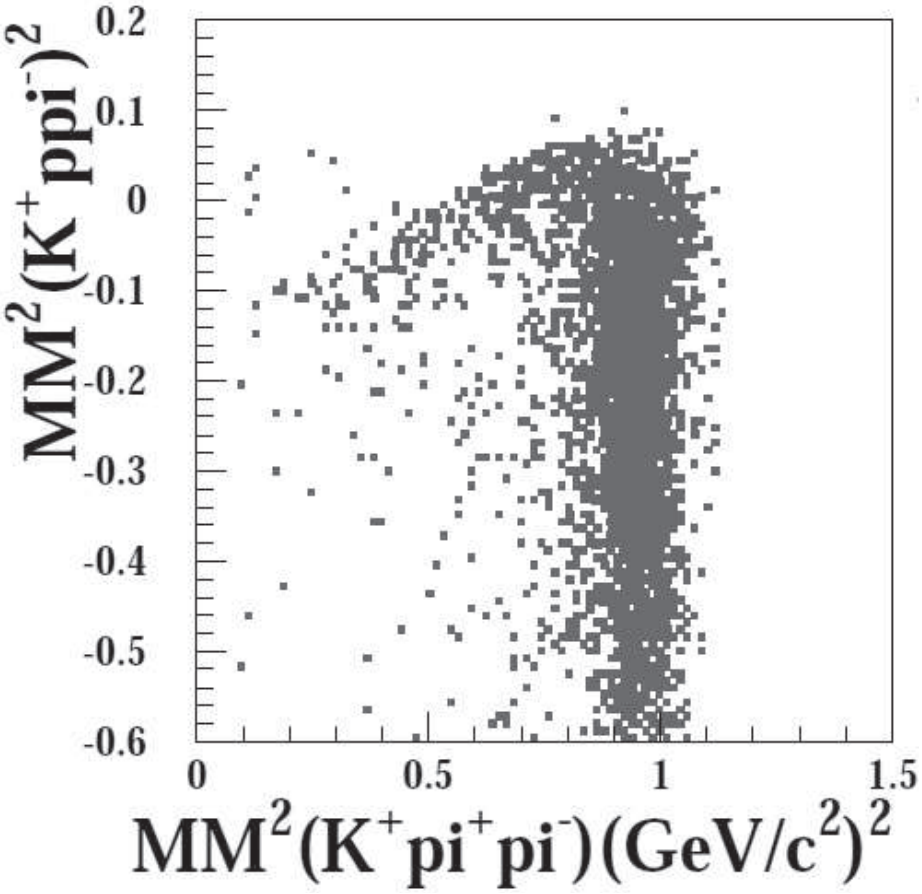

Figure 3.17: A correlation plot between the $MM(K^+\pi^+\pi^-)$ and the $MM^2(K^+p\pi^-)$.

the measurement. The momentum and angular resolution of reconstructed tracks are obtained from the MC simulation.

Since the mass difference between $\Sigma^+(1.1893\ \mathrm{GeV/c^2})$ and $\Sigma^-(1.1972\ \mathrm{GeV/c^2})$ was not negligible, the kinematic fit was applied twice for each event firstly with the $\Sigma^+\pi^-$ decay assumption and secondly with the $\Sigma^-\pi^+$ decay assumption. Figure 3.20 shows the distribution of the χ^2 probability with $\Sigma^+\pi^-$ decay assumption ($prob_{\Sigma^+\pi^-}$) and that with $\Sigma^-\pi^+$ decay assumption ($prob_{\Sigma^-\pi^+}$).

3.7 Selection of Σ^+ or Σ^-

The decay mode of $\Lambda(1405)$, $\Sigma^+\pi^-$ or $\Sigma^-\pi^+$, was identified from the χ^2 probability of the kinematic fit. Figure 3.21 shows the correlation of the χ^2 probability of the kinematic fit between the $\Sigma^-\pi^+$ assumption ($prob_{\Sigma^-\pi^+}$) and the $\Sigma^+\pi^-$ assumption ($prob_{\Sigma^+\pi^-}$) for events which survived the neutron selection cut, the π^0 rejection cut. The χ^2 probability with the $\Sigma^+\pi^-$ decay assumption, $prob_{\Sigma^-\pi^+}$, should be larger than $prob_{\Sigma^+\pi^-}$ for events with a $\Sigma^+\pi^-$ pair, and $prob_{\Sigma^-\pi^+}$ should be larger than $prob_{\Sigma^+\pi^-}$ for evnets with a $\Sigma^-\pi^+$ pair. In this way, we

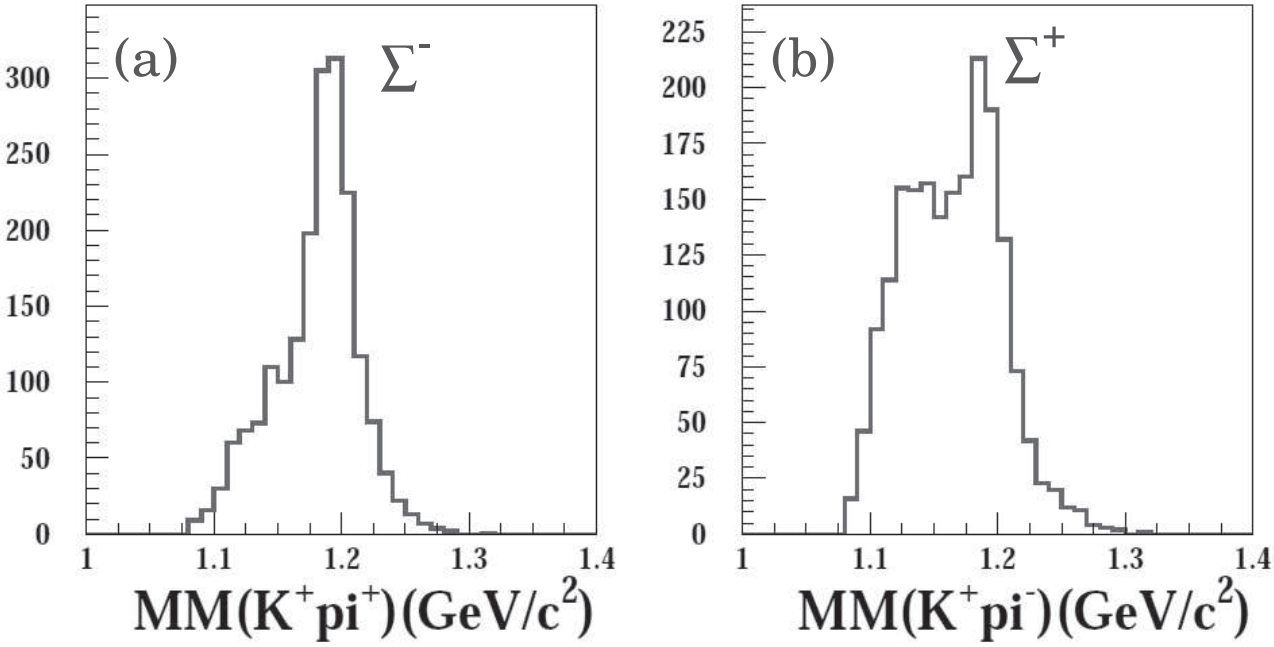

Figure 3.18: The distributions of $MM(K^+\pi)$ for events which survived the neutron selection cut and the π^0 rejection cut. (a) $MM(K^+\pi^+)$, (b) $MM(K^+\pi^-)$.

could distiguish the two decay modes using the χ^2 probability of the kinematic fit. The $\Sigma^+\pi^-$ decay events were selected by requiring $prob_{\Sigma^+\pi^-} > 0.02$ and $prob_{\Sigma^+\pi^-} > prob_{\Sigma^-\pi^+}$, whereas the $\Sigma^-\pi^+$ decay events were selected by requiring $prob_{\Sigma^+\pi^-} > 0.02$ and $prob_{\Sigma^-\pi^+} > prob_{\Sigma^+\pi^-}$.

3.8 $MM(K^+)$ spectra for charged decay modes

Figure 3.22 shows missing mass distribution for the $\gamma p \rightarrow K^+X$ reaction for the $K^+\Sigma^+\pi^-$ final state and $K^+\Sigma^-\pi^+$ final state for evnets selected by all the cuts described above. The decay mode dependence of the lineshapes of $\Lambda(1405)$ is likely due to strong interference between isospin 0 and 1 amplitudes of the $\Sigma\pi$ interaction. The cross sections of the $\Sigma^+\pi^-$ interaction ($\sigma_{\Sigma^+\pi^-}$) and $\Sigma^-\pi^+$ interaction ($\sigma_{\Sigma^-\pi^+}$) can be written using isospin 0 ($T^{(0)}$) and 1 ($T^{(1)}$) component of scattering matrices as,

$$\sigma_{\Sigma^+\pi^-} = \frac{1}{2}|T^{(1)}|^2 + \frac{1}{3}|T^{(0)}|^2 + \frac{2}{\sqrt{6}}Re(T^{(0)}T^{(1)}) \tag{3.9}$$

$$\sigma_{\Sigma^-\pi^+} = \frac{1}{2}|T^{(1)}|^2 + \frac{1}{3}|T^{(0)}|^2 - \frac{2}{\sqrt{6}}Re(T^{(0)}T^{(1)}). \tag{3.10}$$

The coefficients are deduced from the Clebsch-Gordan coefficients. The third term, the interference term of isospin 0 and 1 amplitudes, has different sign in two decay modes, and thus, this term causes the change of the lineshape depending on the decay mode.

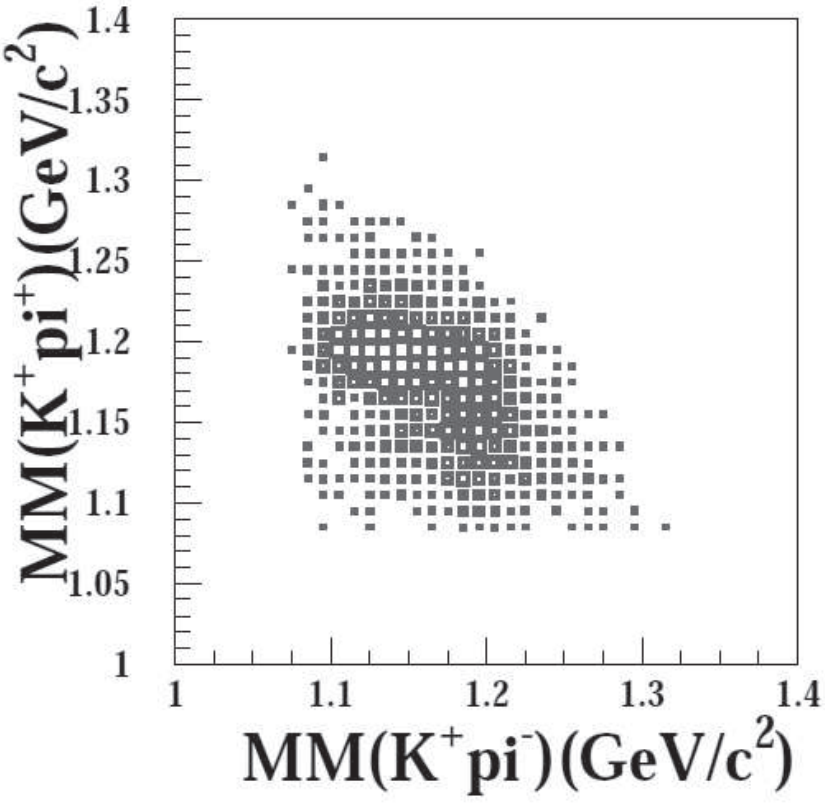

Figure 3.19: The correlation between $MM(K^+\pi^+)$ and $MM(K^+\pi^-)$.

The isospin interference term is cancelled by summing the spectra of the $\Sigma^+\pi^-$ and $\Sigma^-\pi^+$ modes. The summed spectrum was obtained after correcting for the decay branch of $\Sigma^+ \to p\pi^0$ (52%), and the result is shown in Figure 3.23.

3.9 Yield of $\Lambda(1405)$

The yield of $\Lambda(1405)$ production was extracted from a peak in the combined spectrum of the $\Sigma^+\pi^-$ decay mode and $\Sigma^-\pi^+$ decay mode in which the isospin interference term is canceled. The yields were obtained in three photon energy regions: $1.5 < E_\gamma < 2.0$ GeV, $2.0 < E_\gamma < 2.4$ GeV and $2.4 < E_\gamma < 3.0$ GeV. Figure 3.23 shows distributions of $MM(K^+)$ in three photon energy regions. The contribution from $\Sigma^0(1385)$ production estimated from $\Lambda\pi^0$ decay mode is shown as yellow circles. The background of $K^0(892)\Sigma^+$ production is measured from a invariant mass spectrum of $K^+\pi^-$ pairs. The spectra were fitted with the distribution for $K^+\Lambda(1405)$, $K^+\Lambda(1520)$ and nonresonant $K^+\Sigma\pi$ production as determined by the MC simulations, where the spectrum shape of $\Lambda(1405)$ calculated by Nacher *et al.* was used. The strength of each reaction was obtained by the fitting, with the assumption that the ratio of the yields of nonresonant $K^+\Sigma\pi$ production in the three photon energy regions is propotinal to the phase volume. The yield of $\Lambda(1405)$ production was estimated by this fitting.

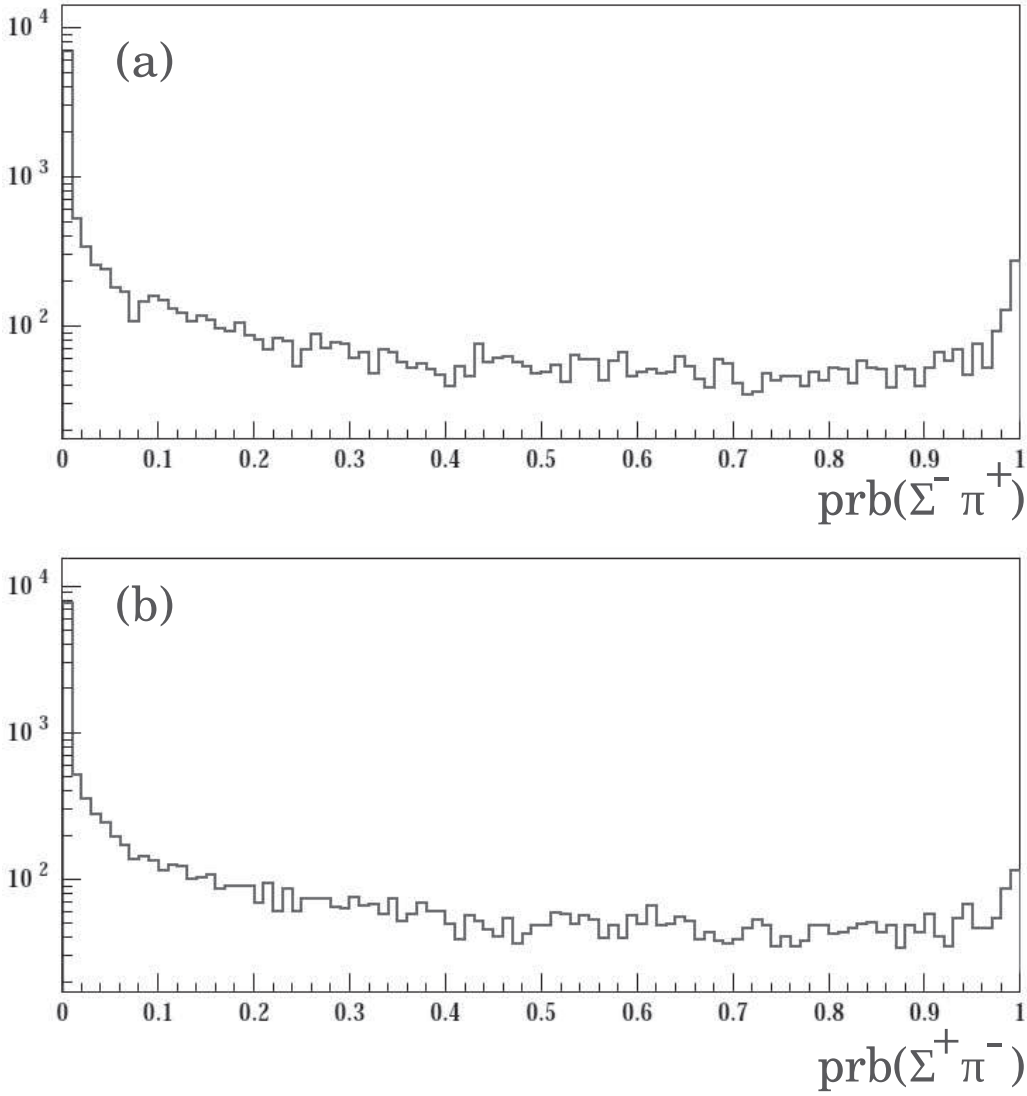

Figure 3.20: The distribution of the χ^2 probability, (a) with $\Sigma^+\pi^-$ decay assumption ($prob_{\Sigma^+\pi^-}$) and (b) with $\Sigma^-\pi^+$ decay assumption ($prob_{\Sigma^-\pi^+}$).

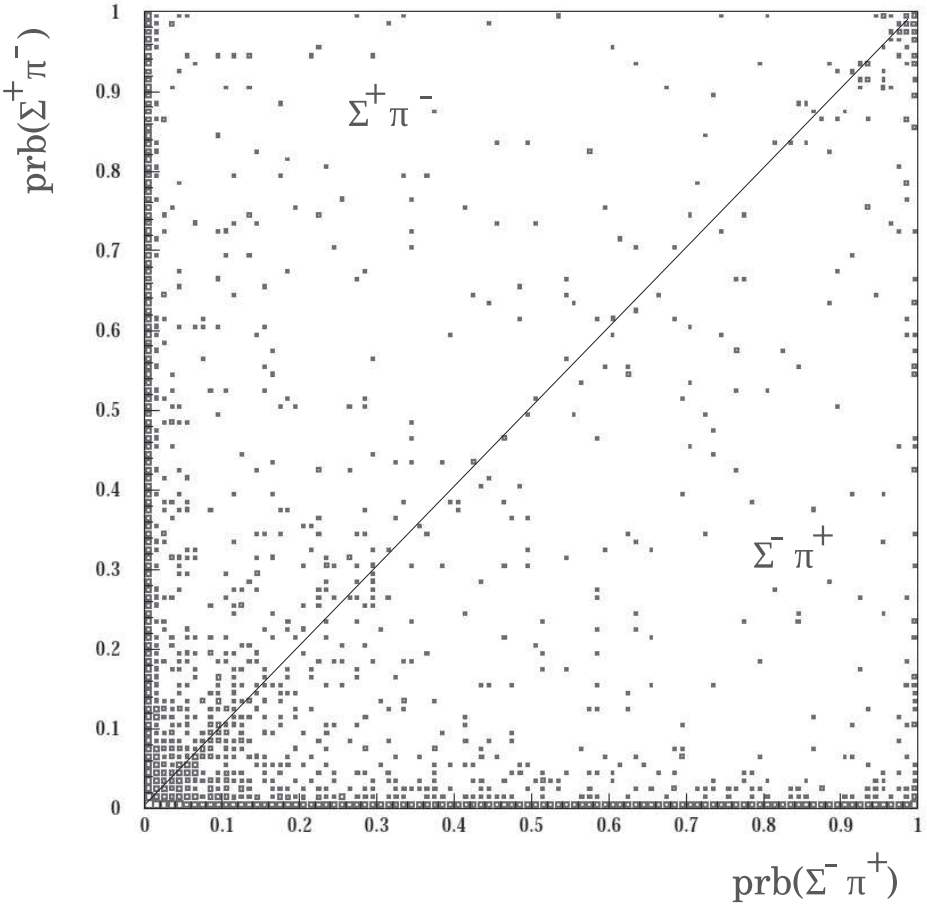

Figure 3.21: The correlation of the χ^2 probability of the kinematic fit between the $\Sigma^-\pi^+$ assumption ($prob_{\Sigma^-\pi^+}$) and the $\Sigma^+\pi^-$ assumption ($prob_{\Sigma^+\pi^-}$).

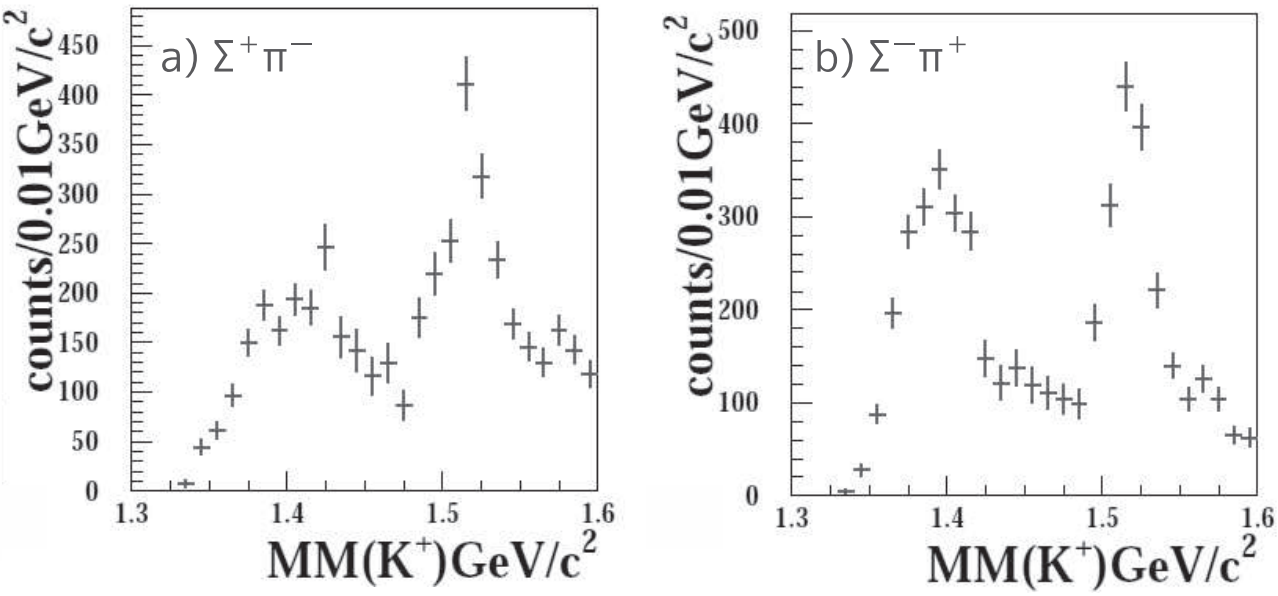

Figure 3.22: The missing mass distribution for the $\gamma p \rightarrow K^+ X$ reaction for (a) the $K^+\Sigma^+\pi^-$ final state and (b) $K^+\Sigma^-\pi^+$ final state.

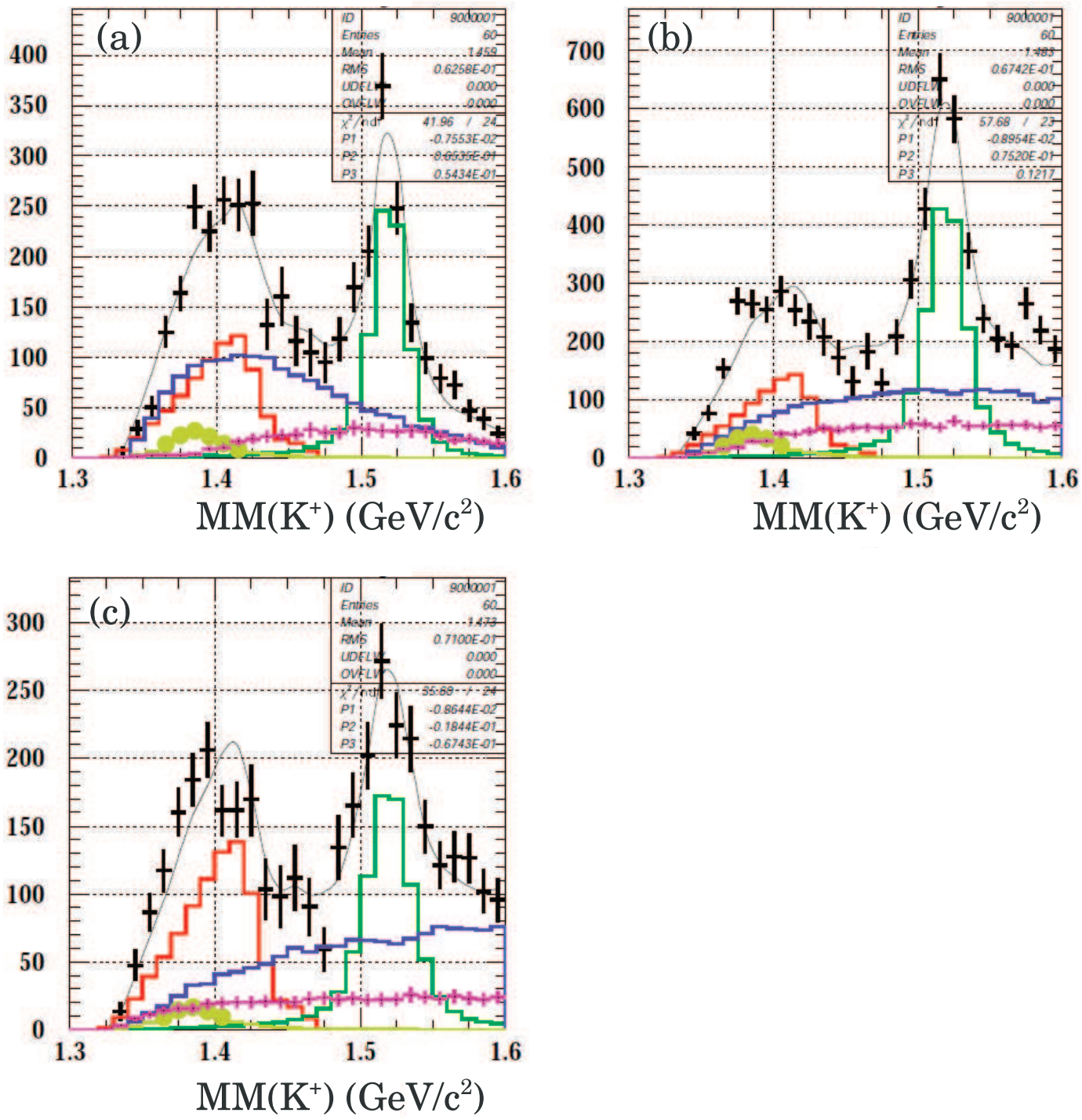

Figure 3.23: The combined $MM(K^+)$ spectrum. The solid line, black, red, yiellow, blue, green, magenta plot show the fitted result, data, the mass spectra of $\Lambda(1405)$calculated by Nacher *et al.*, $\Sigma^0(1385)$, nonresonant $K^+\Sigma\pi$, $\Lambda(1520)$ and $K^0(892)\Sigma^+$, respectively.

Chapter 4

Results

4.1 Differential cross section

The differential cross section of a hyperon is expressed as follows,

$$\frac{d\sigma}{dcos\Theta_{K^+CM}} = \frac{Y}{A \cdot N_T \cdot N_{eff\gamma} \cdot dcos\Theta_{K^+CM}}, \tag{4.1}$$

where denotes

Y : yield of a hyperon

A : acceptance in the detector system

N_T : the number of protons inside the liquid hydrogen target

$N_{eff\gamma}$: the total number of photons at the target

$d\cos\Theta_{K^+CM}$: width of $\cos\Theta_{K^+CM}$

The differential cross sections of $\gamma p \rightarrow K^+\Lambda(1405)$ reaction and those of $\gamma p \rightarrow K^+\Sigma^0(1385)$ reaction were obtained at three E_γ regions, $1.5 < E_\gamma < 2.0$ GeV, $2.0 < E_\gamma < 2.4$ GeV, $2.4 < E_\gamma < 3.0$ GeV, at $0.8 < \cos\Theta_{K^+CM} < 1.0$, where Θ_{K^+CM} is the angle of K^+momentum with respect to the beam axis in the center of mass system. The values of these cross sections are summarized in Table 4.1.

The differential cross sections of $\Sigma^0(1385)$ photoproduction were obtained using the yield of the reaction $\gamma p \rightarrow K^+\Sigma^0(1385) \rightarrow K^+\Lambda\pi^0$ and the systematic errors were estimated from the uncertainties of the background of the reaction $\gamma p \rightarrow K^+\Lambda(1405)/\Sigma^0(1385) \rightarrow K^+\Sigma^+\pi^-$ in the reaction $\gamma p \rightarrow K^+\Sigma^0(1385) \rightarrow K^+\Lambda\pi^0$.

	$\Lambda(1405)$ (μb)	$\Sigma^0(1385)$ (μb)
$1.5 < E_\gamma < 2.0$ GeV	$0.236 \pm 0.017(stat.) \pm 0.011(syst.)$	$0.356 \pm 0.036(stat.) \pm 0.074(syst.)$
$2.0 < E_\gamma < 2.4$ GeV	$0.153 \pm 0.015(stat.) \pm 0.016(syst.)$	$0.467 \pm 0.027(stat.) \pm 0.104(syst.)$
$2.4 < E_\gamma < 3.0$ GeV	$0.642 \pm 0.035(stat.) \pm 0.017(syst.)$	$0.612 \pm 0.049(stat.) \pm 0.114(syst.)$

Table 4.1: The differential cross section of $\gamma p \rightarrow K^+\Lambda(1405)$ reaction and those of $\gamma p \rightarrow K^+\Sigma^0(1385)$ reaction at each E_γ region.

4.2 Photon energy dependence of the differential cross section

The photon energy dependence of the differential cross section of $\gamma p \rightarrow K^+\Sigma^0(1385)$ reaction and $\gamma p \rightarrow K^+\Lambda(1405)$ reaction are shown in Figure 4.1 and Figure 4.2, respectively. Figure 4.3 shows the photon energy dependence of the sum of the differential cross section of $\gamma p \rightarrow K^+\Lambda(1405)$ reaction and $\gamma p \rightarrow K^+\Sigma^0(1385)$ reaction.

In Figure 4.1, the differential cross section for $\Sigma^0(1385)$ production increase with the increasing photon energy.

On the other hand, Figure 4.2 shows that the differential cross section for $\Lambda(1405)$ production at the photon energy region of $2.0 < E_\gamma < 2.4$ GeV is smaller than that of $1.5 < E_\gamma < 2.0$ GeV region. This dependence is simillar to the result of the previous LEPS TPC experiment [24]. However, the differential cross section for$\Lambda(1405)$ production increase at the photon energy region of $2.4 < E_\gamma < 3.0$ GeV.

4.3 Comparison with two experiments at LEPS

In the LEPS beam line, M.Niiyama *et al.*[24] measured the differential cross sections for $\Lambda(1405)$ and $\Sigma^0(1385)$, as already referred to (the previous LEPS TPC experiment, LEPS TPC1). Recently, D.S.Ahn [22] finished the analysis of $\Sigma^0(1385)/\Lambda(1405)$ photoproduction (LEPS K^+). D.S.Ahn measured the sum of the differential cross sections for photoproduction $\Sigma^0(1385)$ and $\Lambda(1405)$.

Figure 4.4 shows the comparison of the sum of $\Lambda(1405)$ and $\Sigma^0(1385)$ photoproduction cross sections.

After normalizing the results of this analysis and those of LEPS TPC1 to those of LEPS K^+, the cross sections for $\Lambda(1405)$ and $\Sigma^0(1385)$ of this analysis and LEPS TPC1 were scaled. The scaled cross sections are consistent within errors (Figure 4.5 and 4.6).

4.4 Comparison with CLAS

The differential cross sections of $\Lambda(1405)$ obtained by this analysis were compared with those of CLAS at overlap region of $\cos\Theta_{K^+CM}$ and E_γ. Figure 4.7 shows the result of CLAS and this analysis.

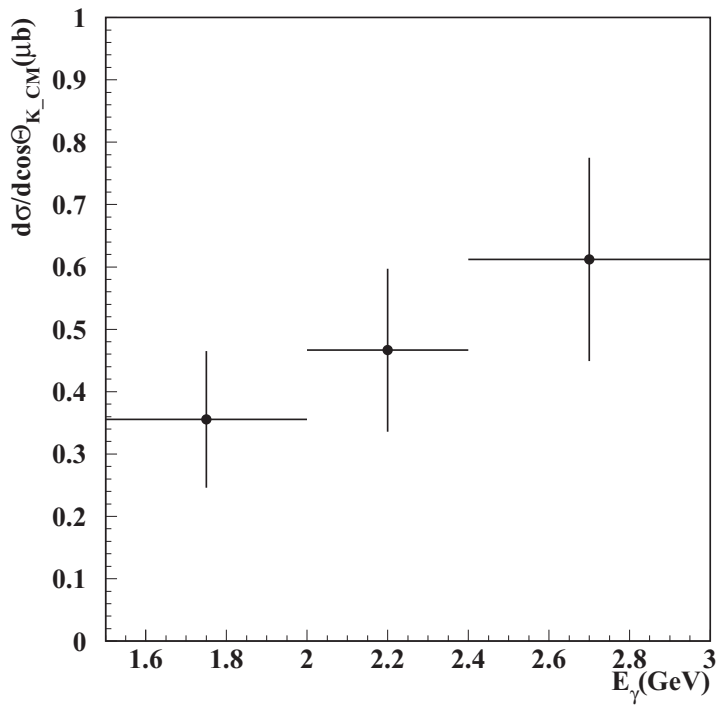

Figure 4.1: The photon energy dependence of the differential cross section of $\gamma p \rightarrow K^{+}\Sigma^{0}(1385)$ reaction.

They are consistent at the E_γ region of $1.5 < E_\gamma < 2.0$ GeV, $2.4 < E_\gamma < 3.0$ GeV. However, at the E_γ region of $2.0 < E_\gamma < 2.4$ GeV, they are inconsistent.

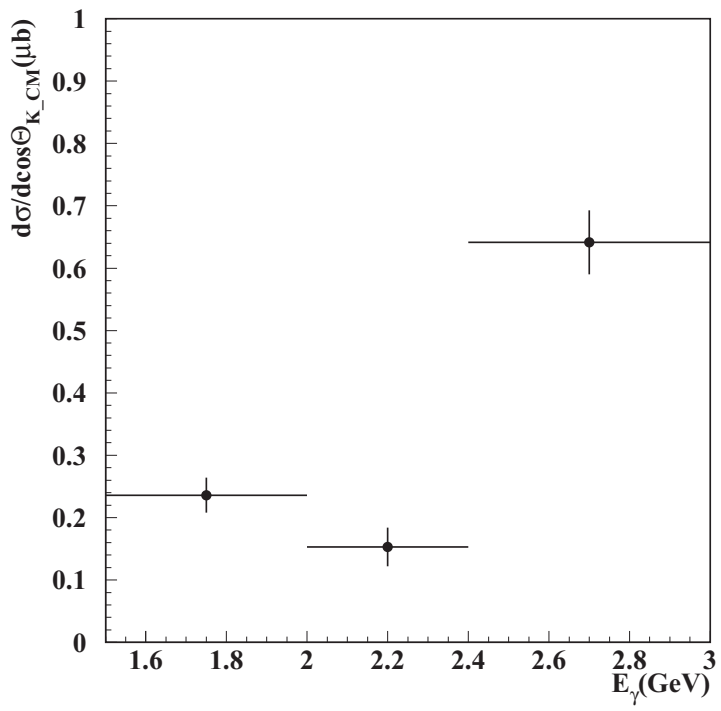

Figure 4.2: The photon energy dependence of the differential cross section of $\gamma p \rightarrow K^{+}\Lambda(1405)$ reaction.

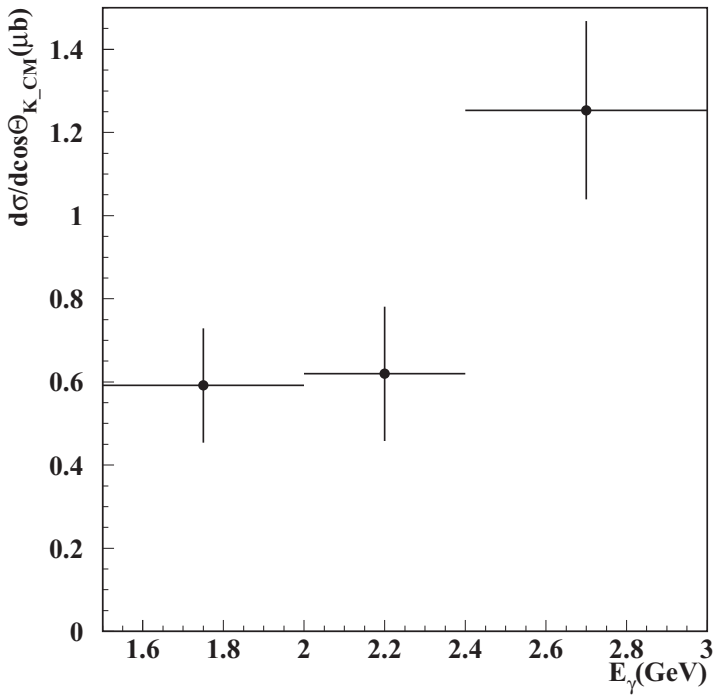

Figure 4.3: The photon energy dependence of the sum of the differential cross section of $\gamma p \rightarrow K^+\Lambda(1405)$ reaction and $\gamma p \rightarrow K^+\Sigma^0(1385)$reaction.

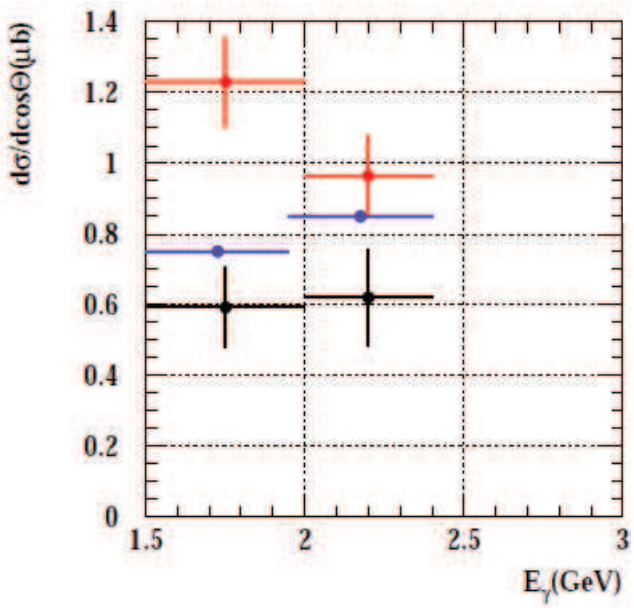

Figure 4.4: Comparison of the sum of the differential cross section for $\Lambda(1405)$and $\Sigma^0(1385)$between D.S.Ahn , Niiyama *et al.* and this analysis. Blue, red and black points correspond to the data of D.S.Ahn, Niiyama and this analysis, respectively.

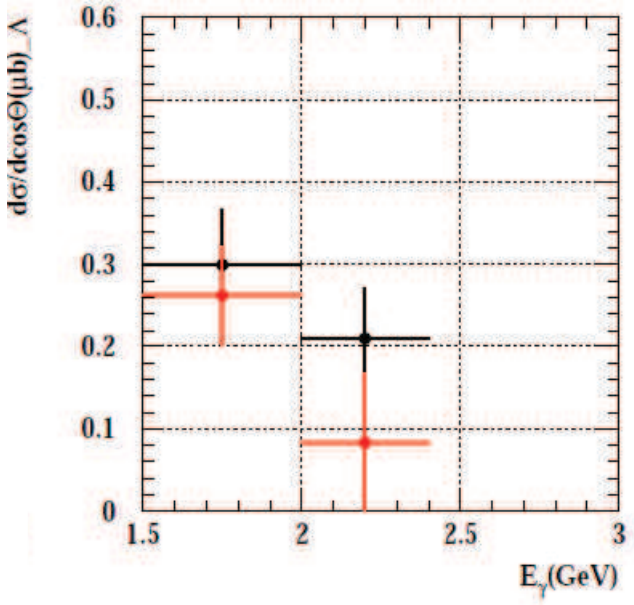

Figure 4.5: Comparison of the differential cross section for $\Lambda(1405)$ between Niiyama *et al.* and this analysis, after nomrmalized to D.S.Ahn. Red and black points correspond to the data of Niiyama and this analysis, respectively.

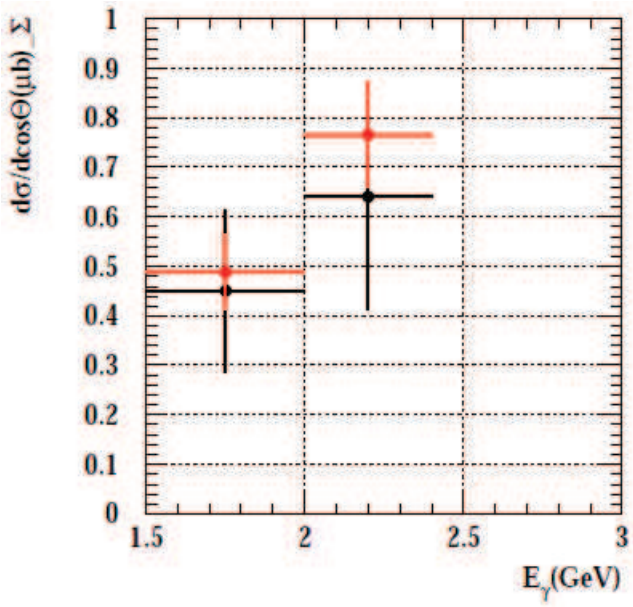

Figure 4.6: Comparison of the differential cross section for $\Sigma^0(1385)$ between Niiyama *et al.* and this analysis, after nomrmalized to D.S.Ahn. Red and black points correspond to the data of Niiyama and this analysis, respectively.

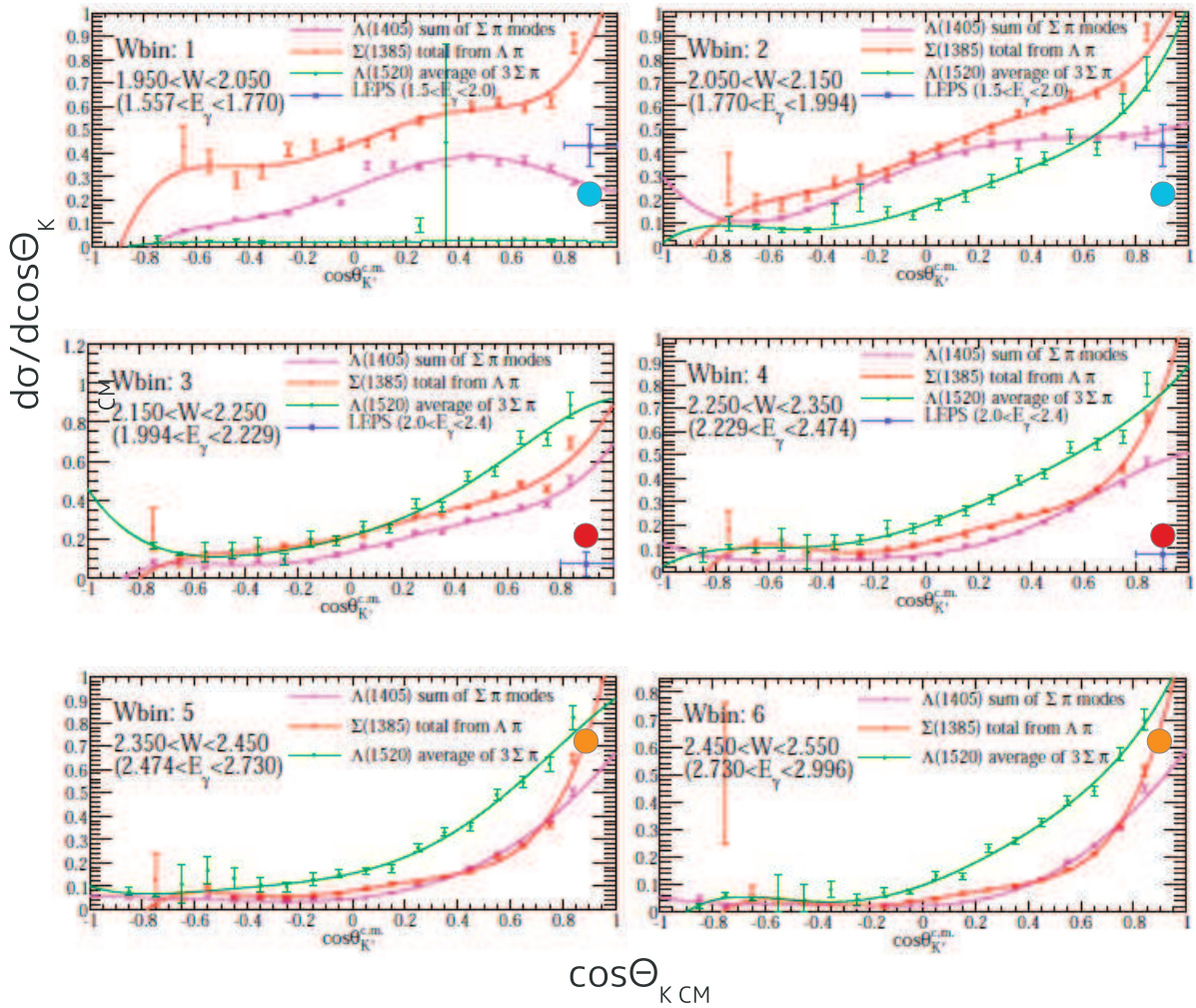

Figure 4.7: Comparison of the differential cross section for $\Lambda(1405)$ between CLAS and this analysis. Magenta line shows the $\Lambda(1405)$ result of CLAS. Blue, red and yellow points correspond to this analysis in the E_γ region of $1.5 < E_\gamma < 2.0$ GeV, $2.0 < E_\gamma < 2.4$ GeV and $2.4 < E_\gamma < 3.0$ GeV, respectively.

Chapter 5

Discussion

The differential cross sections of $\Lambda(1405)$ photoproduction were obtained using the yield of the reaction $\gamma p \rightarrow K^+\Lambda(1405) \rightarrow K^+ \Sigma^{\pm} \pi^{\mp} \rightarrow K^+ n \pi^+ \pi^-$. The $\Sigma^0(1385)$ photoproduction reaction has the same final state and contamitates the estimation of the yield of $\Lambda(1405)$ photoproduction. The amount of the contamination was estimated using the yield of the reaction $\gamma p \rightarrow K^+\Sigma^0(1385) \rightarrow K^+\Lambda\pi^0$. Therefore, the differential cross sections of $\Lambda(1405)$ photoproduction have the systematic errors corresponding to those of $\Sigma^0(1385)$ photoproduction. However, the branching ratio of the decay mode of $\Sigma^0(1385)\rightarrow\Sigma\pi$ (11.7%) is much smaller than that of the decay mode of $\Sigma^0(1385)\rightarrow\Lambda\pi^0$ (87.0%) and that is the reason why the systematic errors of $\Lambda(1405)$ photoproduction are smaller than those of $\Sigma^0(1385)$ photoproduction.

The cross section for $\Lambda(1405)$ photoproduction decrease once in the photon energy range of $2.0 < E_\gamma < 2.4$ GeV and then increase rapidly again as the photon energy increase.

Nam *et al.*[27] suggested *s*-channel dominance to explain the decrease of the $\Lambda(1405)$ differential cross section in the photon energy range of $2.0 < E_\gamma < 2.4$ GeV obtained by the previous LEPS TPC experiment. In the photon enregy region of $E_\gamma < 2.4$ GeV, the E_γ dependence of the differential cross section of $\Lambda(1405)$ photoproduction obtained by this analysis is similar to that obtained by the previous LEPS TPC experiment. On the other hand, in the photon enregy region of $2.4 < E_\gamma < 3.0$ GeV, the differential cross section of $\Lambda(1405)$ photoproduction measured by this analysis increases. It is clear that $\Lambda(1405)$ has different production mechanisms. The suggention by Nam *et al.* should be modified or is correct for the lower photon energy region.

In the photon energy region of $2.4 < E_\gamma < 3.0$ GeV, the differential cross section obtained from this analysis is consistent with that measured by CLAS and the results of CLAS have a forward peak. Therefore, the increase of the differential cross section of $\Lambda(1405)$ photoproduction is caused by *t*-channel contribution in the $\Lambda(1405)$ production process.

Because this analysis covers the very forward angle region of K^+, the increase of the differential cross secion for $\Lambda(1405)$ photoproduction at the higher E_γ corresponds to the rapid increase of the differential cross section for $\Lambda(1405)$ at the small momentum transfer region. This means that $\Lambda(1405)$ has a large form factor, and if we assume $\Lambda(1405)$ is a resonance of $\overline{K}N$, an exchanged particle in *t*-channel should be $\overline{K}$, and the increase of the differential cross section for $\Lambda(1405)$ photoproduction can not be explained by K^- exchange in a tree level *t*-channel diagram because the vertex of $\gamma\ K\overline{K}$ is propotional to the momentum transfer.

Therefore, different K^- exchange process should be considered, such as a rotational band of K^- (Regge trajectory), or vector meson dominance intermediated by virtual ϕ, ρ, ω mesons. In order to investigate exchanged particles in t-channel, we need to measure the photon beam asymmetry of $\Lambda(1405)$ photoproduction at forward angle of K^+. For example, if Regge trajectory contributes to $\Lambda(1405)$ photoproduction, the sign of the photon beam asymmetry become negative. If vertex of $\gamma K\overline{K}$ need to be modified, it affects not only $\Lambda(1405)$, but also other Hyperons and the cross section for them is expected to increase at forward angle.

Chapter 6

Summary

The differential cross sections of $\gamma p \rightarrow K^+\Lambda(1405)$ and $\gamma p \rightarrow K^+\Sigma^0(1385)$ reaction were measured by data analysis of a hyperon photoproduction experiment carried out at SPring-8/LEPS. In this experiment, a backward-Compton-scattered photon beam and a liquid hydrogen target were used. The photon energy ranged from 1.5 GeV to 3.0 GeV. The charged particles produced by a reaction were detected by the LEPS spectrometer and a time projection chamber. The differential cross sections were obtained at three photon energy ranges: 1.5 $< E_\gamma <$ 2.0 GeV, 2.0 $< E_\gamma <$ 2.4 GeV and 2.4 $< E_\gamma <$ 3.0 GeV. The spectra of hyperons were obtained from the missing mass distribution of the $\gamma p \rightarrow K^+X$, $MM(K^+)$, requiring the cut condition of $0.8 < \cos\Theta_{K^+CM} < 1.0$, where Θ_{K^+CM} is the angle of K^+ momentum with respect to the beam axis in the center of mass system.

The yield of $\Sigma^0(1385)$was obtained by analysing following reaction:

$$\begin{aligned} \gamma p &\rightarrow K^+\Sigma^0(1385) \\ &\rightarrow K^+\Lambda\pi^0 \\ &\rightarrow K^+p\pi^-\pi^0. \end{aligned} \tag{6.1}$$

The procedure of analysis of $\Sigma^0(1385)$ was as follows:

1. The missing mass distribution $MM(K^+)$ was obtained, requiring that a $\Lambda(1116)$ was identified in the invariant mass distribution of $p\pi^-$pair detected by TPC ($M(p\ \pi^-)$).

2. The amount of the contamination from $\gamma p \rightarrow K^+\Lambda(1405) \rightarrow K^+\Sigma^0\pi^0 \rightarrow K^+\Lambda\gamma\ \pi^0$ reaction was extracted from the missing mass distribution of $\gamma p \rightarrow K^+p\pi^-X$, $MM^2(K^+p\pi^-)$.

3. The amount of the contamination from $\gamma p \rightarrow K^+\Lambda(1405)/\Sigma^0(1385) \rightarrow K^+\Sigma^+\pi^- \rightarrow K^+p\pi^0\pi^-$ reaction was extracted by estimating the yield of the peak corresponding to Σ^+ in the missing mass distribution of $\gamma p \rightarrow K^+\pi^-X$, $MM(K^+\pi^-)$.

4. The yield of the reaction 6.1 was determined by subtracting the contamination of 2 and 3 from the yield of 1.

In the process of 3, the width of the peak corresponding to the $\Sigma^+$was much wider in the real data than in the Monte Carlo simulation, and the reason of the larger width could not

be specified in this analysis. Then, the systematic error of the yield of the reaction (6.1) was determined by estimating the yield of the reaction (6.1) twice, firstly assuming that there were no contribution to the peak from $\Sigma^+$and secondly assuming that all contribution of the peak came from Σ^+. The diffential cross sections of $\Sigma^0(1385)$photoproduction were obtained to be $0.356 \pm 0.036(stat.) \pm 0.074(syst.)$ μb for $1.5 < E_\gamma < 2.0$ GeV, $0.467 \pm 0.027(stat.) \pm 0.104(syst.)$ μb for $2.0 < E_\gamma < 2.4$ GeV and $0.612 \pm 0.049(stat.) \pm 0.114(syst.)$ μb for $2.4 < E_\gamma < 3.0$ GeV.

The yield of $\Lambda(1405)$was obtained by analysing following reaction:

$$\begin{aligned} \gamma p &\rightarrow K^+\Lambda(1405) \\ &\rightarrow K^+\Sigma^\pm\pi^\mp \\ &\rightarrow K^+ n\pi^+\pi^-. \end{aligned} \tag{6.2}$$

The procedure of analysis of $\Lambda(1405)$was as follows:

1. The missing mass distribution $MM(K^+)$ was obtained, requiring that a $\pi^+$and a π^-were detected by TPC and a neutron was identified in the missing mass distribution of $\gamma p \rightarrow K^+\pi^+\pi^- X$, $MM(K^+\pi^+\pi^-)$.

2. The charged decay modes of $\Lambda(1405)$, $\Lambda(1405)\rightarrow \Sigma^+\pi^-$and $\Lambda(1405)\rightarrow \Sigma^-\pi^+$, were identified separately by kinematical fit. The distribution of $MM(K^+)$ for each decay mode was obtained.

3. In order to cancel the effect of the interference between isospin 1 and 0, $MM(K^+)$ spectra for $\Sigma^+\pi^-$and $\Sigma^-\pi^+$decay mode were combined. The yield of the reaction (6.2) was estimated by fitting the combined spectrum with line shape of $\Lambda(1405)$calculated by Nacher *et al.* and background shape.

Because the amount of the contamination from $\gamma p \rightarrow K^+\Sigma^0(1385)\rightarrow K^+\Sigma^\pm\pi^\mp$reaction was estimated using the yield of the reaction (6.1) in the process 3, the yield of the reaction (6.2) has a corresponding systematic error. The diffential cross sections of $\Lambda(1405)$ photoproduction were obtained to be $0.236 \pm 0.017(stat.) \pm 0.011(syst.)$ μb for $1.5 < E_\gamma < 2.0$ GeV, $0.153 \pm 0.015(stat.) \pm 0.016(syst.)$ μb for $2.0 < E_\gamma < 2.4$ GeV and $0.642 \pm 0.035(stat.) \pm 0.017(syst.)$ μb for $2.4 < E_\gamma < 3.0$ GeV.

The photon energy dependence of $\Lambda(1405)$ production obtained from this analysis is similar to previous LEPS TPC experiment at $E_\gamma < 2.4$ GeV and decrease with the increasing photon energy. On the other hand, the differential cross section of $\Lambda(1405)$ at $2.4 < E_\gamma < 3.0$ GeV, which is a new result from this analysis, shows the increase. This implies that $\Lambda(1405)$ is produced through the different process at the different energy region and t-channel contribution for $\Lambda(1405)$ photoproduction at higher E_γ region. In order to measure the exchanged particle in t-channel, the photon beam asymmetry of $\Lambda(1405)$ photoproduction should be measured precisely at forward angle of K^+. A new beam line LEPS2 has just started and the study of $\gamma p \rightarrow K^+\Lambda(1405)$ reaction will be able to perform with high statistics in the future.

Acknowledge

I am sincerely grateful to Prof. Takashi Nakano. He has supported and encouraged me with enthusiasm all during my Ph.D study. His advice is always excellent and helpful for me. I have learned many things about physics and analysis from him, and I have been impressed with his professionalism as a physicist. I could not complete this Ph.D thesis without his support.

I would like to thank Prof. Masaru Yosoi for supporting me for a long, long time. He is a great, dedicated and gracious mentor for my research and life. I have learned a lot of things about experiments and detectors from him since I was a master student in Kyoto University. He has given me essential comments and helped me to proceed with the analysis. I will never forget his thoughtful guidance.

I would like to thank all the committee members, Prof. Atsushi Hosaka, Prof. Masaharu Aoki, , Prof. Tadafumi Kishimoto.

I would like to really appreciate LEPS Collaborators Prof. M. Sumihama, Prof. M. Niiyama, Prof. T. Hotta, Prof. W.C. Chang, Prof. J.Y. Chen, Prof. M. Miyabe, Dr. Y. Morino, Dr. Y. Kato, Dr. T. Sawada, Mr. Y. Kon, Prof. J.K. Ahn, Dr. D.S. Ahn, Dr. S.H.Hwang, Prof. H. Noumi, Prof. Y. Sugaya, Prof. T. Mibe, Prof. T. Yorita, Prof. H. Kohri, Prof. S. Ajimura, Prof. N. Muramatsu, Prof. T. Ishikawa,, Prof. M. Uchida, Prof. K. Imai, Prof. K. Hicks, Prof. C. Rangacharyulu, Prof. H. Fujimura, Dr. Y. Ohashi and Dr. S. Date.

Bibliography

[1] J. Beringer *et al.* Phys. Rev. D **86**, 010001 (2012) (PDG).

[2] N. Isgur and G. Karl, Phys. Rev. D18, 4187 (1978).

[3] R.H. Dalitz, Rev. Mod. Phys. 33, 471 (1961).

[4] R.H. Dalitz, T.C. Wong and G. Rajasekaran, Phys. Rev. 153, 1617 (1967).

[5] R.H. Dalitz, Euro. Phys. J C15, 748 (2000) (PDG).

[6] W. Melnitchouk et al., Phys. Rev. D67, 114506 (2003).

[7] Y. Nemoto, N.Nakajima, H. Matsufuru and H. Suganuma, Phys. Rev. D68,094505 (2003).

[8] N. Ishii, T. Doi, M. Oka and H. Suganuma, Prog. Theor. Phys. Suppl. 168, 598 (2007).

[9] J.C. Nacher, E. Oset, H. Toki and A. Ramos, Phys. Lett. B455, 55 (1999).

[10] D. Jido, J.A. Oller, E. Oset, A. Ramos and U.-G, Meissner, Nuc. Phys. A755, 669 (2005).

[11] D.W. Thomas, A. Engler, H.E. Fisk and R.W. Kraemer Nucl. Phys. B56, 15 (1973).

[12] R.J. Hemingway, Nucl. Phys. B253, 742 (1985).

[13] S. Prakhov et al., Phys. Rev. C70, 034605 (2004).

[14] V.K. Magas, E. Oset and A. Ramos, Phys. Rev. Lett. 95, 052301 (2005).

[15] I. Zychor et al., Phys. Lett. B 660, 167 (2008).

[16] M.Q. Tran et al., Phys. Lett. B445, 20 (1998).

[17] J.W.C. McNabb et al., Phys. Rev. C69, 042201 (2004).

[18] K.-H. Glander et al., Eur. Phys. J. A19, 251 (2004).

[19] M. Sumihama et al., Phys. Rev. C73, 035214 (2006).

[20] S. Capstick and W.Roberts, Phys. Rev. D58, 074011 (1998).

[21] J.K. Ahn et al., Nucl. Phys. A721, 715c (2003).

[22] D.S. Ahn, Doctor Thesis of Osaka University, (2012).

[23] K. Moriya, Doctor Thesis of Carnegie Mellon University, (2010).

[24] M. Niiyama *et al.* (LEPS Collaboration), Phys. Rev. **C78**, 035202 (2008).

[25] Y. Oh, C.M. Ko and K. Nakayama, Phys. Rev. C 77, 045204 (2008).

[26] M.F.M. Lutz and M. Soyeur, Nucl. Phys. A748, 499 (2005).

[27] S.I. Nam, J.H. Park, A. Hosaka, H.C. Kim, hep-ph/arXiv:0806.4029 .

[28] T. Nakano et al., Nucl. Phys. A684, 71c (2001).

[29] `http://garfield.web.cern.ch/garfield`

[30] A, D'Angelo, O. Bartalini, V. Bellini, P. Levi Sandri, D. Moricciani, L. Nicoletti and A. Zucchiatti, Nucl, Instr. Meth. **A455** (2000) 1.

[31] SPring-8 annual report (1998) 132